Experimental and numerical investigations of wind-induced effects on ground-mounted solar panels at the WDS facility

by

Charly Massaad

A thesis submitted to the Faculty of Graduate and Postdoctoral studies in partial fulfillment of the requirements for the degree of

Master of Applied Science

In

Civil Engineering

Department of Civil Engineering

University of Ottawa

Ottawa, Canada

June 2019

Abstract

The usage of ground-mounted photovoltaic solar panels is increasing, and it is essential to fully understand the wind behavior and loading on the panels, since there is no specific code or guideline for their design in the present. In addition, the University of Ottawa and Carleton University recently developed a new facility, called the Wind Damage Simulator (WDS). This study will allow to understand the flow behavior in the facility, along with the effects of different blower rpm settings on the flow. A CFD study was also conducted, in order to examine the methodology and turbulence models suitable for the flow replicated in this facility, for future research.

The newly developed Wind Damage Simulator (WDS) facility was used to examine wind-induced effects on two solar panels attached to a frame. The mean pressure coefficient distribution on the photovoltaic panels was examined for several wind angles of incidence (AOI) and wind speeds. The wind AOI considered were the 0°, 30°, 45°, 180°, 210° and 225°, along with wind speeds ranging from 14 m/s to 42 m/s, with increments of around 2 m/s. The experimental results showed fluctuations in the Cp distribution on the panels, due to the WDS wind flow being highly unstable. The 180° wind AOI led to the highest uplift mean Cp equivalent (Cp_{eq}) value on the panels. The 45° and 180° wind AOI were found to induce a Cp_{eq} of significantly higher magnitude on the first panel compared to the second panel, whereas the 0° and 210° wind AOI induced a significantly higher Cp_{eq} magnitude on the second panel compared to the first panel Cp_{eq}. Moreover, the CFD study provided pressure coefficient distribution on the panels and flow visualization when interacting with the panels surfaces. The LES Dynamic Smagorinsky subgrid scale model was found to be more suitable for the WDS numerical replication than the RANS shear stress transport k-ω turbulence model. The LES model showed the fluctuating pressure coefficients on the panels' surfaces, induced by the swirls that were formed post interaction of the wind with the panels.

Acknowledgments

First, I would like to deeply thank my supervisor Dr.Elena Dragomirescu, who supported and guided me throughout every step of this research. I am extremely grateful, and I appreciate all the help she has provided me, along with the countless advice and motivation.

I would also like to thank Zhe Xiao, Majeed Muslim, Gamal Elnabelsya, and everyone that has helped me in this project.

Finally, I would like to dedicate this thesis to my dear family. Without their endless love, prayers and support, I would not be where I am today. They have been, are and will always be my true inspiration.

Contents

List of Figures

List of Tables

Nomenclature

ABL	Atmospheric Boundary Layer
AOI	Angle Of Incidence
ASCE	American Society of Civil Engineers
CFD	Computational Fluid Dynamics
DES	Detached Eddy Simulation
LES	Large Eddy Simulation
MUSCL	Monotone Upstream Centered Scheme for Conservation Laws
NBC	National Building Code
PV	Photovoltaic
RANS	Reynolds-Averaged Navier-Stokes
SEAOC	Structural Engineers Association of California
SST	Shear Stress Transport
WALE	Wall-Adapting Local Eddy-viscosity
WDS	Wind Damage Simulator
A_i	Tributary area (m^2)
$C_{p,eq}$	Equivalent pressure coefficient
$C_{p,lower}$	Lower surface pressure coefficient
$C_{p,net}$	Net pressure coefficient
$C_p(t)$	Time-history pressure coefficient
$C_{p,upper}$	Upper surface pressure coefficient
P_s	Static pressure (Pa)

P_t	Total pressure (Pa)
P_0	Reference pressure (Pa)
$P_0(t)$	Time-history reference pressure (Pa)
$P(t)$	Time-history surface pressure (Pa)
ρ	Air density (kg/m^3)
q	Dynamic pressure (Pa)
$q(t)$	Time-history dynamic pressure (Pa)
μ	Air viscosity (Pa.s)
v_0	Reference velocity (m/s)
v	Velocity (m/s)

Chapter 1 Introduction

1.1 Solar energy systems and wind loading

Fossil fuels have been the main source of energy in the past. However, with the rise of climate change and its negative impacts on the environment, more focus is directed towards renewable energy in order to mitigate these effects. According to a report issued by Natural Resources Canada (NRCan, 2017), one of the fastest growing types of renewable energy in Canada is the solar photovoltaic energy. The solar energy systems are mainly formed of solar cells installed on solar panels or solar trackers, that capture the sunlight and convert it into electricity. This process is environmentally friendly and its increase in usage helps reducing the global warming emissions production (IPCC, 2011). In addition, solar energy technology and applications increase jobs opportunities, since it requires labor due to the need of workers for installments of solar panels, maintenance, and repairment. With this significant increase of focus on solar energy, it is important to design the solar panels or racking system efficiently to resist forces of nature while also being economical, by avoiding any overdesign of the systems.

Solar panels, whether they are roof-mounted or ground-mounted, are often designed according to wind forces since these are most likely to be the critical and governing load. “Winds are caused by differences in atmospheric pressure: the greater the difference, the stronger the wind” (Nkemdirim, 2006). Generally, wind is directed horizontally along the earth surface due to the horizontal wind speed component being more dominant than its vertical component. Adequately understanding the wind effects and the wind-induced pressure distribution on the solar panel surface, allows for better design standards, which will lead to more effective installments. This can be very economical for large-scale solar projects, such as solar farms, since maintenance, repairs and redesigns can be very costly, time consuming and negatively affecting the energy production rate. The adequate structural designing of solar panels systems will help maintain the structural integrity of the supporting systems, thus protecting the large investment of time, money and material. More importantly, this will assure the public safety and will avoid significant structural failures.

According to National Building Code of Canada (NBC, 2015), typical structures are all designed to resist the strongest wind determined for significant large return period. The value of the

reference wind velocity pressure (NBC, 2015, Appendix C-2) used in the design is obtained from historical data that depend on the geographical location and are based on a probability of exceedance in any one year of 1 in 50 (NBC, 2015, Division B). However, for structures such as solar panels, using the static load procedure could be considered inaccurate. Solar systems might be subjected to buffeting which can be due to turbulence, aerodynamic instability, vortex shedding or upwind obstructions. Hence it is recommended in Commentary I, sentence 54 of the User's Guide-NBC 2015: Part 4 of Division B, to conduct a more detailed aerodynamic analysis for solar systems with a natural frequency lower than 10 Hz, since it takes into account the vibrations that may increase the dynamic loading effect (Structural Commentaries, 2015).

The uplift wind pressure is often the major concern for any engineer or designer; this is caused by a negative pressure applied to the surface, which is magnified by separated flow creating conical vortices. Wind uplift force occurs when the pressure below a support is greater than the pressure above, thus creating suction (Aly and Bresowar, 2016). Due to the insufficient understanding of wind-induced effects and provisions regarding the solar panels design for wind loadings, engineers often have to count on their best judgement to obtain the optimum design. In some situations, the design values obtained may be underestimated or overestimated, leading to either structural failures or overdesigns, which can have significant safety or economical consequences (Banks, 2012). Computational fluid dynamics (CFD) analysis can be conducted to develop and understand better wind flow patterns around structures or objects to optimize designs. However, for high turbulent wind scenarios, these estimates are not reliable and precise. According to NBC (2015) Commentary I sentence 5 (Structural Commentaries, 2015), no standards or provisions accept CFD procedures, and it is not allowed to be used solely without experimental wind tunneling for validation of results. Currently, in NBC (2015) there is a section in the commentary specifically for roof-mounted solar panels system design procedure; however, more studies and guidelines are needed for ground-mounted solar panels.

1.2 Research motivation

As mentioned previously, implementing solar energy technology is part of a worldwide vision to help reducing the negative impact of climate change and global warming. In Ontario, the Feed-In

Tariff (FIT) Program, a previous long-term project, allowed energy consumers to participate in the generation of sustainable and renewable energy. Through the FIT program, opportunities were made available for people and communities to reduce their electricity bills or even earn money through the net metering system, where energy generated through solar panels is delivered to the electricity grid and is taken into account with the consumption simultaneously. For small renewable power generation projects (10kW or less), MicroFIT program, which belonged to the FIT program, encouraged solar energy generation for small businesses or homeowners (IESOa, 2019). This allows for a cleaner environment; however, it also increases significantly the usage of solar energy systems. Even though the Minister of Energy terminated this program on December 2016 (IESOb, 2019), new similar projects could emerge in the future.

This implies a significant future growth in solar energy projects, especially for ground-mounted systems due to the fact that these have easier access and maintenance, are less costly and more suitable for big projects. Moreover, a big advantage of ground-mounted solar panels is that, usually, their location is distanced from communities and urban areas; leaving behind smaller probability of large consequences in case of unexpected structural failure.

The solar energy industry has been on a goal, which is to lower the cost of the PV systems as much as possible. According to Cain and Banks (2015), “as industry scales, prices fall” (Figure 1.1), meaning that with the increase of the number of installations, the cost of implementing these solar energy systems decreased. Hence manufacturers of solar racks often rely on modeling their system and running wind tunnel experiments to design more efficiently and to reduce the cost (Cain and Banks, 2015). However, the occurrence of failures on large-scale ground-mounted solar systems will lead to damages which might become greater than the savings of a more economical design. This shows the importance of further research regarding wind effect and loadings on the solar energy systems in order to foresee and prevent structural failure.

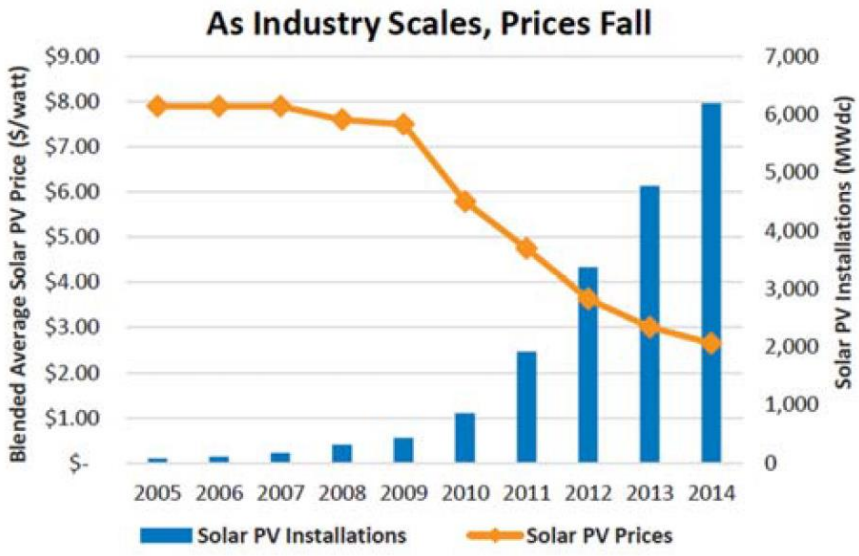

Figure 1.1 Growth trend of the solar PV industry (Cain and Banks, 2015)

The current study performed for ground-mounted solar panels was also motivated by the fact that over the past years, most studies were conducted on roof-mounted solar systems, because it is less challenging than ground-mounted solar systems. Ground-mounted solar panels are often situated in the lower part of the boundary layer wind profile, where the flow is highly turbulent, and it is difficult to replicate its effects on scaled modules in a wind tunnel. Full-scale wind tunnel testing is difficult to achieve due to model dimensions and blockage restrictions, hence there are limits for scaling the specimens. Also, replicating turbulence on small-scale models can lead to inadequate results. NBC Structural commentaries (2015) contains design steps (Commentary I paragraphs 56 and 57) that can be followed for roof-mounted solar arrays, but still there is not enough guidelines nor regulations for ground-mounted systems. Before the development of design guidelines, further research regarding the wind effect on ground-mounted solar panels is deemed necessary for safety and economical reasons, especially since growth is being witnessed regarding the scale of solar energy industry, such as the Quaid-e-Azam Solar Power (QASP) system as can be seen in Figure 1.2.

Figure 1.2 QASP solar system. Photo credit Quaid-e-Azam Solar Power (Pvt) Ltd. Retrieved from: https://www.dawn.com/news/1209933

In addition, in 2018 a new facility was developed at the University of Ottawa, the Wind Damage Simulator (WDS), which also motivated this study. This facility is capable of simulating wind loading through a suction outlet located at the middle of the facility ceiling connected to an industrial blower, as detailed in Chapter 3. Air is extracted through the top suction outlet and it can be drawn inside the box by opening one or several inlets, located on each lateral wall of the facility, depending on the experimental procedure and flow characteristics desired. The WDS is still a new facility, and this is the first experiment conducted in it, hence further investigations and work are needed to be performed in the future, regarding wind flow specifications and the setup procedures for the WDS facility, to reach its full potential.

1.3 Research objectives

The current research project is planned to be conducted at the newly constructed WDS facility at the University of Ottawa with the main objective of obtaining the wind-induced pressure coefficients distribution on the ground-mounted solar panels. After obtaining the experimental results, they will be compared with a previous experimental study (Samani, 2016) conducted on a

similar solar panels and rack of similar characteristics; however, through a different wind tunnel facility called WindEEE Dome at Western University. This will allow for a comparison of the two facilities and provide a better understanding of the WDS.

Furthermore, Computational Fluid Dynamics (CFD) analysis is also planned to be conducted to determine the wind flow characteristics, which otherwise cannot be visualised during the experiment. The wind-induced pressure coefficient distribution on the solar panels and flow behaviour will be determined from the CFD simulations.

Finally, the numerical results are to be compared with the measurements obtained through the experiment conducted in the WDS facility. In addition, this CFD study will allow for a better interpretation and understanding of the pressure coefficient distribution on the surfaces of the panels through the visualization of the flow behavior, and will clarify the appropriate CFD methodology to follow, such as turbulence models and solvers, for replicating the wind flow conditions in the WDS experimental facility for future research studies.

1.4 Scope of the research

The model tested in the current study consists of two solar panels, ground-mounted and supported by an aluminum frame with an inclination angle of 25°. The dimensions are two 985 mm × 1,960 mm panels with a 20mm gap in between, as shown in Figure 1.3 below. These configurations were based on the geometry of the solar panels used by Samani (2016) in a wind tunnel experiment, for comparison reasons, and for better evaluation of the results obtained in the WDS facility.

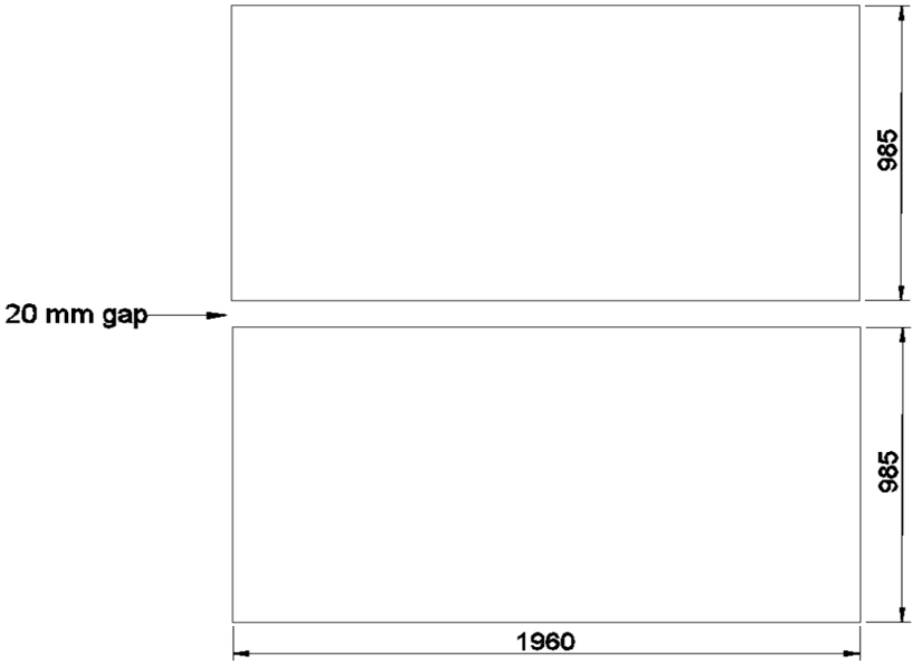

Figure 1.3 Solar panels with gap (dimensions in mm)

In the current research, the panels are represented by two plates of plywood and the frame was made by using P1000 aluminum Unistrut cross section, constructed at the University of Ottawa laboratory. Six wind angles of incidence were tested (0°, 30°, 45°, 180°, 210°, and 225°) under 14 different wind speeds, ranging from 14 m/s to 42 m/s, with around 2 m/s increments. The pressure coefficient distribution along the panels surfaces is determined and analyzed.

Moreover, three-dimensional CFD studies were carried out using STAR-CCM+ software. The solutions were based on Large Eddy Simulation (LES) turbulence model; however at first, the Reynolds-Averaged Navier-Stokes (RANS) model was used until convergence was attained, to obtain the initial conditions for the LES model. The results were then analyzed to understand the pressure coefficients distribution and were compared with the experimental reults. Conclusions were drawn regarding the CFD methodology and the WDS facility functionality.

1.5 Thesis layout

The main objectives and motivations of the current research are stated in Chapter 1 along with the scope of the research. It allows to obtain a general idea about this research and covers briefly the cases considered and the research methodology.

Chapter 2 provides background information and the literature review on the ground-mounted solar panels topics, presenting previous studies related to it, along with the theory and formulas required to determine the wind pressure coefficients on the solar panels surface. It also allows for a general idea about the ground-mounted solar panels studies and provides an overview regarding the CFD modelling approach that has been used previously for wind effect on solar panel studies.

Chapter 3 covers the experimental test setup, along with information about the new WDS experimental facility at the University of Ottawa. This chapter covers the experimental model adopted in the current study, the dimensions and the wind angle of incidence cases that were considered, along with the solar panel support system constructed.

The results of the laboratory experiments are analyzed, presented, and discussed in Chapter 4. The pressure coefficients values are determined along the panel surfaces, and for each case a graphical representation was created along three different lines: inlet-line, mid-line and edge-line. Contours are created for the pressure coefficients distribution on the upper surface, lower surface, and for the net pressure coefficients on the panels. This allows for a better understanding of the tested cases and for a comprehensive comparison with the selected cases from a previous wind tunnel study (Samani, 2016).

Chapter 5 focuses on the CFD simulations, methodology used (RANS/LES), and the pressure coefficients results, along with their comparison with the experimental data, for a better understanding of the pressure coefficient distribution and the CFD models associated with the WDS facility.

Finally, Chapter 6 contains discussions and conclusions that were drawn from the experimental and numerical results. Limitations encountered in the current research are also presented, along with the recommendations regarding future research especially for the newly developed WDS facility at the University of Ottawa.

Chapter 2 Literature Review

When wind-induced damages on solar panels (PV) take place, economical consequences can be frustrating for the project investors and system designers economically and timely. Failures could interrupt the energy production, would require repairments or even in some cases redesigns and installations of updated models. In order for the future generations to effectively rely on solar energy systems, more studies are needed.

2.1 Wind induced pressure on solar panels

Unlike streamlined bodies, when a bluff body is subjected to wind, a separation of the flow at the leading-edge corners and a surface pressure on the body takes place along with vortex generation, as shown in Figure 2.1 (Holmes, 2015).

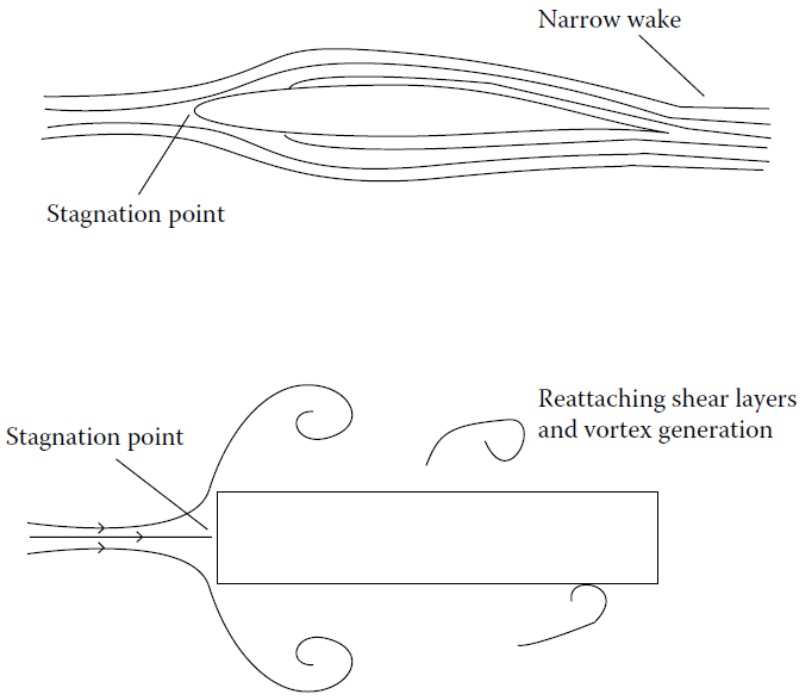

Figure 2.1 Steady flow around streamline and bluff body (Holmes, 2015)

2.1.1 Evaluation of wind-induced pressure

When wind streamlines attach or detach from the surface of an object, these will induce positive or negative pressure. Bernoulli's equation (Eq. 2.1) describes the relationship between the static pressure P_s (Pa), the dynamic pressure q (Pa) and the total pressure P_t (Pa) (Holmes, 2015):

$$P_s + q = constant = P_t \tag{2.1}$$

where the dynamic pressure q is a function of the velocity v (m/s) and the density ρ (kg/m^3) as follows:

$$q = \frac{1}{2}\rho v^2 \tag{2.2}$$

Considering the static pressure and the wind velocity at the region outside of the body's influence (reference point) as P_0 and v_0 respectively, the following relationship can be determined:

$$P_s + \frac{1}{2}\rho v^2 = P_0 + \frac{1}{2}\rho v_0^2 \tag{2.3}$$

Re-writing Eq. 2.3 leads to:

$$P_s - P_0 = \frac{1}{2}\rho(v_0^2 - v^2) \tag{2.4}$$

2.1.2 Pressure coefficient

Due to difficulties in using different and numerous parameters associated with the wind pressure measurements, it is preferable to employ the pressure coefficient, a non-dimensional parameter, for comparisons between different studies. The pressure coefficient, C_p, expresses the dimensionless surface pressure of the object, and can be obtained by the following equation (Holmes, 2015):

$$C_p = \frac{P - P_0}{q} \tag{2.5}$$

where P is the surface pressure. A positive C_p means that the flow is directed towards the considered surface inducing positive pressure, whereas a negative C_p signifies that the flow is moving away from the considered surface, inducing suction.

For evaluating the wind-induced effect on solar panels, it is essential to determine the net pressure coefficient (Eq. 2.6), which can be obtained by simultaneously taking the difference of the pressure coefficient exerted on the upper surface of the panel and the pressure coefficient exerted on the lower surface of the panel.

$$C_{p,net} = C_{p,upper} - C_{p,lower} \tag{2.6}$$

2.1.3 Equivalent pressure coefficient

The pressure coefficient is the non-dimensional coefficient associated with the pressure for a certain location (pressure tap) on the surface; however, the equivalent or area-averaged pressure coefficient allows for the determination of a single equivalent pressure coefficient value for the entire model. This can be obtained by the following equation:

$$C_{p,eq} = \frac{\sum_{i=1}^{n}(C_{p,net,i} \times A_i)}{\sum_{i=1}^{n} A_i} \tag{2.7}$$

with A_i being the tributary area of each pressure tap.

2.1.4 Reference pressure

To determine the pressure coefficient correctly, the reference pressure must be the one corresponding to the static pressure of the fluid, which is not affected by the presence of the structure being tested. In the case of a plenum, which is similar to the WDS facility testing chamber, the plenum pressure (shown in Figure 2.2) is often used as the reference pressure as long as its value is identical to the stream static pressure (Müllenbach and Deutenbach, 1991). If there is a difference between the stream static pressure and the plenum pressure due to blockage or other reasons, the reference pressure should be the one corresponding to the fluid dynamic equivalent pressure. In addition, to avoid any risk of having the measured dynamic pressure affected or altered by the blockage, one can determine the dynamic pressure accurately by obtaining only the nozzle pressure difference (Müllenbach and Deutenbach, 1991).

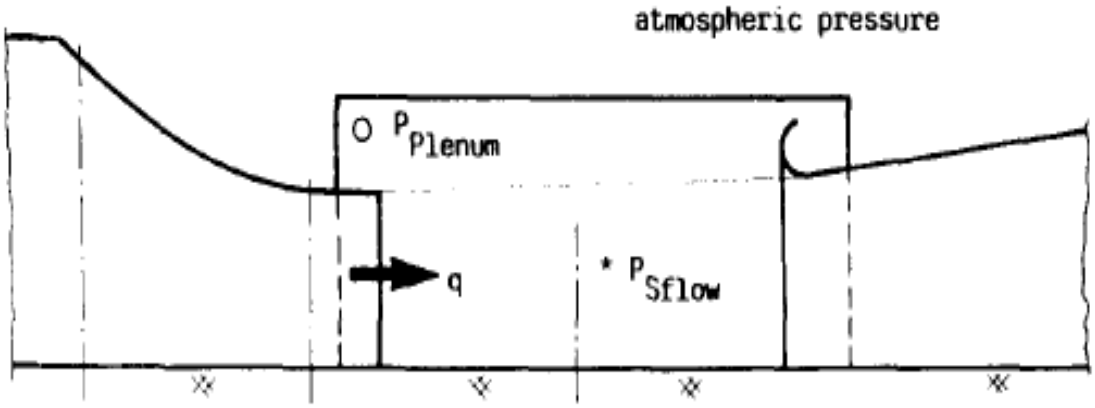

Figure 2.2 Wind tunnel schematic (Müllenbach and Deutenbach, 1991)

2.2 Experimental investigations and solar panels

Throughout previous investigations, it is common that experimental testing such as wind tunnel experiments is preferred over full-scale outdoor testing due to time, cost and uncertainty reasons. Nevertheless, wind tunnel can still be costly and consumes significant amount of time to set up and run customized tests. Wind tunnel testing is recommended for unusual shaped structures or in the cases where the wind loading effects are critical such as for solar panel structures (Mehta and Coulbourne, 2010). Several guidelines such as ASCE 49-12 (2012) exist to give guidance and restrictions for wind tunnel testing to satisfy certain criteria; hence, most ground-mounted solar systems studies are conducted on scaled models instead of full-scale specimens due to many difficulties, and by using the ABL (Atmospheric Boundary Layer) wind tunnel method**.**

2.2.1 Background of experimental investigations on solar panels

The first wind tunnel was designed and built in 1871 by Francis H. Wenham, a council member of the aeronautical society of Great Britain. In order to understand wind effects on photovoltaic panels, wind has to be applied on the model, to replicate the outdoor wind conditions for design purposes. From the wind tunnel experiment, the wind pressure coefficients can be determined at certain locations on the panels, which will allow for better understanding of wind load distribution

and wind-induced effects on the structure, thus leading to safer design codes and recommendations. Wind tunnel facilities allow for the replication of the wind conditions similar to the natural wind, whether it is the wind profile, turbulence, or wind velocity, depending on the location and the required model-testing specifications. If the experimental conditions are proven correct and adequate, wind tunnel experiments are the only method that gives the designers the information to implement into projects where the calculated critical load is in fact lower than the value specified in the design codes. However, if the experiment conditions would be faulty, using the wind tunnel method will most likely increase the probability of having under-designed structures that could lead to potential failures. Hence, in order for designers to get credible results from their experiments, they must meet certain provisions and requirements, whether it is related to the instrument implementation or model configuration, depending on each case scenario (Banks, 2012).

The number of studies conducted on roof-mounted solar systems is much larger when compared with the investigations for ground-mounted solar systems. Many factors can influence the wind loads distribution and the pressure coefficients values on the surface of the solar panel, such as the scale factor, inclination angle, wind speed and direction (wind angle of incidence), geometry, ground clearance, gap dimension, etc. Studies on ground-mounted solar panels are more challenging to perform since they are usually located in the low region of the frictional influence, known as the atmospheric boundary layer due to the roughness of the terrain. The flow in this region is more turbulent, which makes it more difficult to be simulated in the laboratory. Another reason that adds to the difficulty of conducting wind tunnel experiments on ground-mounted solar panels is that the scale factor for ground-mounted is recommended to be small in order to eliminate potential errors in the results. Model dimensions can lead to an incorrect prediction of the wind effects due to flow interference with the measuring devices, low pressure taps resolution, and difficulty for the flow to represent the required turbulence for small-scale structures. So typically, experimental ground-mounted solar panels studies are conducted on large-scale models, bigger than what is normally used in most boundary layer wind tunnels, such as 1:500 to 1:100 scale (Aly and Bitsuamlak, 2013).

2.2.2 Previous experimental studies on ground mounted solar panels

Abiola-Ogedengbe (2013) conducted a study on a 1/10 scaled photovoltaic module (shown in Figure 2.3) in the Boundary Layer Wind Tunnel I (BLWTI). Two panel inclination angles (25° and 40°), and four different wind angles of attack (0°, 30°, 150° and 180°) were considered. Results lead to the conclusion that the critical wind uplift scenario occurred at the angles 150° and 180°, with the greatest uplift occurring at the leading edge of the module. Particle Image Velocimetry (PIV) was used in the experiment for the 0° wind angle of attack. The presence of the gap between the 24 small panels (Figure 2.3) that constitute the tested solar panels led to a decrease of the pressure coefficient (Cp) values for the 0° case and an increase of Cp for 180° case. The Cp distribution on the tested module was found to be symmetrical for the 0° and 180° angles of attack and asymmetrical for the 30° and 150° angles of attack. Regarding the inclination angle of the panels, it was concluded that the 40° panel inclination angle led to a more critical wind effect than the 25° case. Moreover, a conclusion was made regarding the gaps effect on the wind flow, where the wind was directed through the gaps towards the panel's underside, for the 0° wind direction. The gaps led to a turbulence increase, flow acceleration and an alternation of the surface pressure distribution. The largest turbulence zone was observed at the downstream of the flow beyond the trailing edge of the panel.

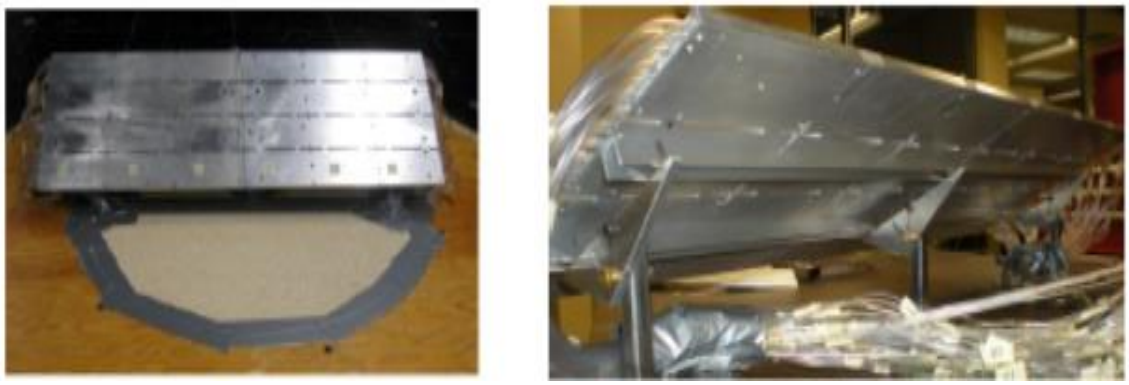

Figure 2.3 Photovoltaic scaled module (Abiola-Ogedengbe, 2013)

Aly and Bitsuamlak (2013) carried out wind effect investigations on ground-mounted solar panels with different model scales (scale 1:5 module shown in Figure 2.4). It was concluded that for the smaller scale tested modules, higher root mean square and peak pressures were observed. The mean loads values were found not significantly affected by turbulence, except for the case when

the models had a very small scale, due to the wind speed uncertainty caused by being very close to the ground.

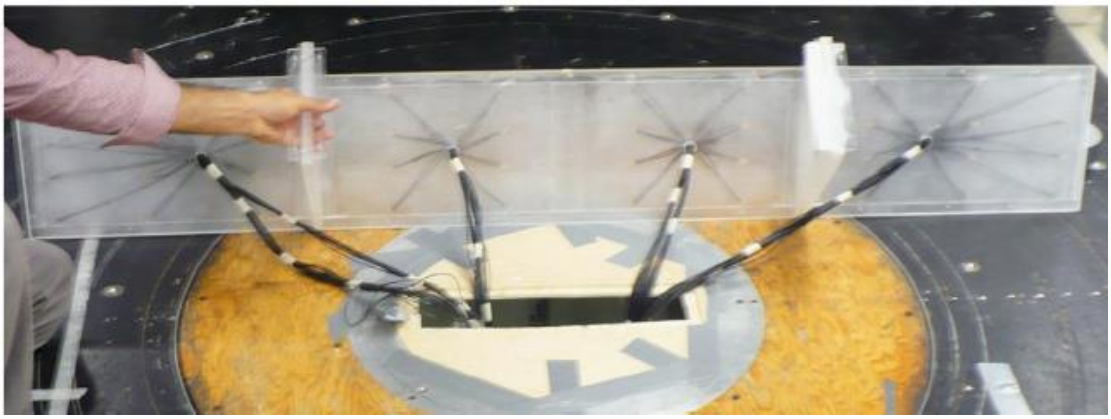

Figure 2.4 Ground-mounted solar panel module, 1:5 scale (Aly and Bitsuamlak, 2013)

Samani (2016) conducted an experimental study on full-scale solar panels, with a 20mm gap between them, as shown in Figure 2.5, using the hexagonal wind tunnel, the WindEEE Dome facility from the Western University, Ontario. Wind-induced pressure distribution was determined on the panels with an inclination of 25° for 21 wind directions (10° intervals from 0° to 180° in addition to 45° and 135°) and the response of the solar panel support racks was obtained based on the force balance tests. Also, the solar panel support rack was evaluated through a finite element analysis and the design improvement for the supporting structure was proposed. It was found that for 0° and 180° wind directions, the system underwent the most critical positive and negative pressure coefficients, respectively, with a symmetrical distribution about the centerline. The 20mm gap presence between the two panels affect the Cp distribution by causing a decrease along the direction of the flow. The equivalent pressure coefficient study concluded that the maximum pressure occurs for the 180° wind angle of incidence. For comparison and evaluation reasons of the new WDS facility, the tested module of the present study is based on the same solar frame materials, module geometry conditions (inclination angle, gap presence, etc.) that are used by Samani (2016), as detailed in the experimental procedure described in Chapter 3.

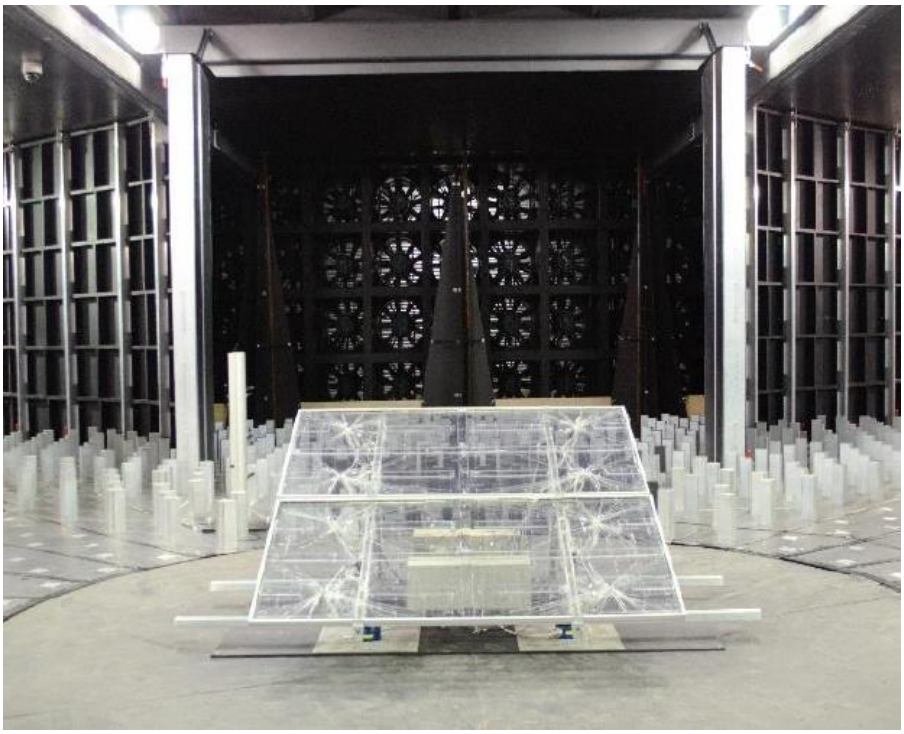

Figure 2.5 Testing module in WindEEE Dome (Samani, 2016)

2.3 CFD investigations and solar panels

Computational Fluid Dynamics (CFD) can also be used to conduct studies for wind flow behaviour and wind effects on solar panels. It is essential for CFD results to be compared with experimental data to validate the simulation methodology implemented in the CFD. If the validation is not performed, the simulation results obtained from CFD could be incorrect and could lead to serious negative consequences; therefore, they are considered inadequate and have to be disregarded (Banks, 2012).

2.3.1 Background of CFD investigations on solar panels

Computational Fluid Dynamics, a "transportable wind tunnel" (Anderson, 1995), allows for scientists to analyze and predict fluid flow situations by solving complex numerical equations. In general, three principles govern the physical aspect of CFD or the mathematical equations (Anderson, 1995):

- Conservation of mass
- Newton's Second Law (Force = mass × acceleration)
- Conservation of energy

Through modern technology and powerful computers, this mathematical modeling tool can be used to solve complex fluid flow problems and predict airflow behavior and its effects on structures. Solving complex fluid flow problems manually is considered impossible due to the required manipulations (iterations) of extremely numerous digits, in the order of thousands, to even millions (Anderson, 1995). Although CFD cannot be used solely as a mean to obtain critical results for design purposes yet, it is a good tool to validate with the wind tunnel results for predicting wind flow behaviour and effects on specific structures. Also, studying different preliminary design approaches, that could potentially mitigate these wind effects, can be employed with the help of CFD solutions. The CFD approach is more economical than the wind tunnel tests and allows for the testing of any scale, geometry or flow property; however, it is difficult to be validated since its outcome is based on the user's adopted methodology (computational domain and grid, boundary conditions, turbulence models, etc.). In the future, with more research being conducted on CFD, this could become an adequate and validated method to be used solely in designs with proper design codes and provisions. However, presently, the CFD results must be compared against the wind tunnel studies, to be considered valuable and to be certain that the boundary conditions and the parameters have been defined properly in the software (Banks, 2012).

There are guidelines and geometry recommendations to simulate a virtual wind tunnel in CFD; however, the WDS facility is different than the typical wind tunnel, thus the previous CFD guidelines are not applicable and customised conditions must be defined in order to obtain adequate results. The computational domain (geometries) should be represented accurately, with as much details as possible surrounding the region of interest. This also applies for the computational grid (meshing), where the greater number of cells is used the more accurate the results become; however, having numerous cells in the computational grid could lead to a computationally prohibitive analysis. Hence, it is recommended to implement local mesh refinement around regions of interest or regions that will most likely undergo large flow properties changes (Casey and Wintergerste, 2000). COST (Franke et.al, 2007), a CFD practice guideline, emphasizes on keeping the truncation errors small by having a small grid stretching in the regions

with expansion ratio value lower than 1.3. In addition, it is preferable to use hexahedral cells instead of tetrahedral with a minimum of 10 cells per cube root of structures volume due to the fact they allow for smaller truncation errors and better convergence (Franke et al., 2007).

Boundary conditions also play an important role in the accuracy of the results so they must be properly defined for each CFD simulation. Regarding the turbulence models, in typical ground-mounted solar panels studies the Large Eddy simulation (LES) model or the Reynold-Averaged Navier-Stokes (RANS) have been previously used (Bitsuamlak et al., 2010, Aly and Bitsuamlak, 2013, Jubayer and Hangan, 2014, Shademan et al., 2014). In general, LES is preferred when calculating wind velocities and uplift pressure forces on structures (Kim, 2014); however, it is more computationally and time expensive than the RANS approach. LES requires more grids and more computing resources for calculations to provide efficient results when compared with the RANS turbulence model (Franke et al., 2007).

2.3.2 Previous CFD studies on ground mounted solar panels

Bitsuamlak et al. (2010) conducted a CFD study on a ground-mounted solar panels under Atmospheric Boundary Layer (ABL) flow conditions. The CFD results were compared with the results of a previous full-scale experiment carried out at the Wall of Wind (WoW) testing facility located at Florida International University (FIU). Two CFD techniques were implemented: the Reynolds-Averaged Navier-Stokes (RANS) to determine the initial conditions to be used by Large Eddy Simulation (LES), which is considered a more accurate technique for highly turbulent flows. The case of 180° wind AOI induced the most critical wind loads on the solar panels. Although some agreement was present between the CFD and experimental results, it was found that the LES technique resulted in underestimated mean pressures when compared with the full-scale measurements (Figure 2.6).

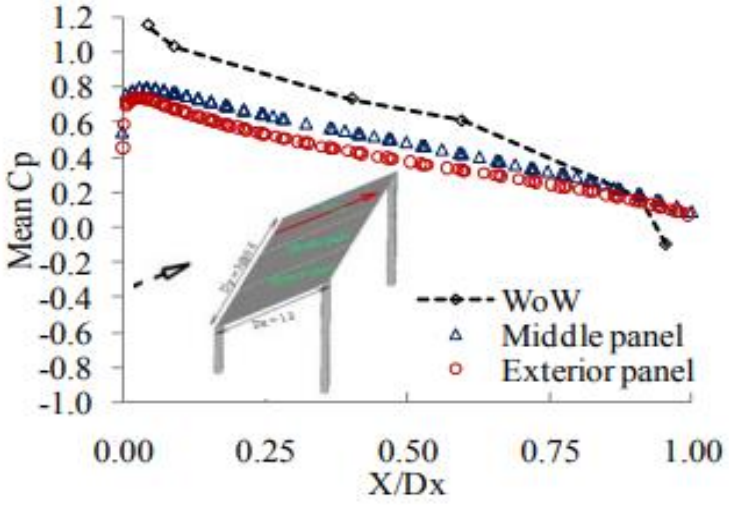

Figure 2.6 Comparison between CFD and experimental results for 0° wind angle of incidence (Bitsuamlak et al., 2010)

Aly and Bitsuamlak (2014) conducted experimental and CFD studies on the ground-mounted solar panel models to investigate how the geometric model scale influences the pressure distribution. It was concluded that the scale factor did not affect significantly the mean pressure coefficients. However, the model size along with the inflow turbulence did alter the peak pressure coefficients. It was also found that the CFD Large Eddy Simulations (LES) resulted in a very good agreement with the experimental results, as can be seen in Figure 2.7.

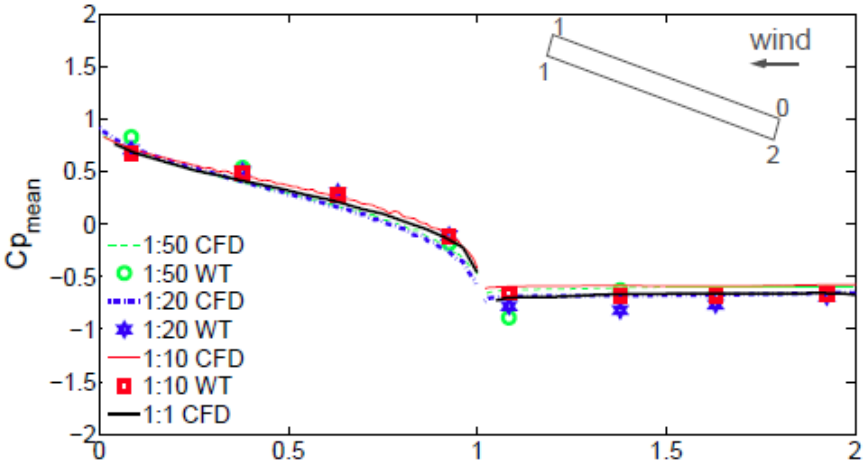

Figure 2.7 Mean pressure coefficients along the mid-line of the panel (Aly and Bitsuamlak, 2014)

Jubayer and Hangan (2014) conducted a CFD study that investigated the wind load and flow field features for a ground-mounted stand-alone panel system immersed in Atmospheric Boundary

Layer (ABL) for different wind directions, using Unsteady Reynolds-Averaged Navier-Stokes (URANS) simulations. The system had a 25° inclination angle, and the wind AOI ranged from 0° to 180°, at 45° intervals. The CFD results were compared against the wind tunnel measurements obtained by Abiola-Ogedengbe (2013) and a 46% agreement was concluded (comparison for the 180° AOI cases shown in Figure 2.8). Maximum overturning moment occurred for the 45° and 135°, whereas the maximum critical uplift pressure was noticed for the 180° wind AOI.

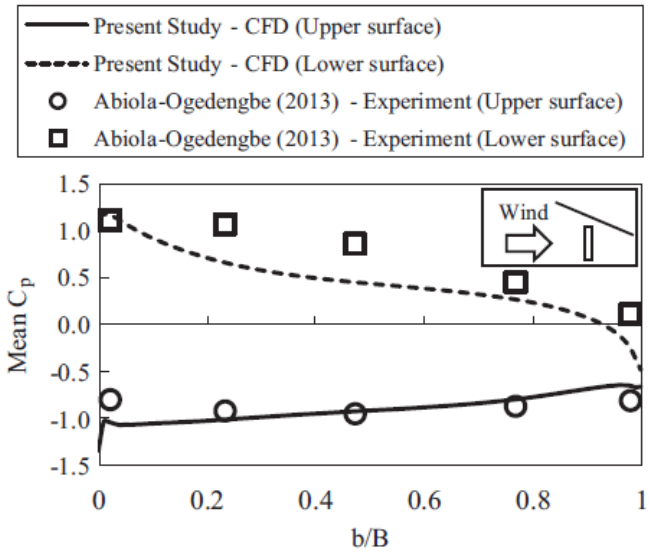

Figure 2.8 Mean Cp profiles along the mid-line of the panel surfaces comparison (Jubayer and Hangan, 2014)

Shademan et al. (2014) carried out CFD simulations of wind loading on ground-mounted solar panels at different flow configurations. The analysis, on a stand-alone solar panel consisting of four individual panels in a 2×2 arrangement (Figure 2.9), was done by using steady three-dimensional RANS simulations, and the results of several flow parameters were compared with the experimental data. From this study, it was concluded that the maximum wind induced loads occurred for the wind angles of attack of 0° and 180°. In addition, the gap spacing between the panels was found to create regions that underwent large wind loading and contributed to formation and shedding of additional vortices. Also, increasing the ground clearance led to an increase in mean wind loads on the panels.

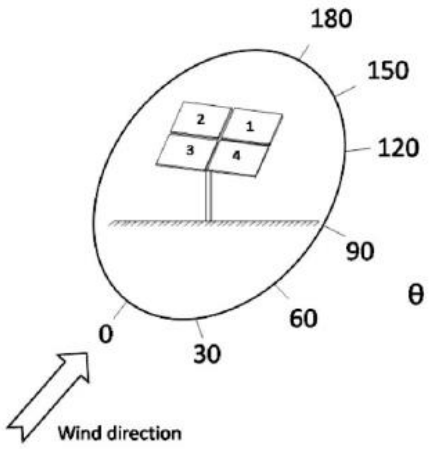

Figure 2.9 Solar panels 2x2 arrangement with wind direction angles (Shademan et al., 2014)

Aly and Bresowar (2016) investigated the model scale and the inflow effects on the pressure distribution for ground-mounted solar panels. High similarity of mean and peak pressure distribution through CFD (LES model) was observed, when compared with experimental results. Lack of large-scale turbulence in the wind tunnel experiment led to lower pressure results than those obtained through CFD LES model for panels at scales ranging from 1:10 to 1:50. A three seconds data analysis approach was presented in this investigation, which serves for consistency in peak wind pressure estimations, as shown in Figure 2.10.

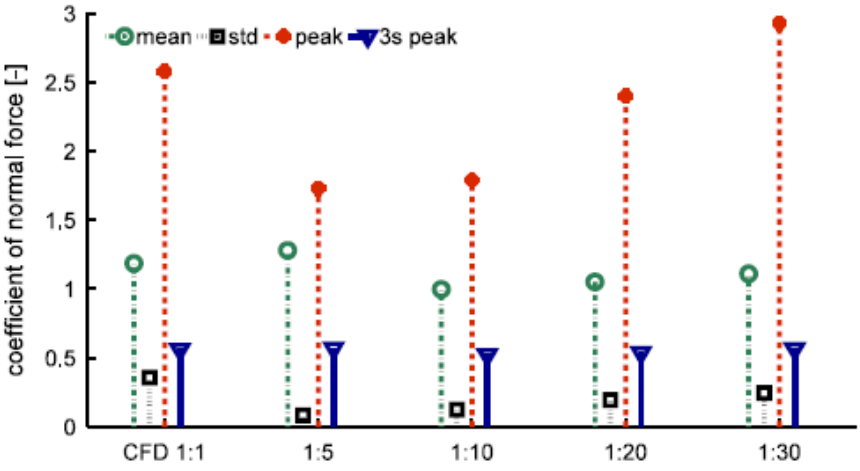

Figure 2.10 Experimental and CFD normal force coefficients comparison (Aly and Bresowar, 2016)

2.4 Design guidelines and for solar panels

The focus of designers and researchers has been shifted more towards the roof-mounted solar systems for several reasons; the main reason is that they are often located near residencies (on buildings), hence resulting in higher danger and risk to human life than ground-mounted solar systems. As mentioned previously, there are several design guidelines for roof-mounted solar panels. In the Structural Commentaries (2015) of National Building Code of Canada 2015 Part 4 Division B, the commentary I contains wind loading design requirements for roof-mounted solar arrays limited to only flat modules and panels, with a natural frequency higher than 10 Hz, to avoid wind-induced vibrations (Paragraphs 53 and 54 of Commentary I). The following are the conditions that have to be met by the designers in order to be able to use the procedure located in paragraph 57:

- Enclosed and partially enclosed structures
- Low slopped roofs (flat or gable or hip with slope < 7°) buildings with any height
- h_2: height of the upper edge of a panel above the roof ≤ 1.2 m
- h_1: height of the lower edge of a panel above the roof ≤0.6 m
- L_p: Length of the panel chord ≤2.0 m

It is mentioned that wind uplift forces on the panels get stronger with the increase of height or length of the panels. Same occurs with the presence of parapets on the roof and building sizes (Paragraph 57, Commentary I, Structural Commentaries 2015).

Pressure equalization factor can be included in the calculation which will help reducing the wind loads. This case is valid for panels that are low enough (less than 250 mm height from the roof's surface) and contain a minimum gap of 6 mm between panels, for every 2 m or more along a row and between each row of the solar array. The pressure equalization factor is directly dependent on the tributary area (Figure I-6 in Commentary I); the larger the tributary area, the lower the solar array pressure equalization factor leading to a lower design wind load. In addition, the location of the panel also affects the wind load, hence in Figure I-8 of the Commentary I roof zones are illustrated, since for each roof zone the pressure gust coefficient is different. Edge exposure conditions for the panels can worsen the wind effects, therefore an Edge factor should be included in the calculations to increase the wind load value where applicable such as for the panels located

around the edge of the roof or solar array (Paragraph 56 of Commentary I, Structural Commentaries 2015).

Prior to the development of design provisions for roof-mounted solar systems, the components and cladding provisions were used to obtain the design wind pressure on the solar panels, which most likely resulted in over-designs due to the absence of pressure equalization factors (Cain and Banks, 2016). In addition to the Structural Commentaries (2015) procedure, the Structural Engineering Association of California (SEAOC) published the "Wind Design for Low-Profile Solar Photovoltaic Arrays on Flat Roofs" paper (PV2-2012). This document is referred to by the Structural Commentaries (2015) procedure in cases where the roofs are not rectangular, and guidance is needed to determine roof zones. The ASCE7-16 included the SEAOC PV2-2012 method with some modifications. The open buildings method may be used in stand-alone ground-mounted solar systems, however there are no specific provisions. ASCE7-16 also provides design provisions for panels parallel to pitched roofs, known as "flush-mounts", that are discussed and for which recommendations are provided in the latest SEAOC "Wind Design for Solar Arrays" PV2-2017 paper. The ASCE7-16 developed new geometric regulations such as the minimum gap of 0.25 inches between panels for pressure equalization, which increases the safety for the flush-mount solar arrays on residential buildings and predicts wind load more adequately (Cain and Banks, 2016).

From the literature review presented above, it can be concluded that a clear lack of wind design guidelines for the application of ground-mounted solar panels is present. Thus, the current research, carried out in the WDS facility, will treat the wind-induced pressure coefficients along the upper and lower surfaces of ground-mounted solar panels and will estimate the critical cases for which the effects will be the most dominant.

Chapter 3 Experimental Test Setup

3.1 Wind-induced Damage Simulator Facility

Most of the wind tunnels used to replicate wind flow are limited to low to medium wind velocity. However, with the current climate change and the increase of wind speeds intensity, it is important to replicate higher wind speeds and wind induced pressures in order to understand and prevent structural damages caused by wind hazards such as tornados and hurricanes.

The multi-hazards research team from the University of Ottawa and Carleton University built the Wind-damage Simulator (WDS), a steel box formed of plate reinforced with HSS members. Through combining wind tunnel techniques with the mechanical up-lift chamber concepts, the WDS facility is able to simulate full-scale winds for close to real windstorm conditions on full-scale structures. Limitations often occur when laboratory conditions prevent replicating the actual physical phenomena encountered in nature; however, the WDS is capable of simulating high wind speeds entering the box through the lateral inlets (Figure 3.1, Figure 3.2), which are directed upwards to the center of the ceiling through the suction created by the industrial blower (Figure 3.1, Figure 3.3), thus inducing uplift forces on the tested models. This is combined with the effect of the incoming wind speed released from several lateral inlets that will alternate such that the desired level of turbulence and gustiness can be obtained along the sides of the investigated model. It has a wide variety of usage purposes, such as understanding wind behavior and forces distribution around surfaces, visualizing failure mechanism of structural components, verifying structural integrity of investigated design models, and recommending the necessary updates for the design codes provisions.

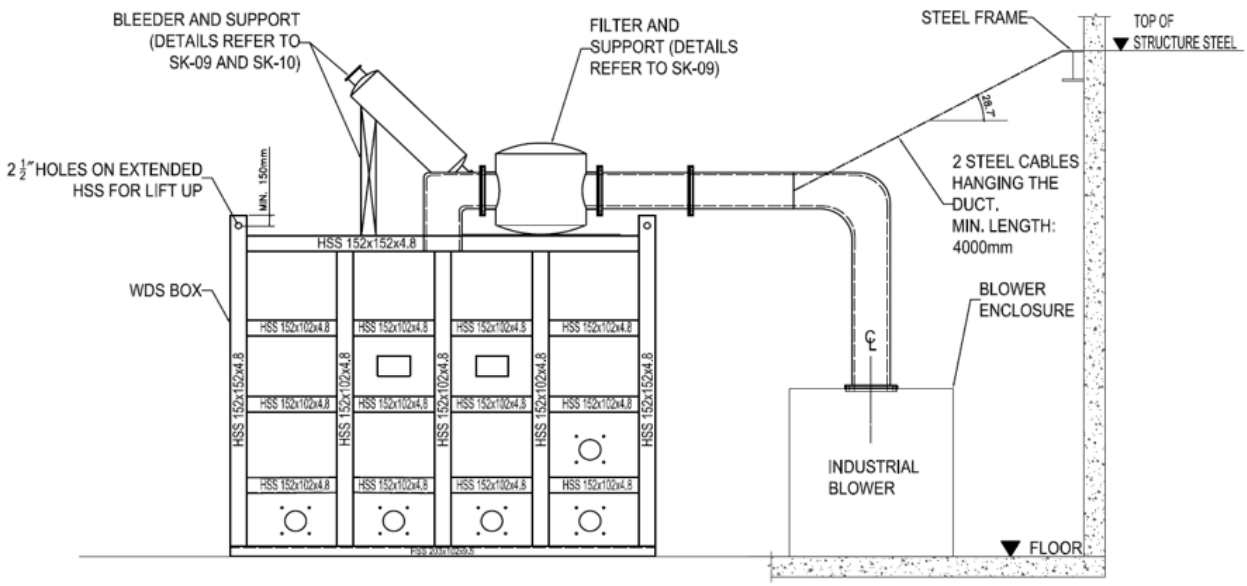

Figure 3.1 WDS facility drawing side view

Figure 3.2 WDS facility with front inlets

Figure 3.3 WDS industrial blower

The geometry dimensions of the WDS facility (shown in Figure 3.1, Figure 3.2) are as following:

- 3.65m width × 3.65m length × 3m height steel box
- 300mm diameter outlet at the center of the ceiling
- 5-200mm diameter inlets on each lateral wall (4 inlets at 250 mm circle center height and 1 inlet at 950 mm circle center height)
- 6.35mm steel plate reinforced with HSS members
- 6 windows for observation
- Steel plate with threaded holes at the bottom

As mentioned previously, the WDS is still newly developed and further studies shall be conducted regarding the wind flow behavior for different setups (inlet openings) and the turbulence details inside the facility. The heights of the inlets may differ in the future, depending on the floor base inside the WDS. Currently, this laboratory is used to test wind pressure distribution on ground-mounted solar panels and to certify for different effects induced by high wind velocities. The

current experiment is the first experiment conducted in the WDS facility, hence, many difficulties are still to be solved while further research is planned in order to allow for full understanding of the WDS facility in order to reach its full potential.

3.2 Testing model and dimensions

The solar panels dimensions considered in the current study are obtained from Samani (2016) for comparison reasons. In this study, two 985 mm × 1,960 mm pieces of plywood with a thickness of 12.7 mm were used to represent the solar panels (full-scale model). The surface was smoothed in order to avoid any possible effects on the results due to module surface roughness. A 20mm gap was also adopted between the two panels, similar to Samani (2016), along with the panels' inclination angle of 25°. The height of the lower edge of the first panel above the ground is around 106 mm whereas the height of the upper edge of the second panel above the ground is 947 mm.

The stand-alone solar frame was constructed at the University of Ottawa lab, using the unistrut P1000 aluminum material, with the cross-section as presented in Figure 3.4.

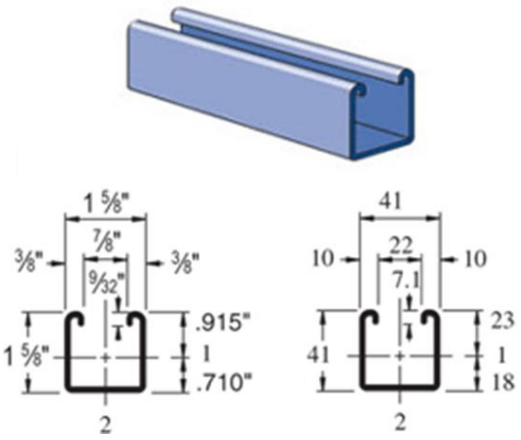

Figure 3.4 P1000 cross-section (Retrieved from: https://www.unistrutohio.com/p1000)

The plan and section view of the frame that supports the solar panels at a 25° inclination angle is represented in Figure 3.5, which is similar to the one used by Samani (2016).

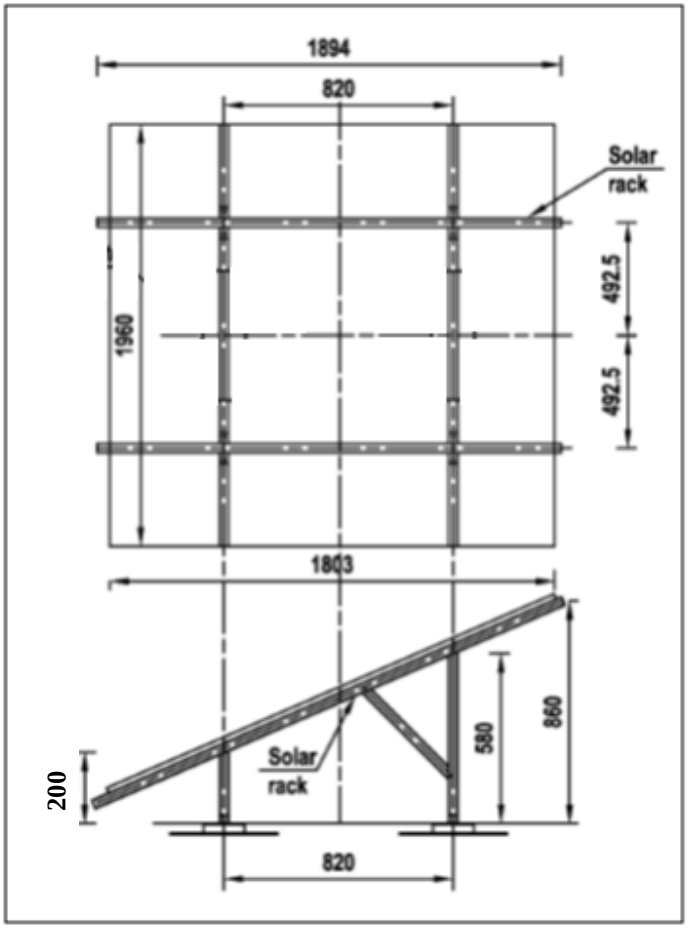

Figure 3.5 Solar support plan and section view (modified from Samani (2016))

3.3 Test procedure and instrumentation

To conduct the experiment, the two plywood pieces, representing the full-scale solar panels, were attached to the frame and placed inside the WDS. The location of the solar panels was chosen in the middle of the facility, such as the centroid of the panels to be located at the center of the WDS. Wind speed was applied on the model from several directions through two mid-inlets. For different wind direction cases, the panels were rotated for each desired angle, while keeping its centroid in the same location to form the wind angle of incidence required with respect to the inlets. To access the inside of the WDS facility, the box is carefully lifted by the crane and it is placed away from the panels. By closing the inlets and leaving only two of them open, the wind is directed towards the panels through suction that is applied by the blower at the outlet located at the middle of the ceiling of the WDS facility, as shown in Figure 3.6.

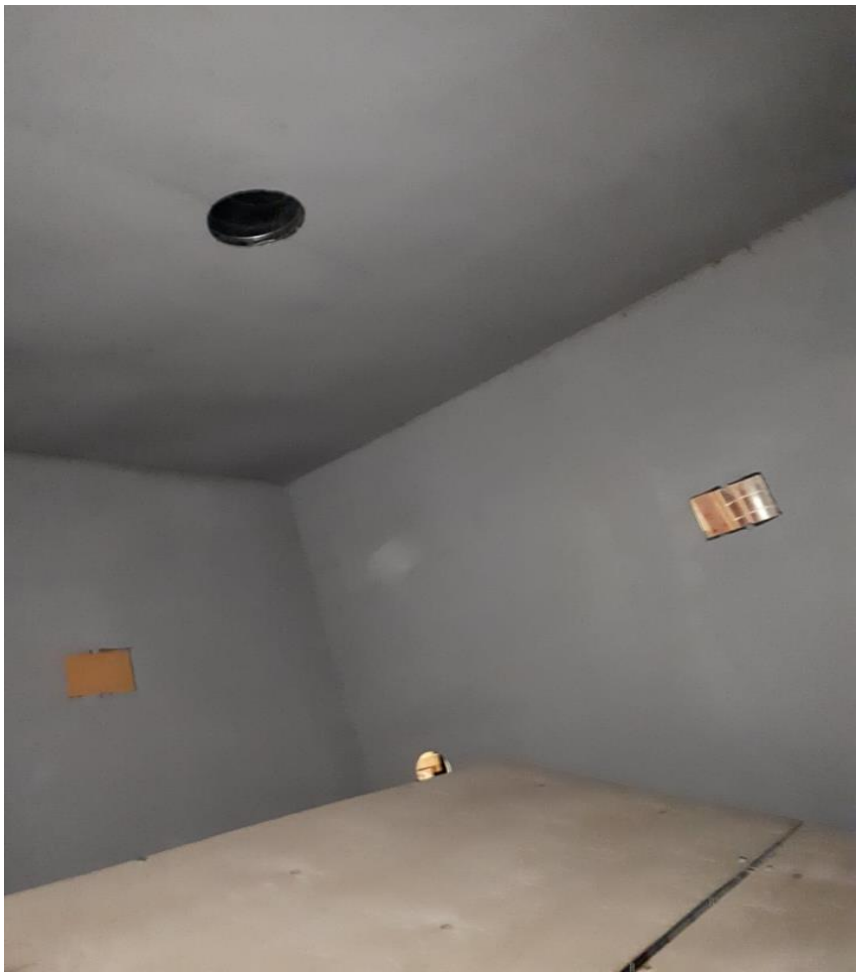

Figure 3.6 WDS outlet shown from the inside of the facility

The following six angles of incidence were conducted in this study: 0°, 30°, 45°, 180°, 210°, and 225° as shown in Figure 3.7. The applied wind speeds ranged from 14 m/s to 42 m/s with an approximate 2 m/s increment.

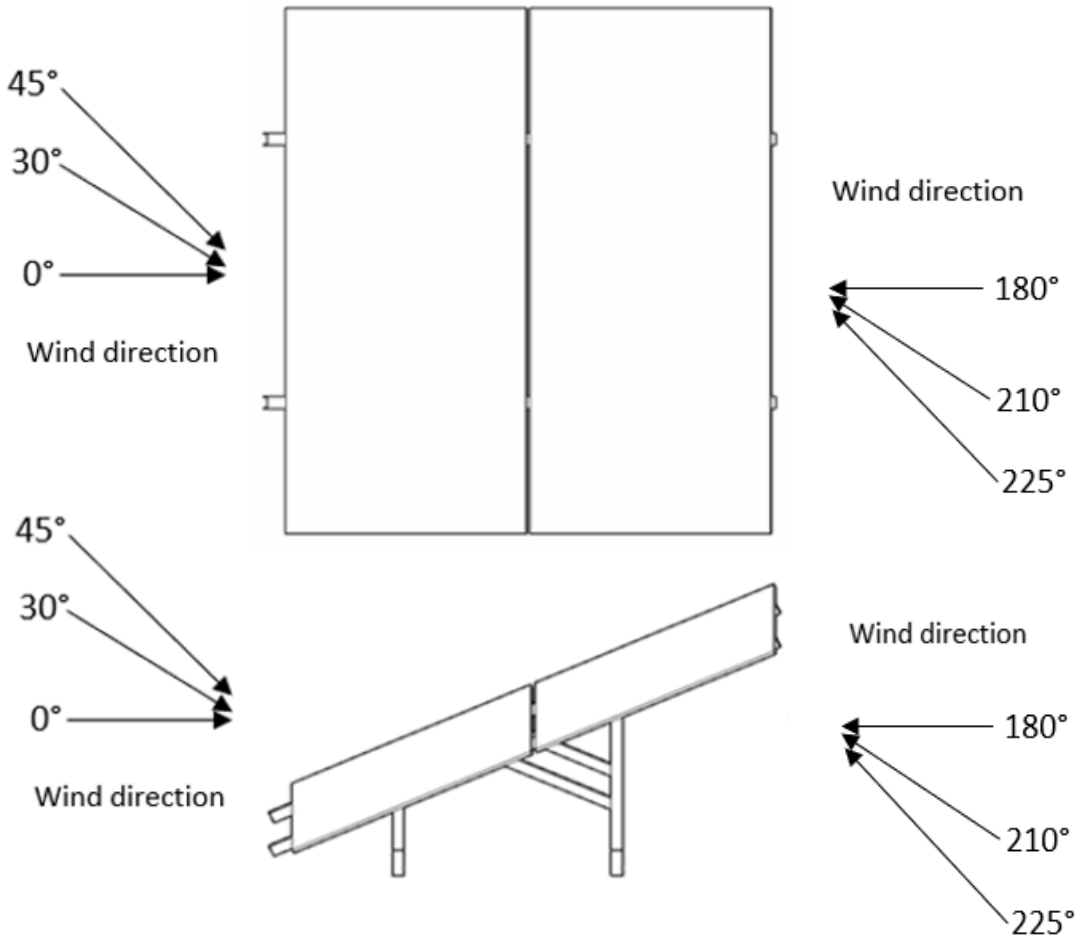

Figure 3.7 Wind angles of incidence with regards to the solar panels

DSA 3017 Scanivalve scanners were used to measure pressure. When exporting the data, each DSA 3017 Scanivalve scanner had sixteen columns of recorded pressure values that correspond to each port that represents a specific pressure tap located on the panel surfaces. In addition, the Aeroprobe sensor and the Pitot tube were connected to the scanners and were used for the inlets and plenum measurements. In total, for each of the six wind angles of incidence, about 12,600 to 14,000 readings were obtained from each scanner. A total of seven pressure scanners was required for the experiment, while each scanner allows for sixteen tubes that were connected to the panels' surfaces, to the Aero-probe or to the Pitot tube. Since the pressure inside the box is negative due to suction, the reference pressure was placed outside the box, which will allow the scanners to measure the pressure difference between the surface location and outside of the box. This increased

the accuracy of the scanners due to the fact that they operate more precisely for higher pressure difference values.

The following is the procedure adopted to conduct the experiment:

- 1) Set up the required equipment and test module
- 2) Adjust the panels' direction
- 3) Connect the scanners to the computer through the Ethernet Network Cable
- 4) Check all the scanners are turned on and computer connections are properly functioning
- 5) Lift the box and place it carefully over the panels using the crane (shown in Figure 3.8)
- 6) Open the required inlets for the case, and launch the Scanivalve software
- 7) Apply the quick zero calibration (CALZ) setting to all the scanners prior to starting the experiment (as recommended by Scanivalve Corp.)
- 8) Set the required unit (Pa), average (25) and frames per scan (1,000) in the settings
- 9) Turn on the blower and start the connection via Bluetooth
- 10) Set the required motor speed in rpm
- 11) Check that the velocity applied is correct through the readings, and keep running the rpm for 10 minutes before starting to record the data to allow the flow to settle
- 12) Record about 900-1,000 frames
- 13) Save the files in their corresponding folders
- 14) For the next wind speed, repeat steps 10) to 13)
- 15) For the next wind AOI, repeat steps 2) to 14)

Figure 3.8 Box lifted over the panels by the crane (45° AOI case)

It is important to emphasize on the “quick zero calibration” (step 7), which makes the small necessary corrections to ensure the accuracy of the sensor. Inlet 1 and inlet 2 were used for the 0°, 30°, and 45° angles of incidence (AOI), whereas inlet 3 and inlet 4 were used for the 180°, 210° and 225°, where the inlets numbering is shown in Figure 3.9. The six angles of incidence were chosen to minimize the crane usage as much as possible, to help reduce air leakage due to re-sealing of the edges and perimeter of the box. For example, for the 0° wind angle of incidence case, inlet 1 and inlet 2 are open and the rest of the inlets are closed; and by simply closing inlet 1 and 2 and opening inlet 3 and inlet 4, the wind direction conditions for the 180° wind angle of incidence case were created. Similarly, the same reasoning was followed for the 30° and 210° cases, along with the 45° and 225° cases.

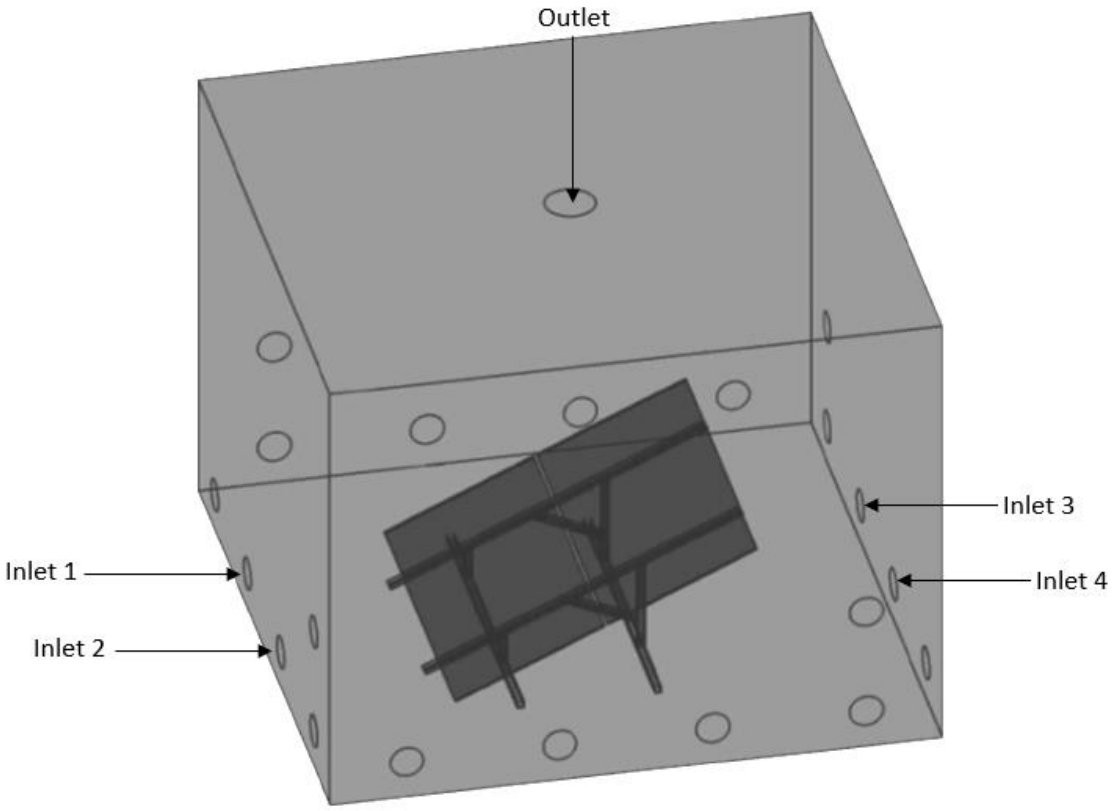

Figure 3.9 Schematic of the WDS with panels

To measure the average pressure coefficient distribution on the panels, 48 pressure taps were located and drilled on each panel surface, as shown in Figure 3.10. The readings were then obtained by connecting Vinyl pressure tubes of a diameter of 2 mm from each drilled location to the DSA3017 Scanivalve scanners which themselves were connected to the computer. For each wind angle of incidence (AOI), about 900-1,000 values were recorded over the duration of each wind speed (5 minutes). The values were then extracted and analyzed in order to determine the average pressure coefficient value.

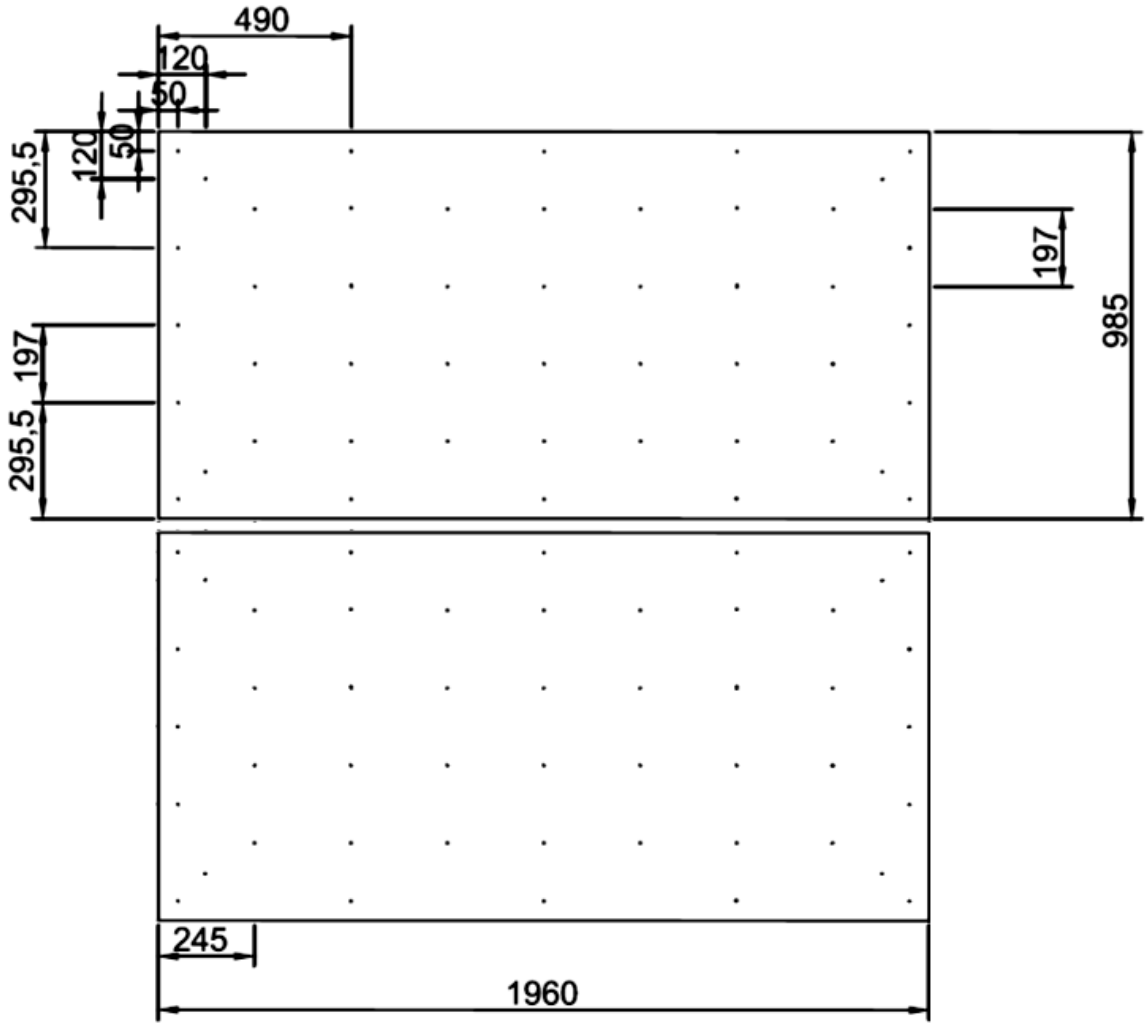

Figure 3.10 Pressure taps distribution on panels surfaces (dimensions in mm)

Different procedures may result in different wind-induced pressure coefficients Cp. In order to determine the wind-induced pressure coefficient Cp (Eq. 2.5), the reference pressure and the dynamic pressure (Eq. 2.2) must be accurately determined. The velocity of the inlet was considered as the reference velocity used in the pressure coefficient calculations. Pitot tube and the Aero-probe sensor were used to obtain measurements at the inlets for each case throughout the experiment. This allowed to make sure that the stream static pressure is identical to the plenum pressure, along with determining the right velocity magnitude through the pressure difference method, as proposed by Müllenbach and Deutenbach (1991).

Equation (3.1) can be used to determine the surface time history pressure coefficient, Cp(t), which was then averaged in order to obtain the mean pressure coefficient values for each considered case.

$$C_p(t) = \frac{P(t) - P_0(t)}{q(t)} \tag{3.1}$$

The reference velocity was considered at the inlet of the WDS facility. It should be noted that the velocity approaching the panel is slightly smaller because it decreases slightly with the distance from the inlet; however, since it can be affected by the presence of the panel (blockage effects), this will unintentionally lead to errors in the dynamic pressure, hence it cannot be used in the calculations. For the consistency with the other investigated cases (30°, 45°, 180°,210° and 225°) and for results comparison purposes, the inlet velocity is used as the reference velocity in the Cp calculation.

Chapter 4 Experimental Results

4.1 Introduction

In the current chapter, the results obtained from the measurements during the experiments are presented and organized according to the wind angle of incidence (AOI). Six different wind AOI were considered: 0°, 30°, 45°, 180°, 210°, and 225° (Figure 3.7) along with fourteen wind speeds ranging from 14 m/s to 42 m/s, in increments of around 2 m/s. In total, 84 test cases were conducted and recorded. The time-averaged pressure coefficients were determined for the upper surface and the lower surface of the tested panels, as per the pressure taps distribution shown in Figure 3.10, which were used to determine the net pressure coefficient, Cp_{net}. To understand the variation of wind pressure coefficients at representative locations on the panels, graphs representing the pressure coefficients along three lines were determined and plotted for the upper and lower surfaces of the panels. The lines deemed critical were considered as follows: the panels' mid-line crossing the middle of the panels' surfaces, the panels' line along the direction of the inlet (inlet-line), and the panels' line along the edge (edge-line), as schematically represented in Figure 4.1. The 0° and 180° wind AOI cases were used to determine the figures for the lines; the contours representing the pressure coefficient distribution along the test model were determined and discussed for all the six wind angles of incidence (ranging from 0° to 225°). The results were normalized to the unit width of the panels for comparison reasons and were plotted for the mid-line, inlet-line and edge-line of the panels. It is important to note that the first panel ends at b/B = 0.495, followed by the 20mm gap, and the second panel, which starts at b/B = 0.51 and ends at b/B = 1.0, where B is the total width along the panel's axis of both panels combined (1,990 mm) and b is the distance where the particular reading was obtained, as shown in Figure 4.1 below.

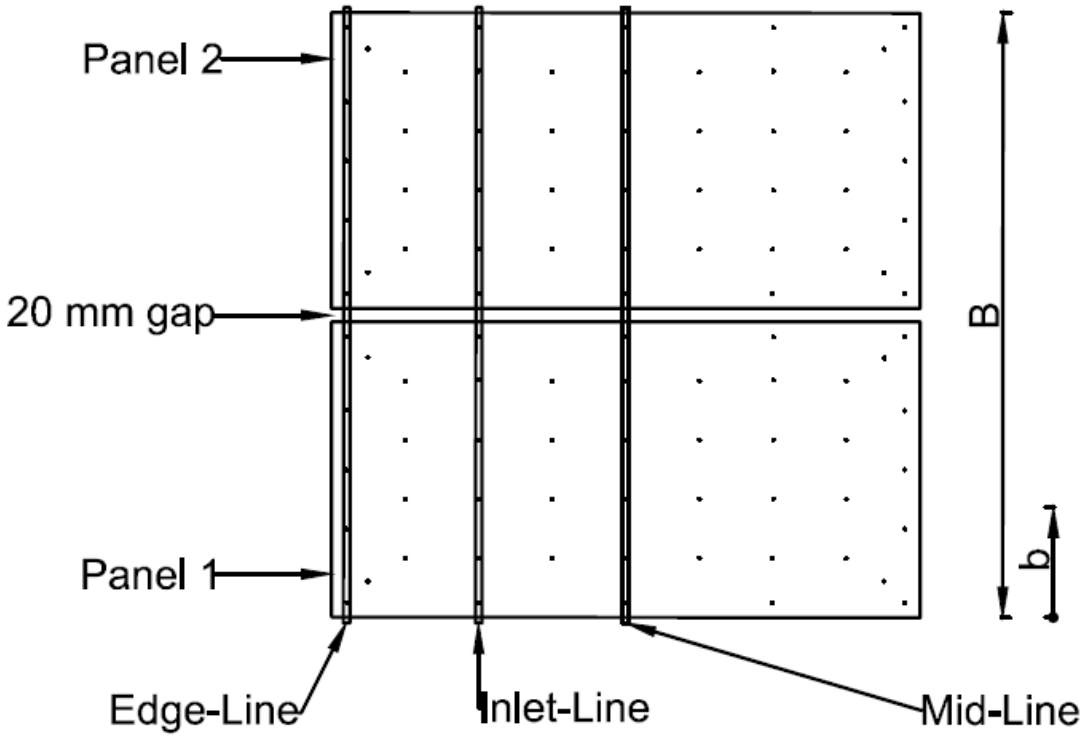

Figure 4.1 Model configuration of the panels with pressure taps showing different lines and the corresponding locations

4.2 Wind-induced pressure coefficients for the 0° angle of incidence

The pressure coefficient for the solar panels subjected to incoming wind flow at 0°AOI (Figure 4.2) were obtained for several wind speeds, ranging from 14.76 m/s to 41.40 m/s. The pressure was measured for the upper and lower surfaces of the solar panels, and the results were grouped into three wind speeds rages, for which similarities could be noticed in the C_p distribution:

Range 1: 14.76 m/s to 22.79 m/s

Range 2: 24.77 to 31.13 m/s

Range 3: 33.15 to 41.40 m/s

As mentioned previously, the values of the mean pressure coefficient of the upper and lower surfaces of the panels were obtained, and the mean net pressure coefficient was determined by subtracting the lower from the upper mean pressure coefficient (Eq. 2.6) for each AOI case. A

positive pressure coefficient signifies that the wind is directed towards the corresponding surface, while a negative pressure coefficient signifies that the wind is directed away from that surface.

Figure 4.2 Inside view of the WDS with panels inside (0° wind angle of incidence)

4.2.1 Pressure coefficients along the mid-line of the solar panels for 0° AOI

The pressure coefficients along the mid-line of the panels are determined for the upper surfaces and lower surfaces of the panels, and based on these measurements, the net pressure coefficients are obtained. Results are presented and discussed below.

4.2.1.1 Cp along panels' upper surface mid-line

The pressure coefficients registered along the mid-line of the panels' upper surface, for range 1 wind speeds, are represented in Figure 4.3. It was noticed that the pressure coefficients on the upper surface of the first panel decreased gradually along the mid-line, reaching negative Cp values (suction) at b/B = 0.4. An abrupt increase of Cp followed when approaching the 20mm gap

between the two panels (at b/B = 0.47), which could be caused by the separation and flow impinging on the edge of the first panel or the outlet effect located at the middle of the WDS. Along the mid-line of the upper surface of the second panel, the pressure coefficients decreased gradually until it experienced suction at halfway of the mid-line (b/B = 0.7). Afterwards the pressure coefficients increased to their maximum positive value followed by a decreasing trend until suction is reached when approaching the edge of the second panel (Figure 4.3). This Cp alternation signifies the possibility of swirls formation as the wind flow hits the panels' surfaces.

The upper surface pressure coefficients along the mid-line for wind speeds range 2 and range 3 are represented in Figure 4.4 and Figure 4.5, respectively. It was noticed that for most of the high wind speeds the pressure coefficient on the first panel upper surface started by positive values followed by a decrease along the mid-line until b/B = 0.2, then by an increase at ¾ of the mid-line. Instead of a sudden increase when approaching the gap between the two panels, the pressure coefficient decreased, and the suction occurred on both panels, which is different than the Cp evolution observed for the velocities in range 1 (Figure 4.3). This could be due to the stronger outlet suction for higher wind speeds forcing more wind flow to move away from the mid-line of the second panel, towards the outlet, causing a negative pressure near the gap. Moreover, wind passing below the panel could have been redirected upward through the 20mm gap between the panels. It can be noticed that for the high wind speeds (range 3, Figure 4.5), the upper surface mid-line registered positive pressure coefficients along the first panel, except for the region approaching the gap, while for the second panel the suction (negative pressure coefficients) dominated the mid-line.

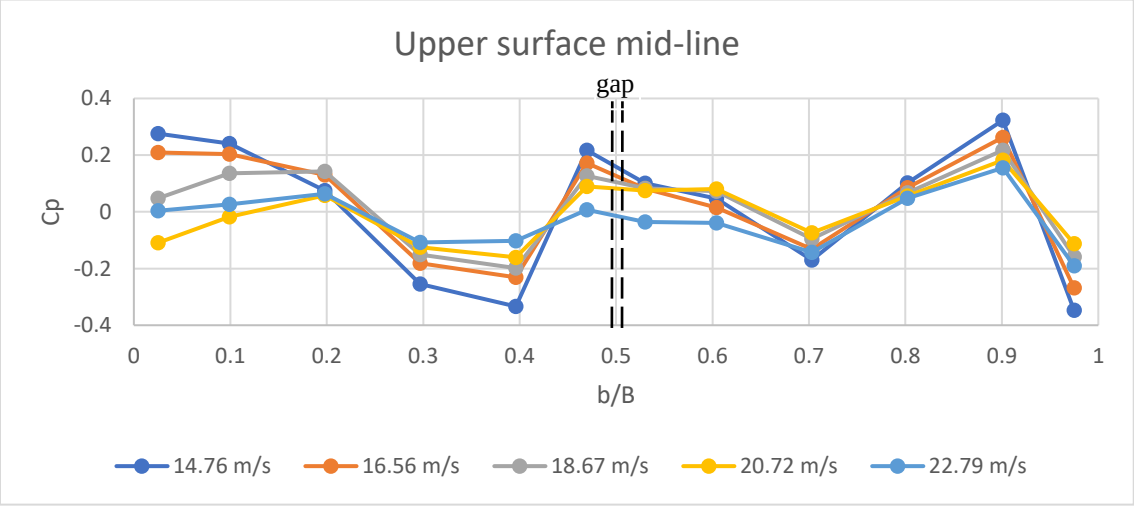

Figure 4.3 Cp variation along the upper surface mid-line (wind speed range 1, 0° AOI)

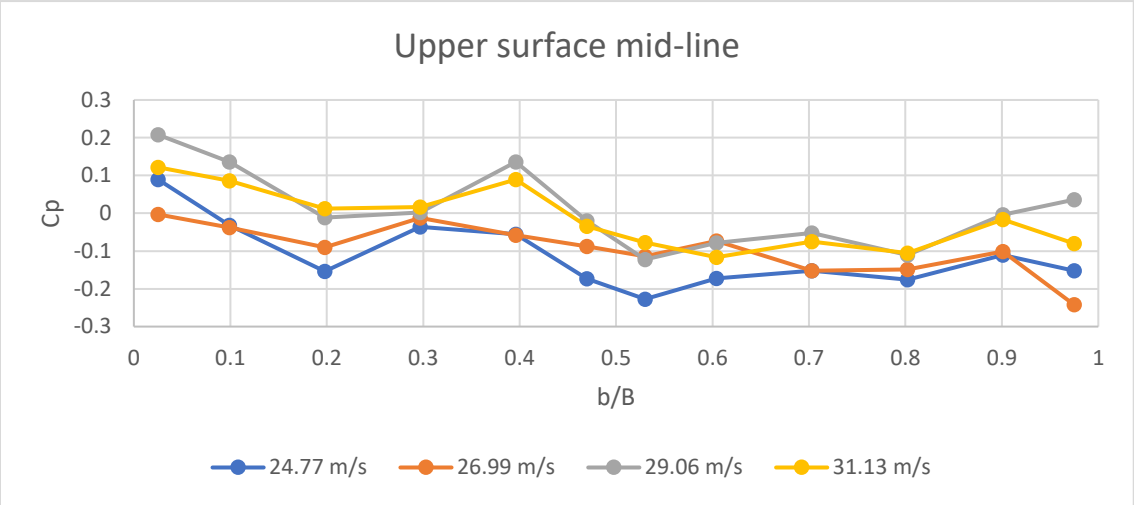

Figure 4.4 Cp variation along the upper surface mid-line (wind speed range 2, 0° AOI)

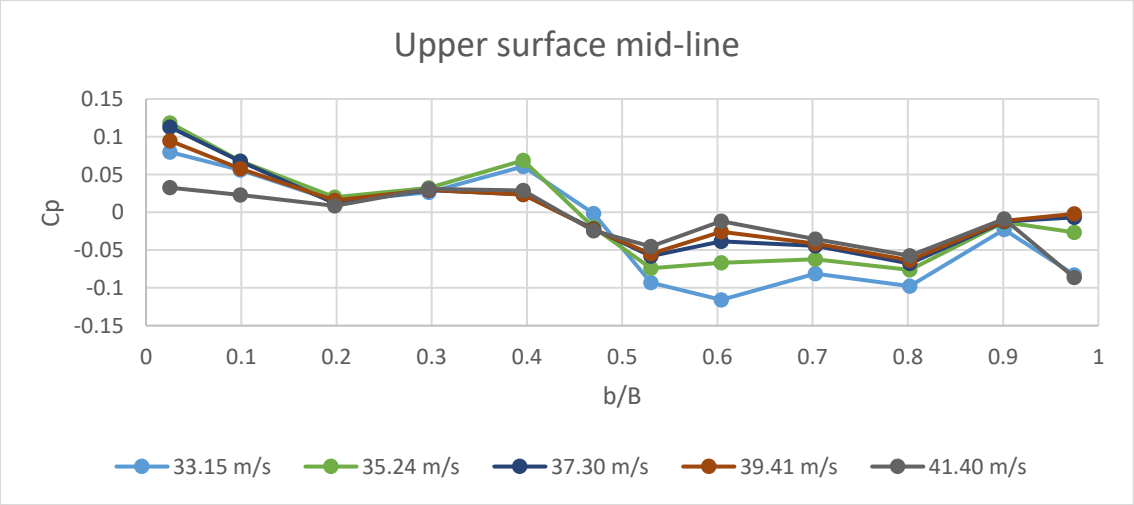

Figure 4.5 Cp variation along the upper surface mid-line (wind speed range 3, 0° AOI)

4.2.1.2 Cp along panels' lower surface mid-line

The pressure coefficients along the mid-line situated on the lower surfaces of the panels are analyzed for wind speed ranges 1 , 2, and 3, and are plotted in Figure 4.6, Figure 4.7, and Figure 4.8, respectively. The Cp distribution along the mid-line showed more similarities for the lower surface for different wind speeds, when compared with the Cp on the upper surface mid-line. It

was noticed that, for most wind speeds, the pressure coefficients on the first panel were negative at the beginning of the panel and they increased and became positive when they reached halfway of the mid-line, only to decrease again at b/B = 0.4. When the mid-line approached the gap between the panels (at b/B = 0.47), the Cp increased, meaning that the wind flow was directed upwards through the gap, since this was measured on the lower surface mid-line. Along the second panel near the gap, the Cp along the mid-line started by a negative value followed by a small increase until reaching b/B = 0.7, after which it started decreasing, ending to a negative Cp value near the leeward edge of the second panel, due to the flow detachment. For wind speeds of range 1 (Figure 4.6) and range 3 (Figure 4.8), it can be observed that the highest suction (negative Cp) along the lower surface mid-line occurred at the end of the second panel, whereas for most of range 2 wind speeds, the highest suction took place at the beginning of the first panel (Figure 4.7).

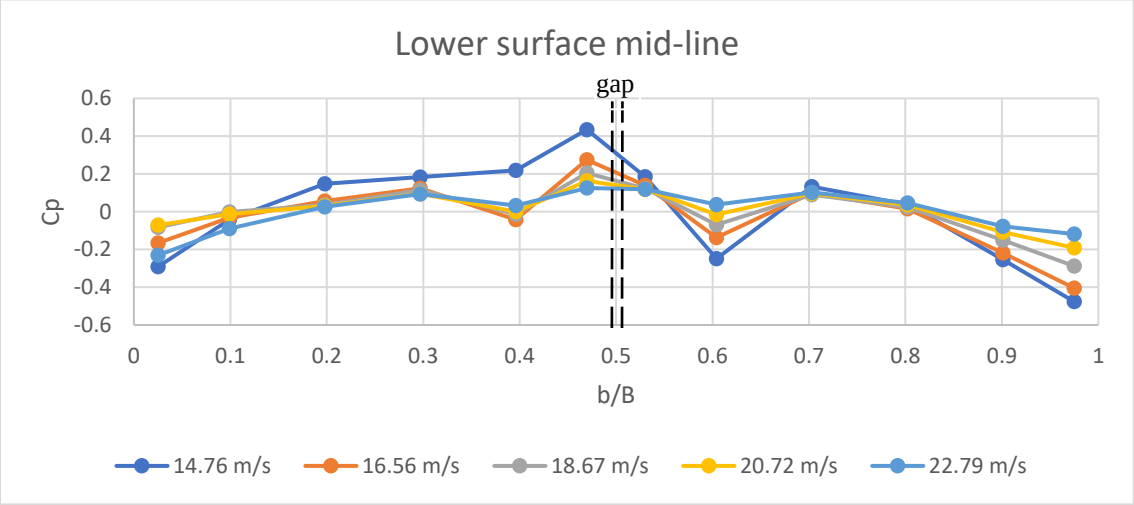

Figure 4.6 Cp variation along the lower surface mid-line (wind speed range 1, 0° AOI)

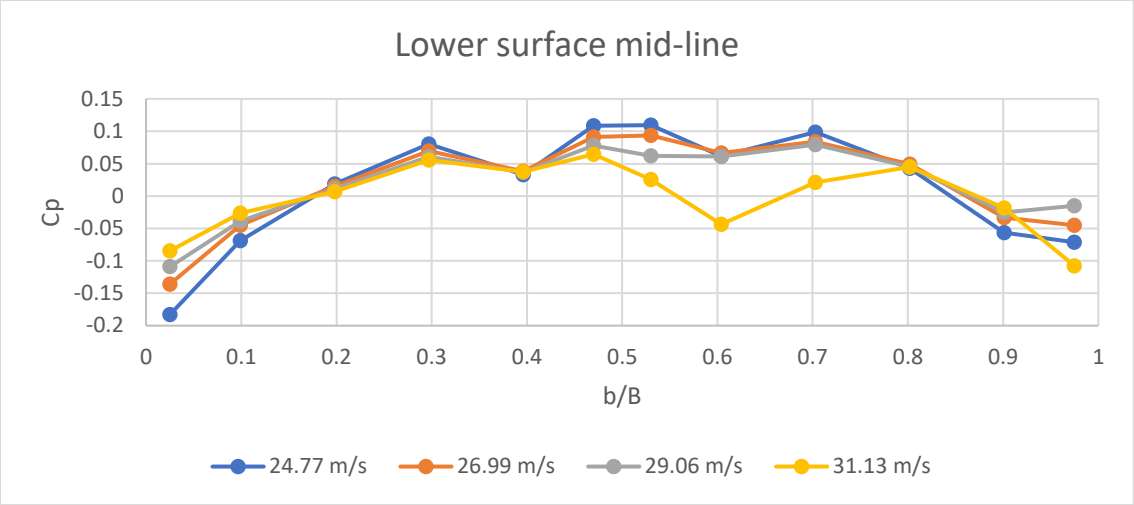

Figure 4.7 Cp variation along the lower surface mid-line (wind speed range 2, 0° AOI)

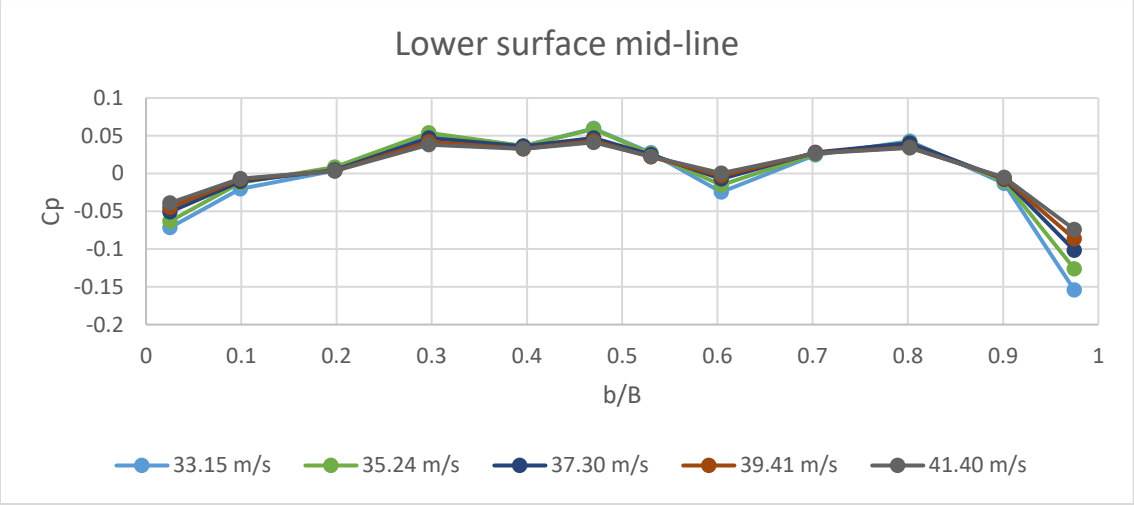

Figure 4.8 Cp variation along the lower surface mid-line (wind speed range 3, 0° AOI)

4.2.1.3 Cp_{net} along panels' mid-line

The pressure coefficients acting on both, upper and lower surfaces of the panels, were summed algebraically for determining the overall (net) pressure coefficient for the respective panels. The net pressure coefficient along the mid-line, presented in Figure 4.9, Figure 4.10 and Figure 4.11, were obtained by subtracting the lower surface pressure coefficients from the upper pressure coefficients for each wind speed. The first panel underwent positive net pressure coefficients (Cp_{net}) at the windward edge, followed by a decrease of pressure coefficients until it reached uplift at halfway of the mid-line. Along the second panel, Cp_{net} increased to positive values at b/B = 0.6

for speeds below 22.79 m/s, whereas the Cp_{net} remained in the negative range for the higher speeds, from 22.79 m/s to 41.40 m/s. It can be concluded that for speeds in range 1 (Figure 4.9), the first panel underwent a positive increasing Cp_{net}, thus diminishing the uplift when approaching the top edge, near the 20mm gap at b/B = 0.47, whereas for the speed ranges 2 and 3 (Figure 4.10 and Figure 4.11, respectively), a significant decrease in pressure (stronger suction) was noticed. For wind speeds between 14.76 m/s and 26.99 m/s, the net pressure coefficient along the mid-line decreased on the second panel when approaching the edge; Cp_{net} remained positive for 14.76 m/s to 20.72 m/s, and underwent suction for 22.79 m/s to 26.99 m/s. However, for the wind speeds ranging from 29.06 m/s to 41.40 m/s, the second panel was subjected to a significant increase of net pressure coefficient, reaching a positive Cp_{net} at the leeward edge. Along the mid-line, the 20mm gap did not have significant effects on the net pressure coefficients at the end of the first panel and beginning of the second panel.

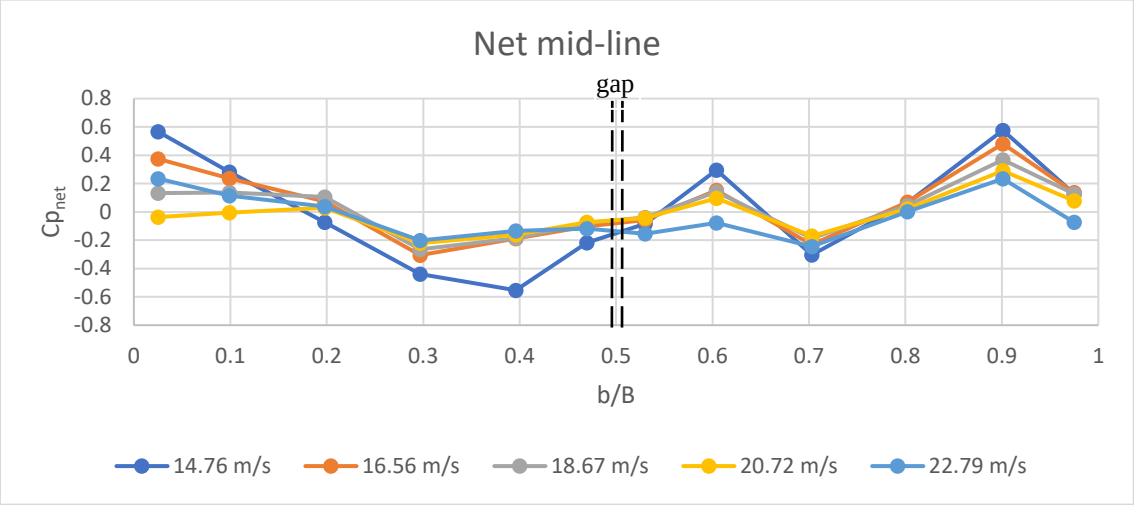

Figure 4.9 Net Cp variation along the mid-line (wind speed range 1, 0° AOI)

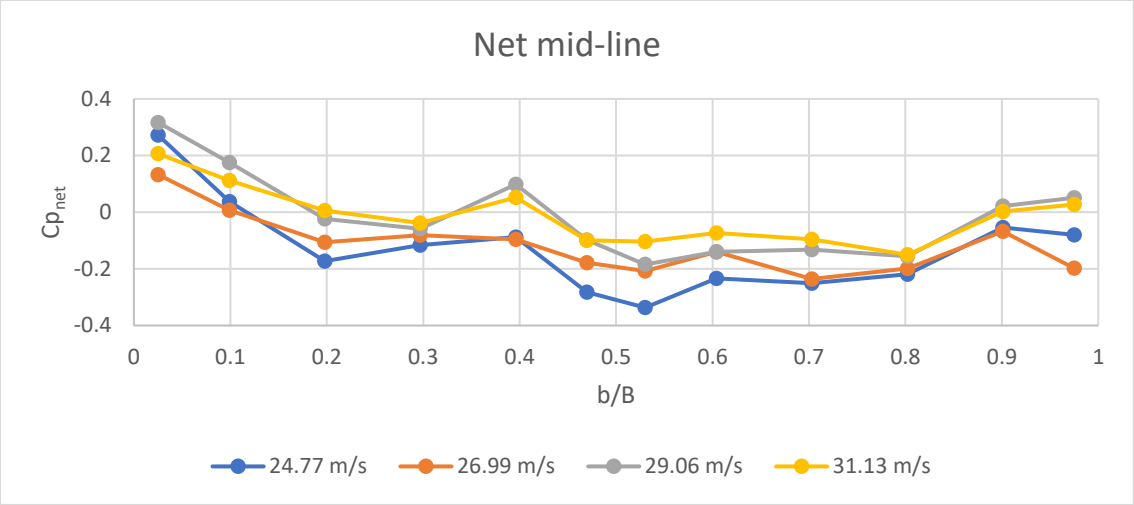

Figure 4.10 Net Cp variation along the mid-line (wind speed range 2, 0° AOI)

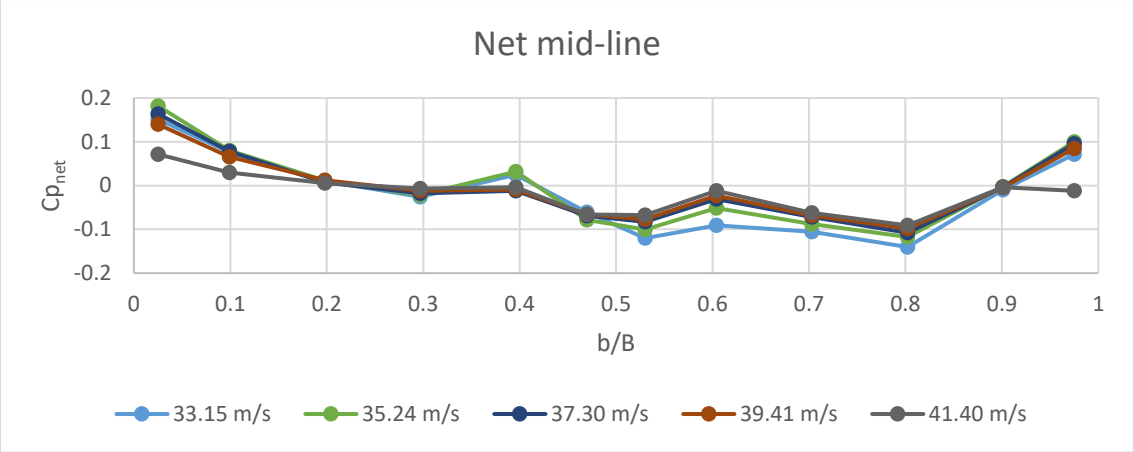

Figure 4.11 Net Cp variation along the mid-line (wind speed range 3, 0° AOI)

4.2.2 Pressure coefficients along the inlet-line of the solar panels for 0° AOI

The pressure coefficients along the line facing the inlet are determined and presented below for different wind speeds. It is important to note that even if both inlets were active for the 0° wind AOI, the Cp data only for one of the inlet-line data is reported due to symmetry.

4.2.2.1 Cp along panels' upper surface inlet-line

The upper surface pressure coefficients registered along the inlet-line for wind speeds range 1, 2 and 3 are represented in Figure 4.12, Figure 4.13 and Figure 4.14, respectively. It was noticed for

the first panel that for most of the low speeds (range 1, Figure 4.12), the pressure coefficient was positive at the point of contact, decreased to negative at b/B = 0.1, and followed an increasing trend until reaching b/B = 0.3 (597 mm along the inlet-line), then this started decreasing. Whereas for the higher wind speeds, Cp ceased to increase at b/B = 0.2 (398 mm), as shown in Figure 4.12. For the wind speeds in the ranges 2 and 3, the upper surface inlet-line of the two panels was mostly subjected to uplift, with its maximum magnitude occurring at b/B = 0.4 (796 mm along the line). For the range 1 wind speeds, the first panel reached its maximum positive pressure coefficient value at b/B = 0.3, only to follow a decreasing trend, with negative Cp (suction) until around 200 mm from the edge of the second panel, where it increased to a positive Cp then decreased towards the leeward edge. The 20mm gap had a similar effect on the Cp behavior for all the wind speeds where the inlet-line of the first panel near the gap, had an increase of Cp and a decrease after the gap on the second panel. For speed ranges 2 and 3, it can be observed that along the inlet-line of the panels' upper surfaces, pressure coefficients were dominated by suction (negative pressure), when compared with speeds of range 1, where the first panel experienced mostly positive pressure until approaching the gap; this could be attributed to the suction capacity of the WDS outlet being stronger for higher wind speeds selected.

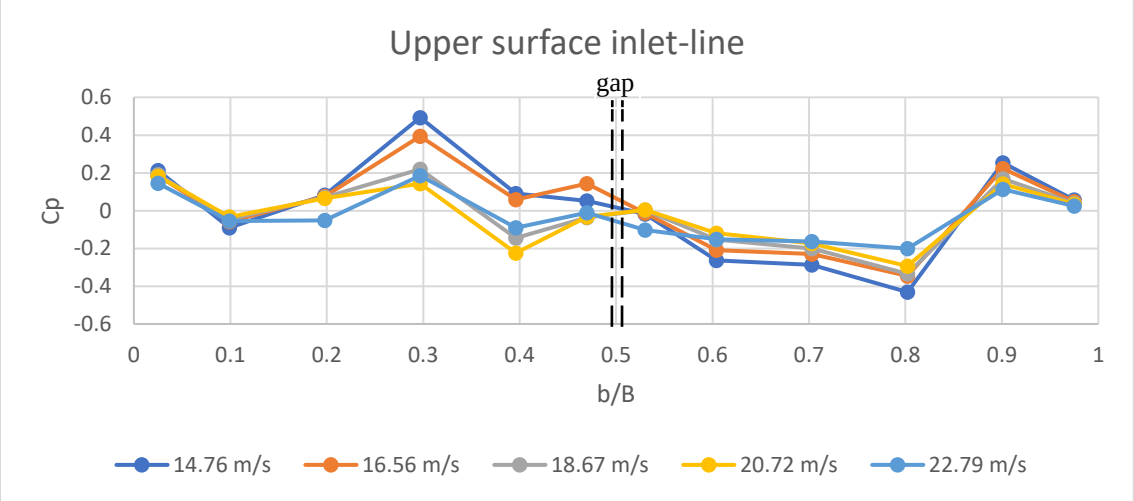

Figure 4.12 Cp variation along the upper surface inlet-line (wind speed range 1, 0° AOI)

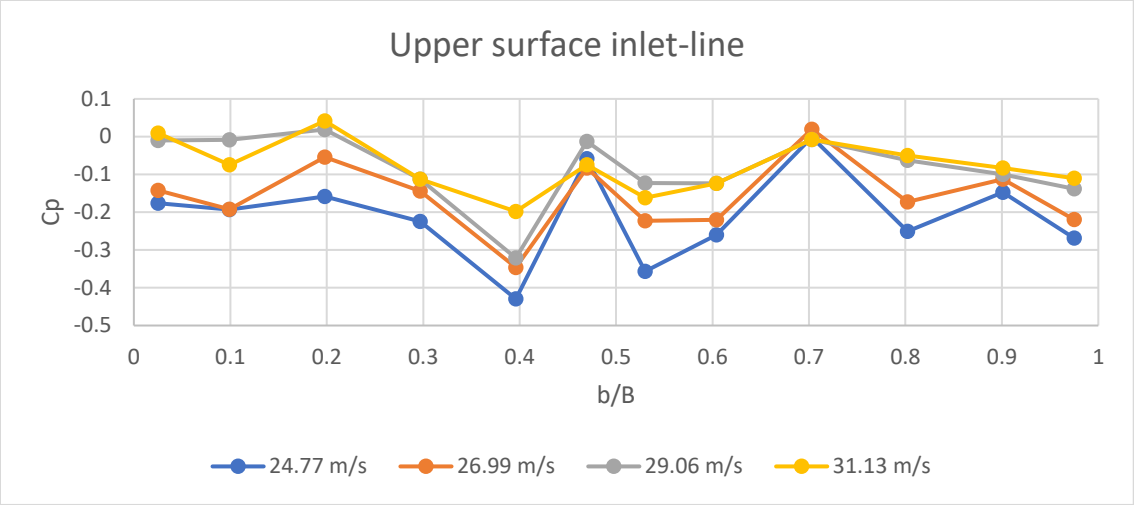

Figure 4.13 Cp variation along the upper surface inlet-line (wind speed range 2, 0° AOI)

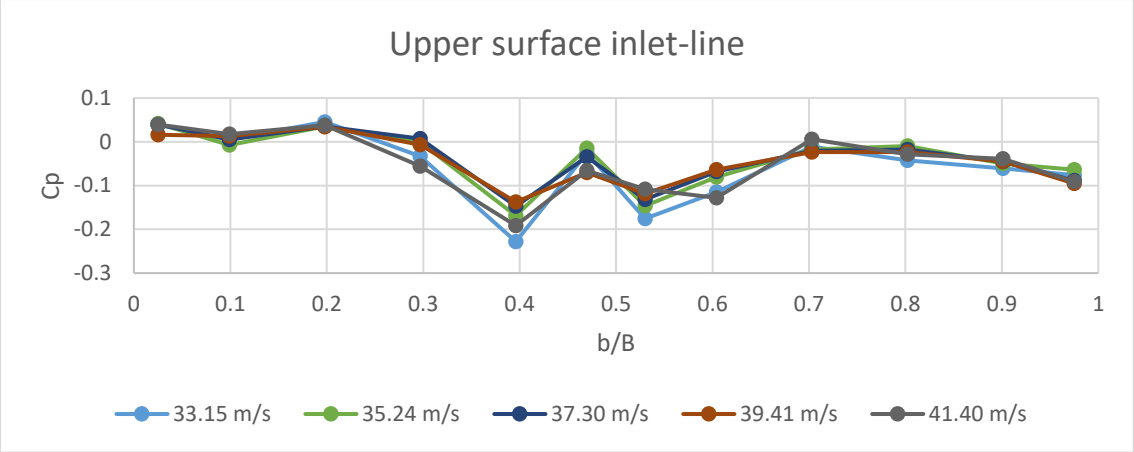

Figure 4.14 Cp variation along the upper surface inlet-line (wind speed range 3, 0° AOI)

4.2.2.2 Cp along panels' lower surface inlet-line

The pressure coefficients for the inlet-line situated on the lower surface are shown in Figure 4.15, Figure 4.16 and Figure 4.17, where a good agreement was noticed between most of speed ranges. The Cp started at negative values on the lower surface inlet-line only for the first range of speeds (14.76 m/s to 22.79 m/s), whereas for the other wind speed ranges it was positive. Cp started increasing until reaching the maximum positive value at b/B = 0.3 (597 mm along the inlet-line) on the first panel, for the wind speed ranges 1 and 2 (Figure 4.15, Figure 4.16), except for the 14.76 m/s wind speed where, similarly to the range 3 wind speeds (Figure 4.17), the maximum positive Cp values were attained prior to the edge of the second panel (at b/B = 0.9). When approaching

the 20mm gap, the Cp on the first panel decreased and for the second panel Cp followed a decreasing then increasing trend, except for the wind speeds 29.06 m/s to 41.41 m/s, where Cp increased then decreased. The inlet-line Cp along the lower surface of the second panel was negative up to halfway of the panel, thereafter it followed an increase to positive trend, and decreased when approaching the leeward edge (b/B = 0.97) for all the wind speeds. Along the lower surface inlet-line, for all the speed ranges, the first panel underwent mostly positive pressure until approaching the 20mm gap where it started decreasing to negative values.

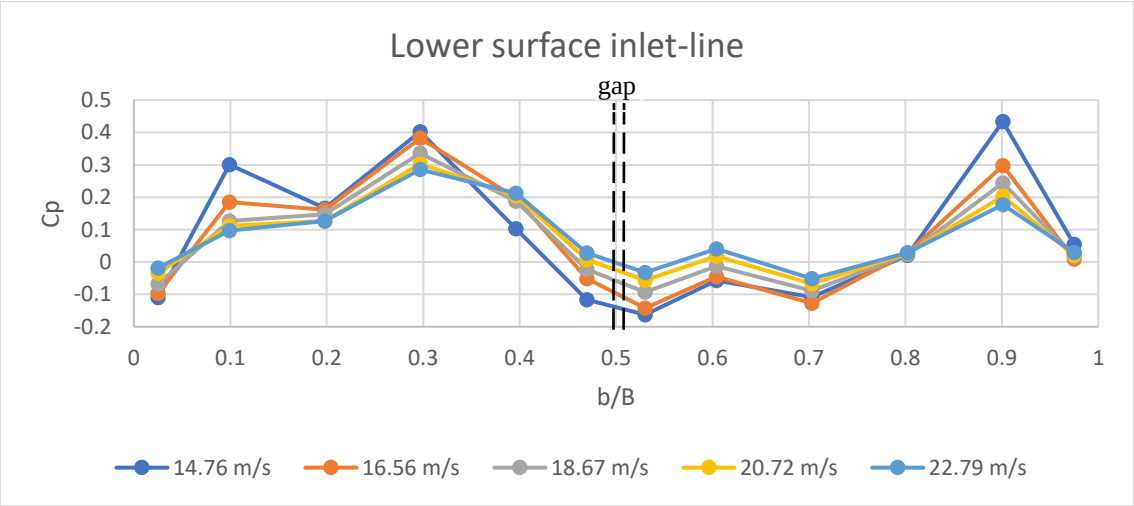

Figure 4.15 Cp variation along the lower surface inlet-line (wind speed range 1, 0° AOI)

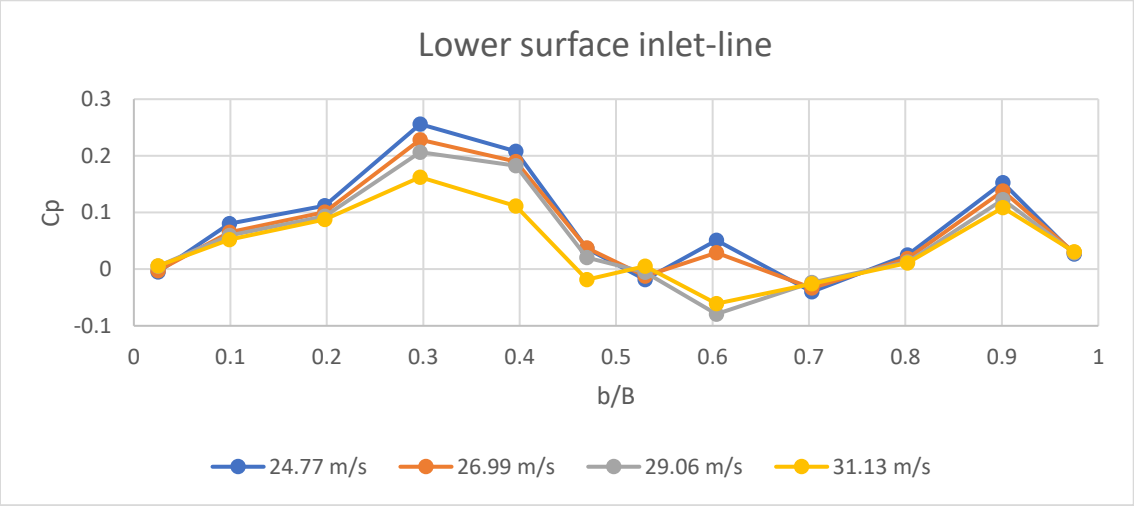

Figure 4.16 Cp variation along the lower surface inlet-line (wind speed range 2, 0° AOI)

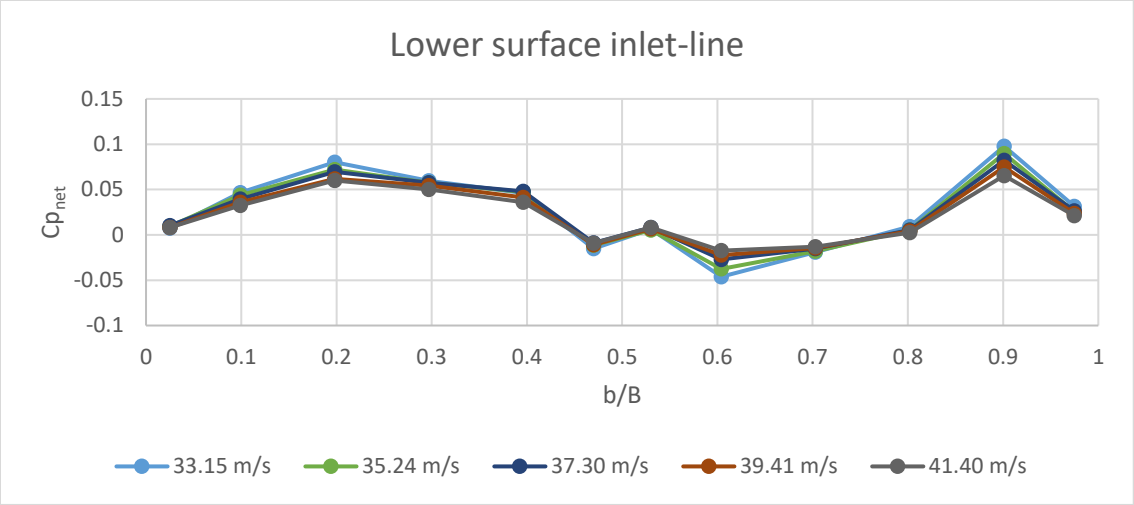

Figure 4.17 Cp variation along the lower surface inlet-line (wind speed range 3, 0° AOI)

4.2.2.3 Cp_{net} along panels' inlet-line

The net pressure coefficients along the inlet-line are represented in Figure 4.18, Figure 4.19 and Figure 4.20 for the speed ranges 1, 2, and 3, respectively. Through interpreting the results, it can be concluded that most of the first panel was subjected to suction (negative Cp_{net}) for the wind speeds of range 2, whereas for most of the other wind speeds, Cp_{net} began with positive values, followed by a decreasing trend and remaining in the negative region. Only for the lowest two speeds (14.76 m/s and 16.56 m/s) an increase to positive Cp_{net} values was observed on the first panel when approaching the gap between the panels. The highest uplift was observed at b/B = 0.4 (796 mm along the first panel), for all the wind speeds except for wind speeds below 18.67 m/s, where it occurred at halfway of the second panel, at b/B = 0.8 (Figure 4.18). It can be concluded that the second panel was subjected mostly to negative pressure, except when speed ranges from 14.76 m/s to 20.72 m/s; the Cp_{net} registered positive values immediately after the gap, on the second panel (b/B = 0.53) and then this decreased to negative values. However, at b/B = 0.7 (halfway of the second panel inlet-line), the Cp_{net} increased to positive or near zero, then immediately decreased furthermore, for the wind speed ranges 2 and 3. The largest suction Cp_{net} value occurred on the second panel at b/B = 0.8 for wind speeds below 18.67 m/s (Figure 4.18), and for the other wind speeds, the highest uplift Cp_{net} value occurred on the first panel (at b/B value of 0.4) before approaching the 20mm gap (b/B = 0.47). For most of the wind speeds, the 20mm gap between the panels affected the net pressure coefficients values, where the magnitude

of suction decreased on the end of the first panel. A CFD study was performed for better understanding the Cp fluctuations and the wind behavior around the two solar panels, and the results were presented in Chapter 5.

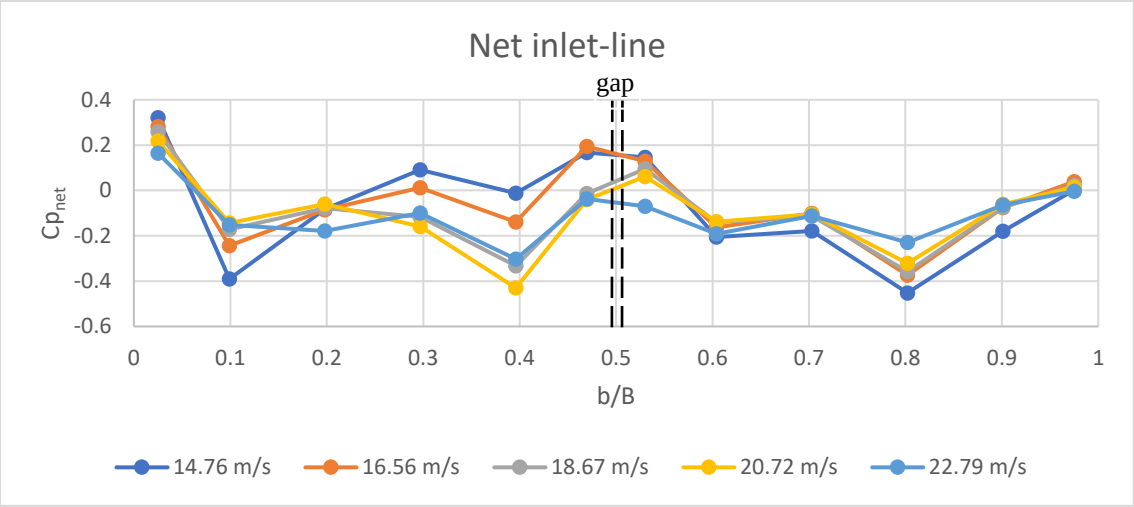

Figure 4.18 Net Cp variation along the inlet-line (wind speed range 1, 0° AOI)

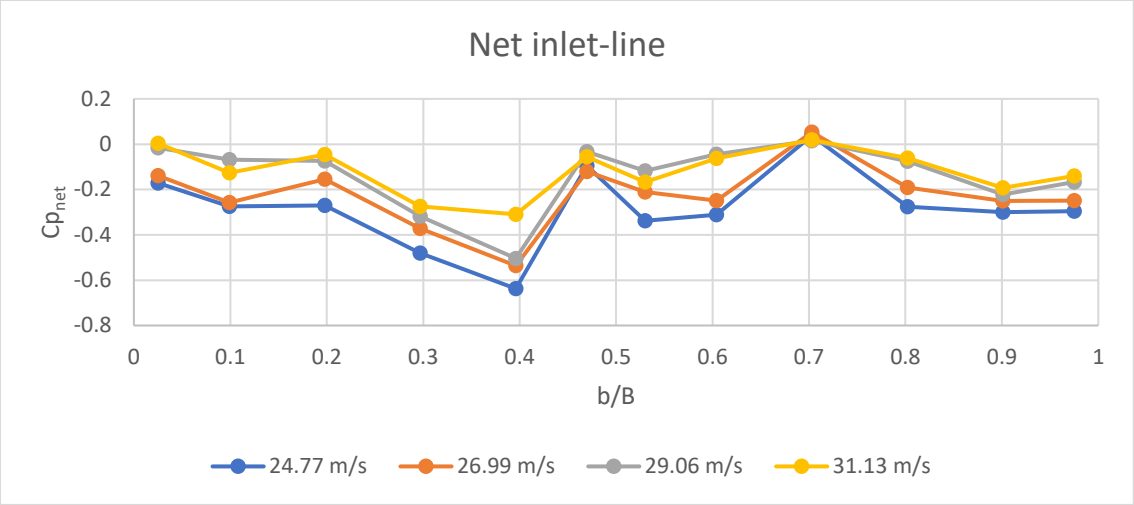

Figure 4.19 Net Cp variation along the inlet-line (wind speed range 2, 0° AOI)

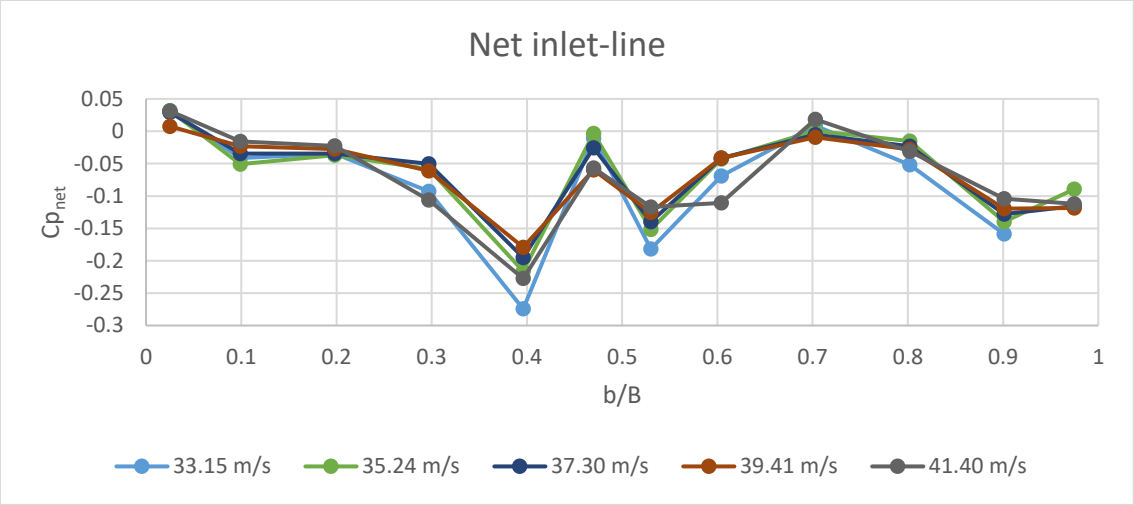

Figure 4.20 Net Cp variation along the inlet-line (wind speed range 3, 0° AOI)

4.2.3 Pressure coefficients along the edge-line of the solar panels for 0° AOI

Along the edge-line of the tested panels, the pressure coefficients are determined for all the wind speeds and are presented below.

4.2.3.1 Cp along panels' upper surface edge-line

In Figure 4.21, Figure 4.22 and Figure 4.23, the pressure coefficients along the upper surface edge-line are plotted for the wind speed ranges 1, 2, and 3 respectively. Similar trends for the pressure coefficients were noticed for the speed ranges 2 and 3 (24.77 m/s to 41.41 m/s), where the Cp started with a negative value along the first panel, following a decreasing trend then increasing at halfway of the panel until it reached a positive value or near 0 on the second panel, after the 20mm gap (at b/B = 0.53), as it can be observed in Figure 4.22, and Figure 4.23. After the gap, the Cp distribution on the second panel registered uplift (negative values) along the entire edge-line and decreased when approaching the leeward edge of the second panel. The edge-line of the first panel was subjected to the highest suction Cp value, around halfway of the line, for the wind speed ranges 2 and 3. For the wind speeds of range 1 (Figure 4.21), the Cp distribution started with a positive value for the first panel, followed by a decrease then an increase, reaching constant positive values at b/B = 0.25 and 0.35. When approaching the gap (b/B = 0.47), Cp decreased to the highest suction value occurring along the upper edge of the first panel, then increased along

the beginning of the second panel, until it reached a positive value at b/B = 0.65 (289 mm along the second panel). Afterwards, Cp values decreased to negative at b/B = 0.85, until it reached the edge of the second panel, where the Cp value increased and became positive.

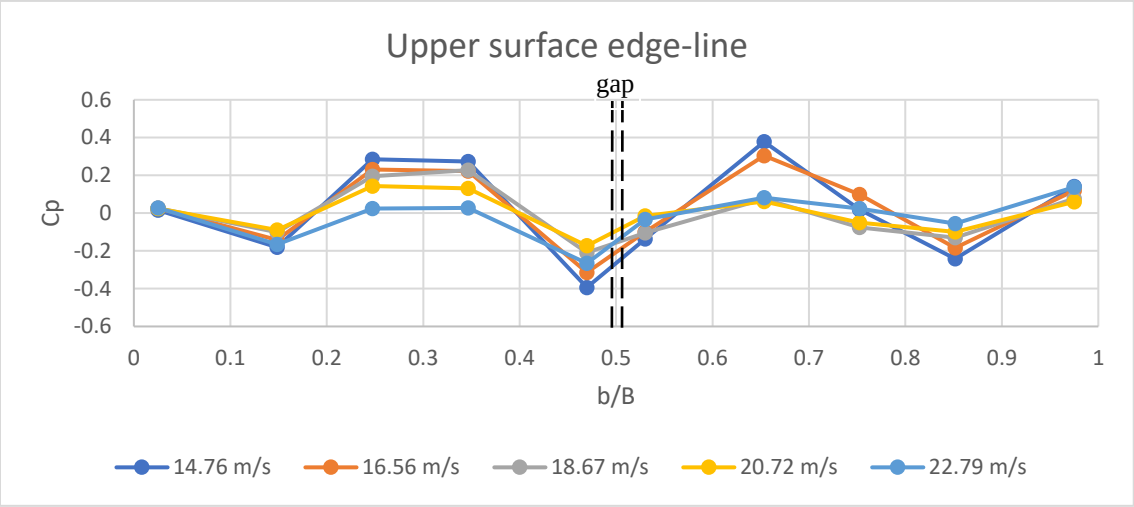

Figure 4.21 Cp variation along the upper surface edge-line (wind speed range 1, 0° AOI)

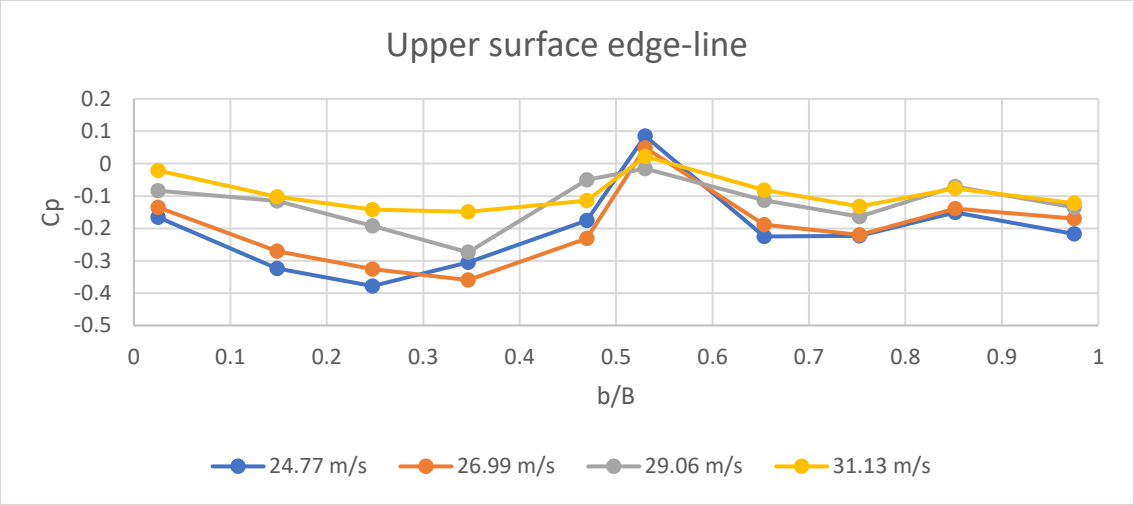

Figure 4.22 Cp variation along the upper surface edge-line (wind speed range 2, 0° AOI)

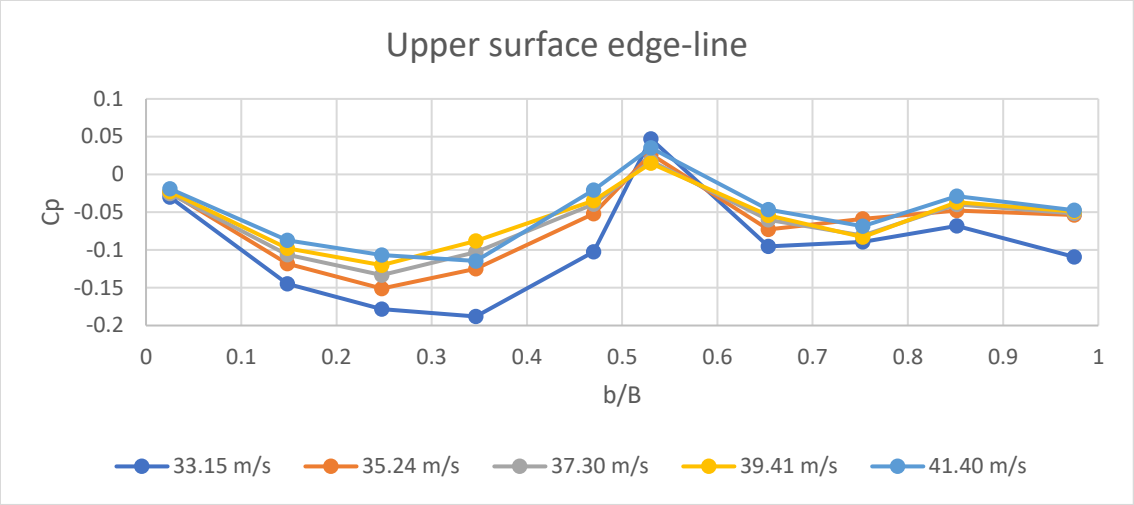

Figure 4.23 Cp variation along the upper surface edge-line (wind speed range 3, 0° AOI)

4.2.3.2 Cp along panels' lower surface edge-line

The pressure coefficients along the edge-line lower surface are represented in Figure 4.24, Figure 4.25 and Figure 4.26 for the wind speed ranges 1, 2, and 3, respectively. The Cp registered positive values for all the speed ranges along the bottom edge of the first panel, followed by a decreasing trend, then increased at halfway of the first panel lower surface (at b/B = 0.25). The Cp stayed in the positive range for most of the cases, except for wind velocities below 20.72 m/s. At b/B = 0.35, it decreased until reaching a negative value for most of the investigated cases. In the vicinity of the gap, around b/B = 0.5, the Cp values increased slightly on the first panel and decreased on the second panel. The lower surface of the second panel was subjected mostly to positive pressure coefficients along the edge-line where it evolved to negative values at b/B 0.85, then it increased near the top edge of the panel. The highest Cp magnitude along the edge-line was positive, and occurred on the lower edge of the first panel for wind speeds of range 2 (Figure 4.25), and around halfway of the second panel for wind speeds of ranges 1 and 3 (Figure 4.24 and Figure 4.26, respectively).

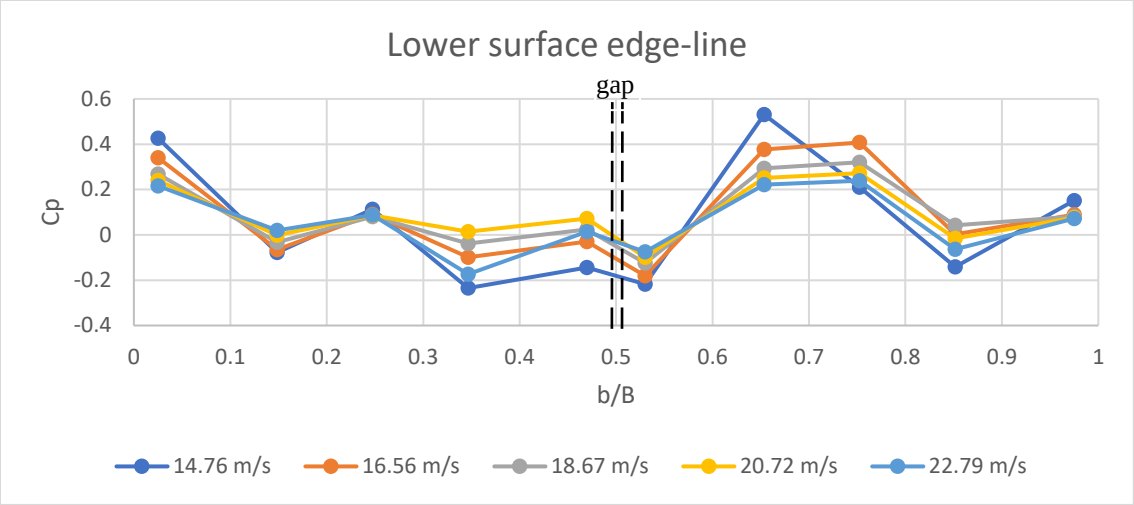

Figure 4.24 Cp variation along the lower surface edge-line (wind speed range 1, 0° AOI)

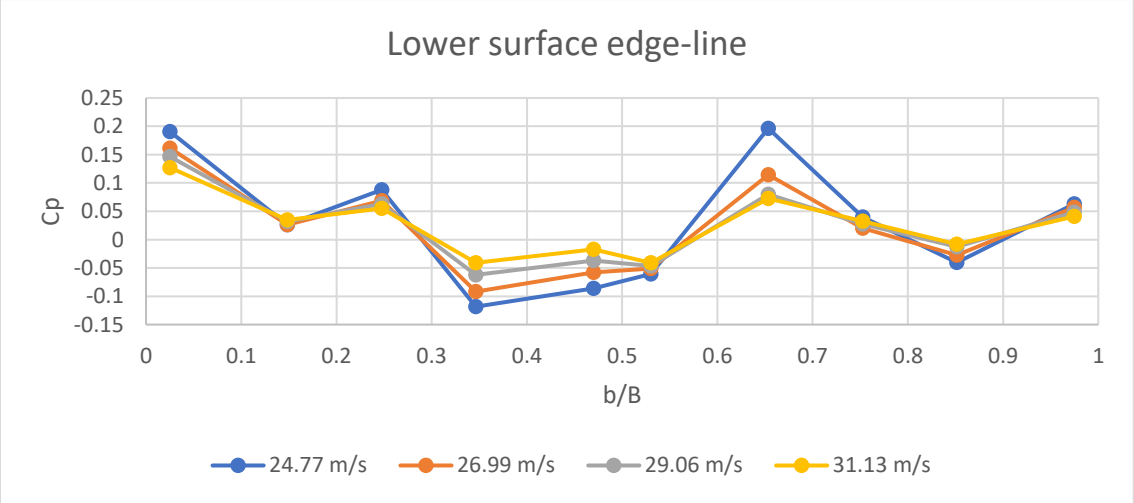

Figure 4.25 Cp variation along the lower surface edge-line (wind speed range 2, 0° AOI)

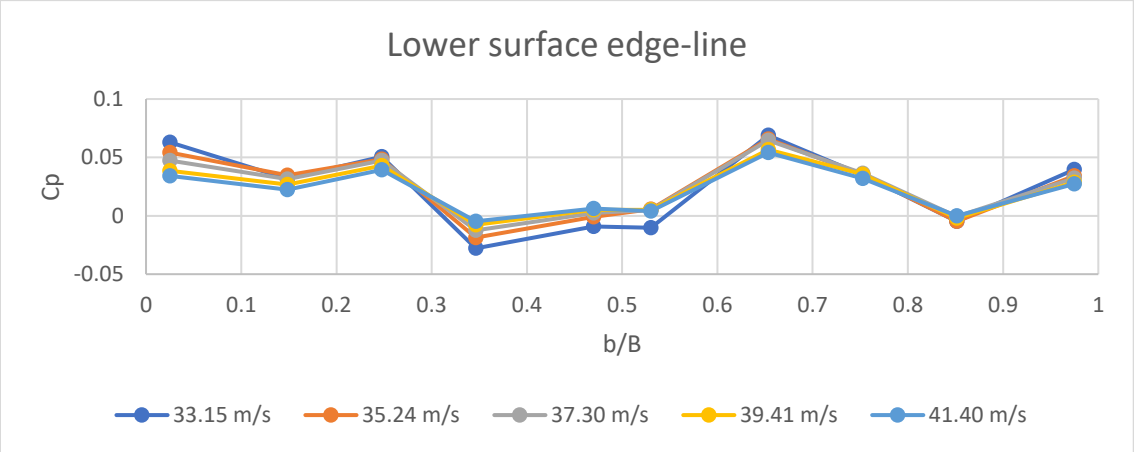

Figure 4.26 Cp variation along the lower surface edge-line (wind speed range 3, 0° AOI)

4.2.3.3 Cp_{net} along panels' edge-line

For the three wind speed ranges examined, the net pressure coefficients along the edge-line are plotted in Figure 4.27, Figure 4.28, and Figure 4.29. For all the tested wind speeds, the net pressure coefficients started with negative values (suction) for the first panel and increased to positive values after the gap (b/B = 0.53). For the wind speed ranges 2 and 3 (24.77 m/s to 41.40 m/s), Cp_{net} had similar behavior. The edge-line along both panels was subjected to negative pressure (uplift), except for the second panel near the 20mm gap (at b/B= 0.53) where the Cp_{net} increased to positive values, afterwards it decreased to negative values (Figure 4.28, Figure 4.29). For the range 1 wind speeds, along the edge-line of the first panel, the Cp_{net} increased to the highest positive values at b/B = 0.35, followed by a decrease up to negative values then an increase to positive for the second panel near the 20mm gap (Figure 4.27). A difference in Cp_{net} behavior was spotted near the end of the edge-line, along the second panel, where it decreased for the wind speed ranges 2 and 3 and increased for the wind speed range 1. For the case of 0° wind AOI, the 20mm gap between the panels increased the net pressure coefficients, along the edge-line of the second panel and this could be attributed to the wind flow passing through the gap downwards due to wind impinging on the first panel surface near its upper edge.

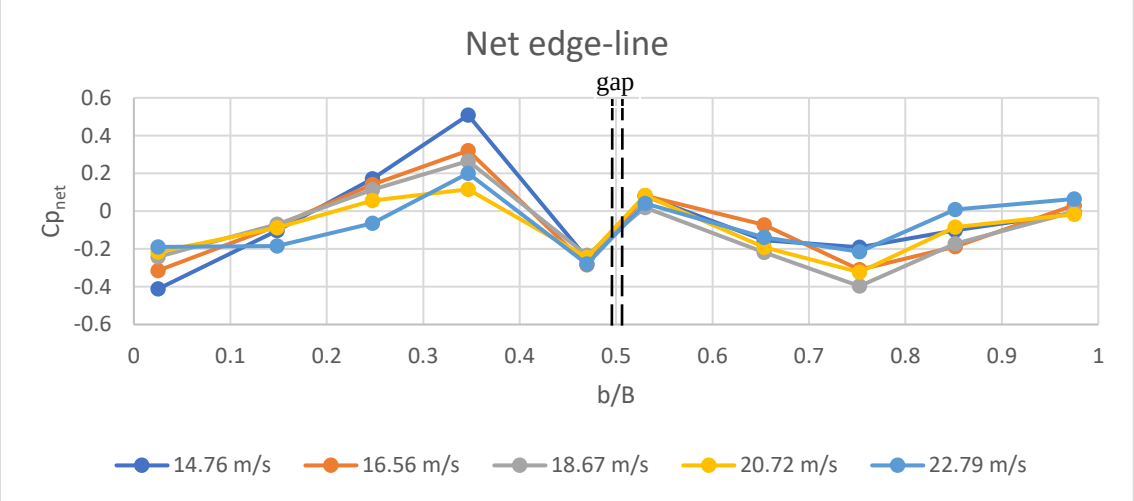

Figure 4.27 Net Cp variation along the edge-line (wind speed range 1, 0° AOI)

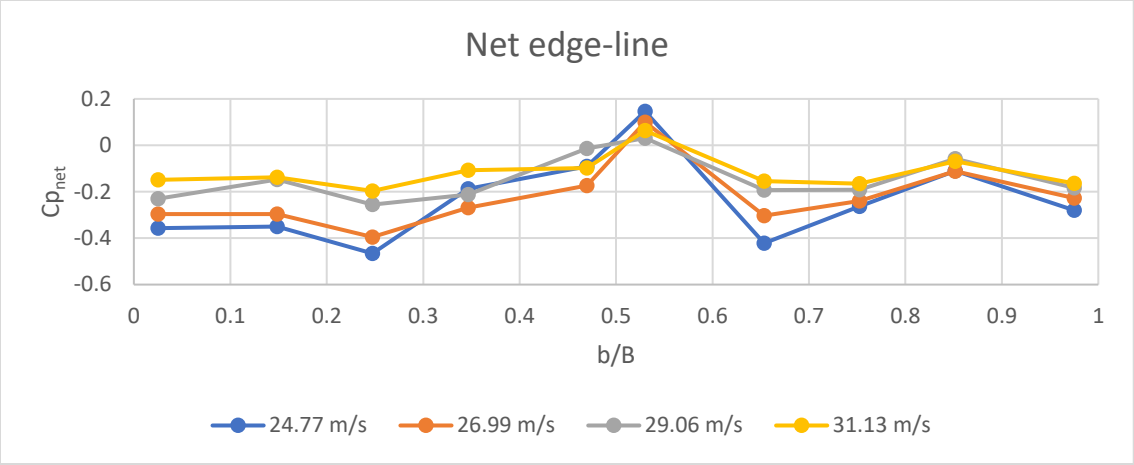

Figure 4.28 Net Cp variation along the edge-line (wind speed range 2, 0° AOI)

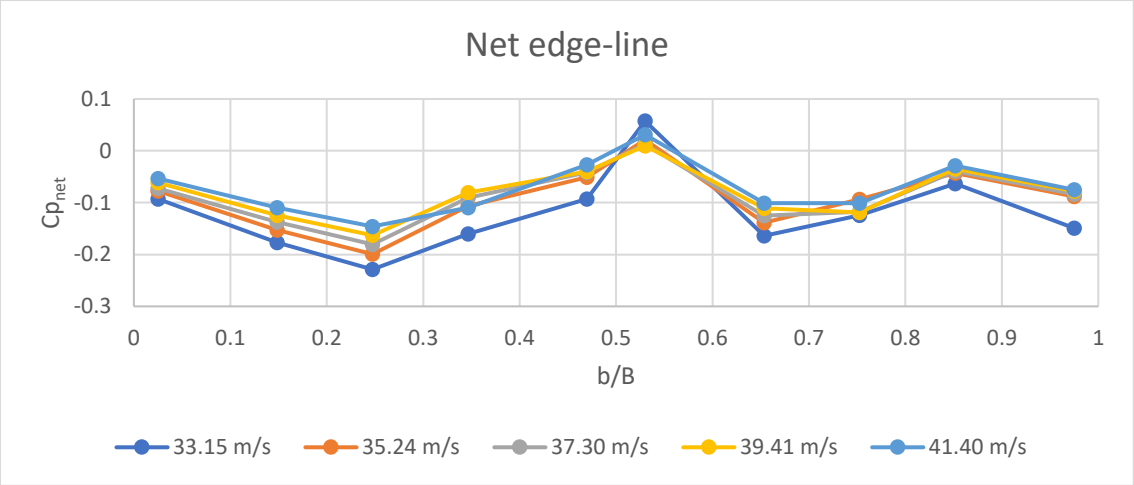

Figure 4.29 Net Cp variation along the edge-line (wind speed range 3, 0° AOI)

4.2.4 Pressure coefficients contours along the solar panels for 0° AOI

Table 4.1 represents the contours for the mean pressure coefficients on the upper and lower surfaces of the two panels, and the contours for the net pressure coefficients, determined for the panels, for the case of 0° wind AOI at a 25° inclination angle. The contours were obtained through the Cp values corresponding to the pressure taps measurements, presented in Chapter 3. The mean pressure coefficients distributions were reported for one wind speed from each of the ranges as follows: 20.72 m/s (range 1), 31.13 m/s (range 2), and 37.30 m/s (range 3). When the panel was exposed to wind at an angle of incidence of 0°, the incoming wind flow is deflected by its surface. Due to the location of the inlets, outlet suction effect, and the flow detachment and reattachment

on the surface of the panels, this created different types of pressure coefficient distributions, where Cp fluctuations were observed. A negative pressure coefficient signifies that suction is applied to the examined surface, thus the wind flow is directed away from the subjected surface, and a positive pressure coefficient values mean that the wind flow is directed towards the respective surface.

4.2.4.1 Cp along panels' upper surface for 0° AOI

The distribution of the pressure coefficients on the upper surface of the panels, obtained from the experimental results, showed that the inlet-lines of both panels were subjected mostly to negative Cp (suction) for the wind speeds 31.13 m/s and 37.30 m/s; this could be caused by the strong suction of the WDS outlet situated on the roof of the experimental room, thus having a larger effect on the wind flow redirected upwards from the panels and passing through the suction outlet. For the 20.72 m/s wind speed, where the WDS outlet suction rpm setting was lower, it can be noticed that the line along the surface facing the inlet is positive on the first panel, with its highest value occurring around the middle of the inlet-line, as it can be noticed in the contours of Table 4.1. Thereafter, a diminishing trend followed, and the Cp reached negative magnitudes (suction) along the rest of the inlet-line and on the second panel, except when approaching the upper edge of the second panel, where the pressure coefficient was positive. That could be due to flow separation near the leeward edge. Along the mid-line of the panels' upper surfaces, the pressure coefficients for the two wind speeds 31.13 m/s and 37.30 m/s were positive, reaching maximum values when it first approached the windward edge and stayed positive on the first panel, only to diminish and reach suction along the entire mid-line of the second panel's upper surface. For the smaller wind speed of 20.70 m/s, the Cp along the mid-line of the first panel was mostly negative with its highest suction attained after reaching halfway of the first panel; on the second panel the pressure coefficient was mostly positive along the entire mid-line.

It can be observed that for low wind speeds, the lines facing the inlets on the first panel and the mid-line of the second panel were subjected to positive Cp, whereas for the higher wind speeds, only the mid-line of the first panel was subjected to positive Cp. This could be attributed to the increasing suction capacity of the blower exerted at the WDS outlet, thus having higher influence

on the wind flow redirecting it upwards from the middle region of the panels and towards the outlet.

4.2.4.2 Cp along panels' lower surface for 0° AOI

The pressure coefficient distribution on the lower surface was mostly positive on both panels for the three wind speeds: 20.72 m/s, 31.13 m/s, and 37.30 m/s, shown in Table 4.1, with a maximum positive pressure coefficient occurring on the first panel, after reaching halfway of the line facing the inlet. Along the mid-line of the lower surface, it can be noticed that for the first panel the Cp started by a negative value, followed by an increasing trend until reaching a positive Cp on the lower surface, in the vicinity of the 20mm gap between the panels. This can be attributed to the wind flow passed below the panel or deflected by the walls, being re-directed upwards towards the WDS outlet through the gap.

4.2.4.3 Cp_{net} along the panels for 0° AOI

The net pressure coefficients are the combination of the Cp registered on both the upper and lower surfaces of the two panels, obtained by subtracting the lower surface pressure coefficients from the upper surface pressure coefficients. Overall, for higher wind speeds (31.13 m/s and 37.30 m/s), it can be observed that the net pressure coefficients on the first panel were mostly negative (uplift) on both panels except for the region at the beginning of the mid-line of the first panel, where this started with positive values, then it diminished with the distance and became negative along the rest of the mid-line. For 20.72 m/s, similar behavior was observed on the first panel; however, the Cp_{net} started with the positive pressure coefficients on the inlet-line and negative (suction) on the mid-line. For the second panel, the mid-line underwent positive net pressure coefficients whereas the inlet-line was mostly subjected to suction (negative Cp_{net}). Near the top edge of the second panel, positive net pressure coefficients were present, and this could be due to the impinging flow at the edge of the panel.

Table 4.1 Cp contours comparison for different wind speeds (20.72 m/s, 31.13 m/s, 37.30m/s) at 0° AOI:

Velocity	Upper Surface Cp	Lower Surface Cp	Net Cp
20.72 m/s	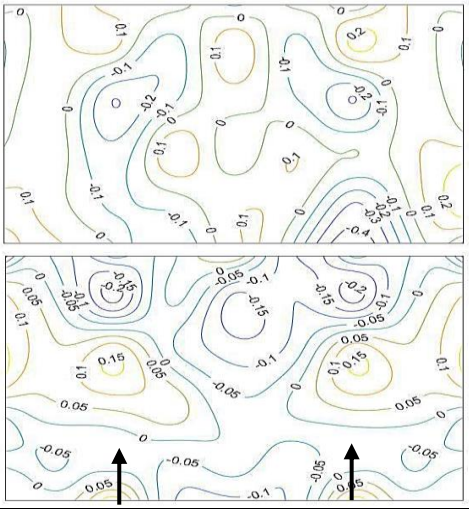	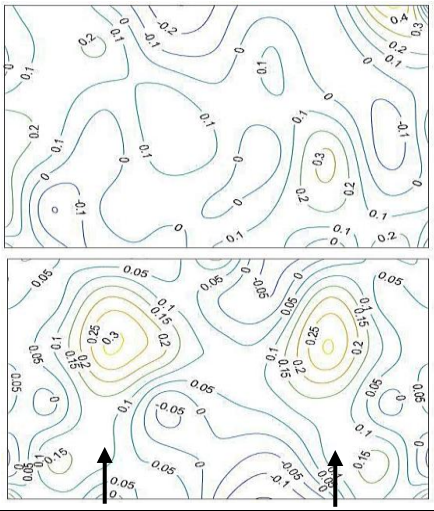	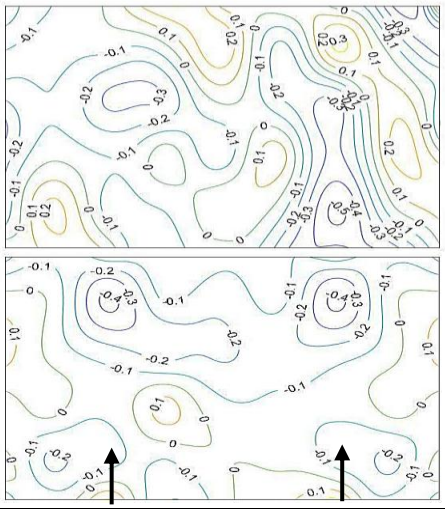
31.13 m/s	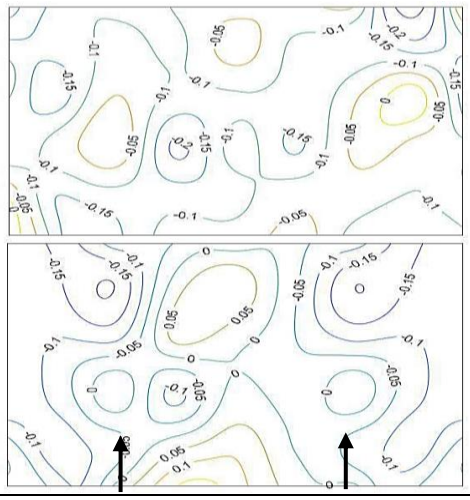	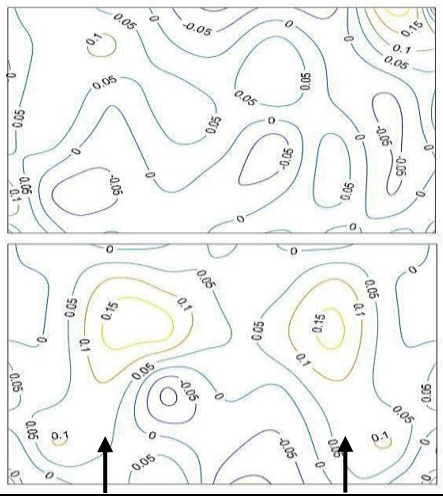	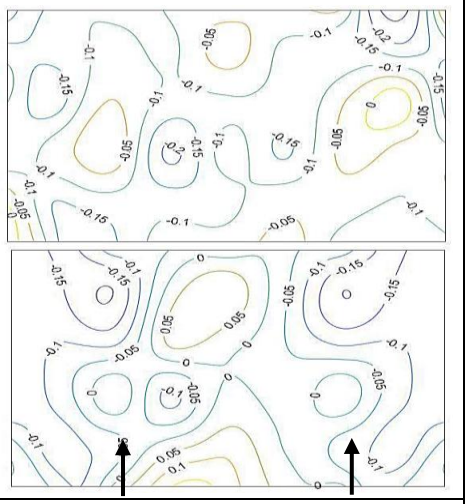
37.30 m/s	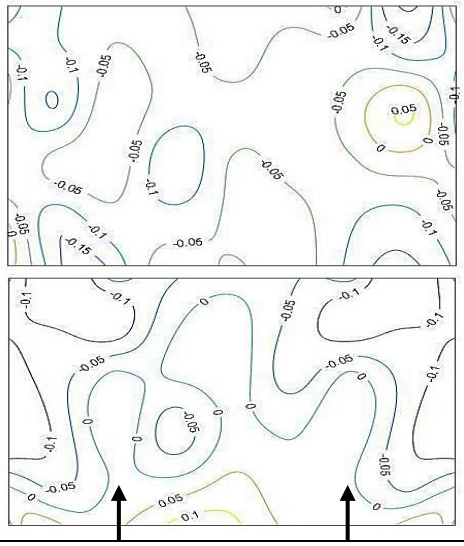	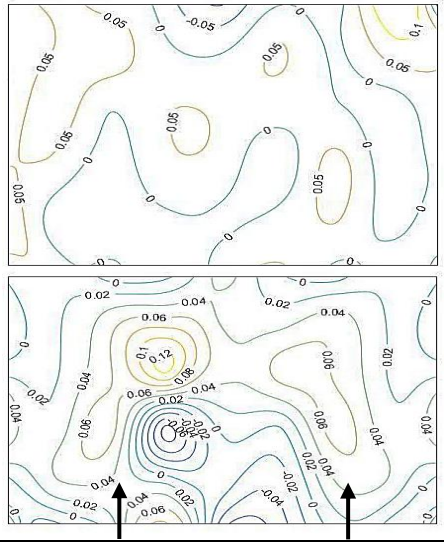	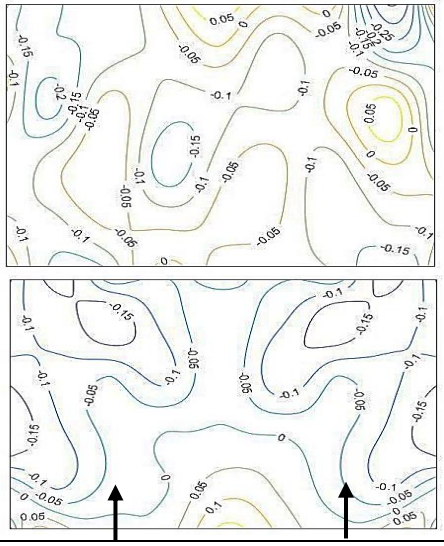

4.2.5 Comparison with previous ground-mounted solar panels study, for 0° AOI

The results of the mean pressure coefficient contours along the panels were compared with the study conducted by Samani (2016) for better understanding and evaluating the capacities of the WDS facility. The previous study (Samani, 2016) was conducted on stand-alone ground-mounted solar panels with the same dimensions (1,960 x 1,990 mm), same gap width (20mm) and same panels' inclination angle (25°), as employed in the current study. However, two main differences should be mentioned: first, the present study used the solar panels models made of plywood, whereas Samani (2016) used the panel models fabricated by polycarbonate. Second, the current study employs the WDS facility, which has inlet flows induced by the outlet suction, while Samani (2016) conducted the study at the wind tunnel called the WindEEE Dome, which replicates the boundary layer wind profile, thus the wind flows are different. The comparison was based on the present study pressure coefficient results corresponding to a velocity of 16.56 m/s, and the Samani (2016) pressure coefficient results corresponding to a velocity of 15.61 m/s.

As it can be seen for the 0° wind AOI case, for the net pressure coefficient contours along the panels, there are negative values (uplift), which is different than the results of the experiment conducted by Samani (2016), where there are only positive Cp_{net} values (Figure 4.30). For the current study, the first panel undergoes mostly negative net pressure coefficients, except for the beginning of the inlet-lines and mid-line, and some parts along the upper half of the edge-lines. This could be due to the fact that in the WDS facility, the high suction induced by the outlet controls the flow in the chamber: the outlet opening, located at the middle of the roof of the WDS, directs the air upwards, away from the panels, through its connecting duct to the blower (industrial fan). Values tend to show different magnitudes than those obtained through the experiment conducted in the WindEEE Dome facility, and this is due to the different experimental conditions used in the theses two studies. During the present experiment, the panels' projected areas are much larger than the inlet cross sectional area in the WDS facility, which is where the air is directed towards the inside of the chamber and gets dispersed towards the test model. This could be the main cause of obtaining lower Cp values, in addition to the suction induced by the blower at the top outlet causing the air to be directed upwards which can be noticed for high wind speeds cases investigated.

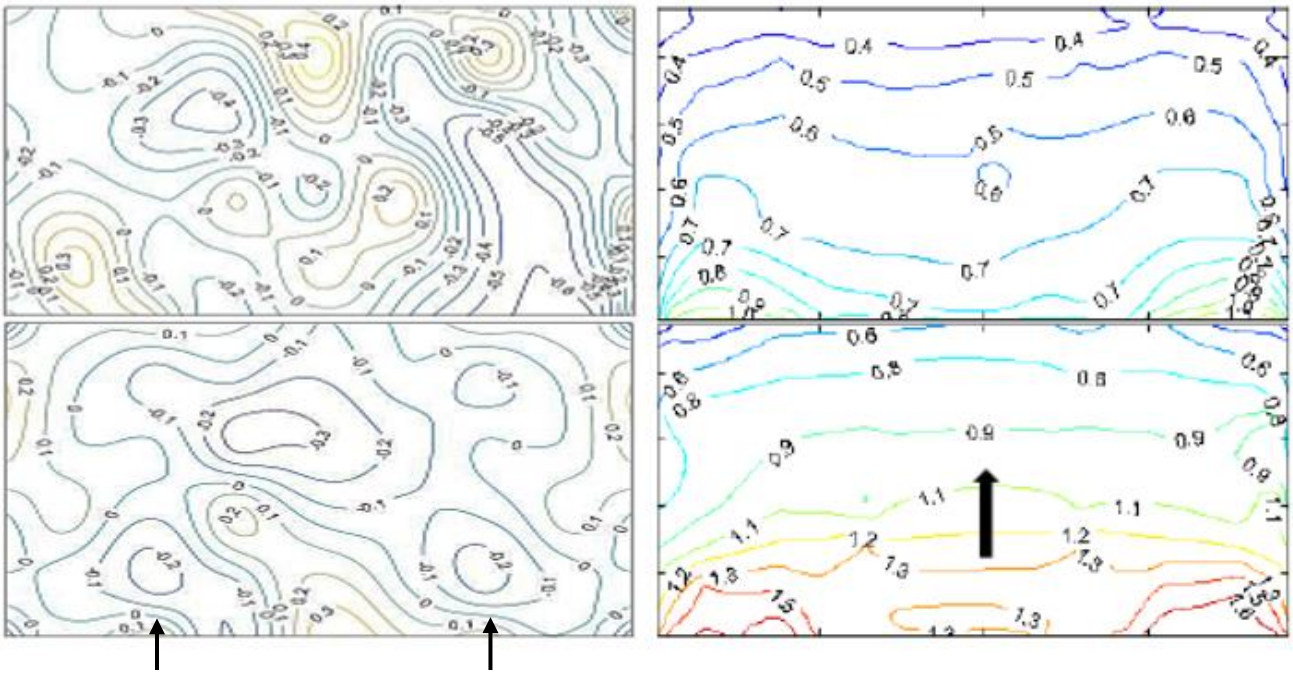

Present study Samani (2016)

Figure 4.30 Net Cp contours comparison with previous study (Samani, 2016) (0° AOI)

Even though the wind speed and the reference pressure are different due to different experimental testing conditions, the mean pressure coefficients along the mid-line and inlet-line of the panel were plotted in Figure 4.31 and Figure 4.32**,** respectively to be compared with the results previously obtained by Samani (2016) for the mid-line of a similar tested model. As can be seen, some disrepancies between the results are present. However, a similar effect of the 20mm gap was observed on the pressure coefficients distribution, where an abrupt change took place. Also, the pressure coefficients tend to follow different trends, since the experimental facilities used are different, thus the flow behavior and the boundary layers are not similar as well, as mentionned previously. Cp fluctuations and alternations between positive and negative values can be observed for both the inlet-line and mid-line results of the present study, which was different when compared with the mid-line Cp results from the previous study (Samani, 2016). This signifies that the wind flow simulated in the WDS is highly unstable, and leads to results different than the conventional boundary layer flows.

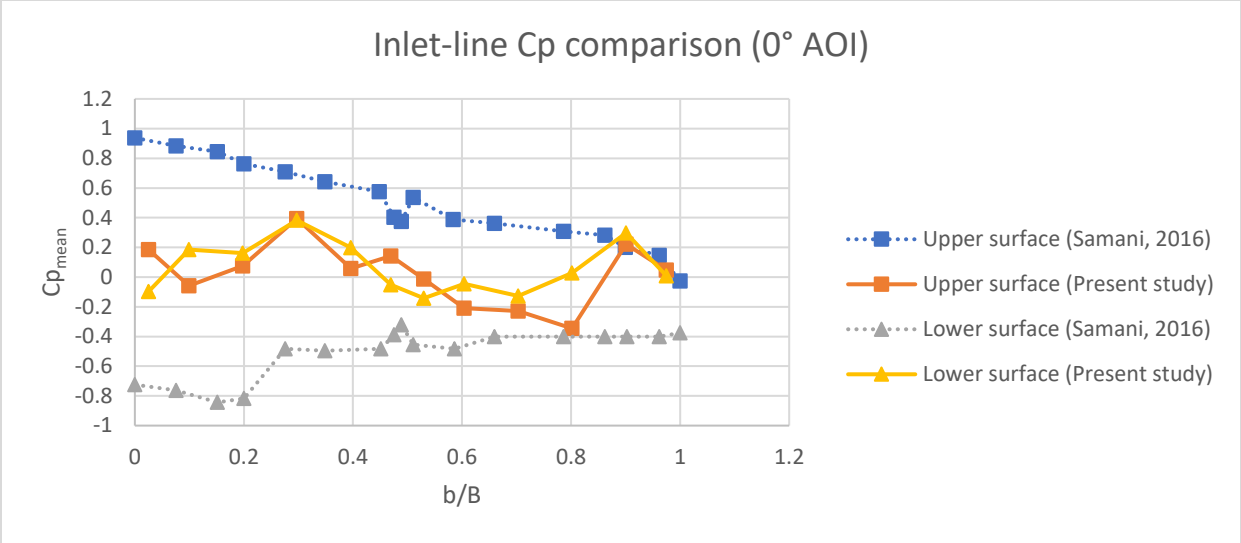

Figure 4.31 Inlet-line mean Cp (16.56 m/s) comparison with mid-line of previous study (15.88 m/s) (0° AOI)

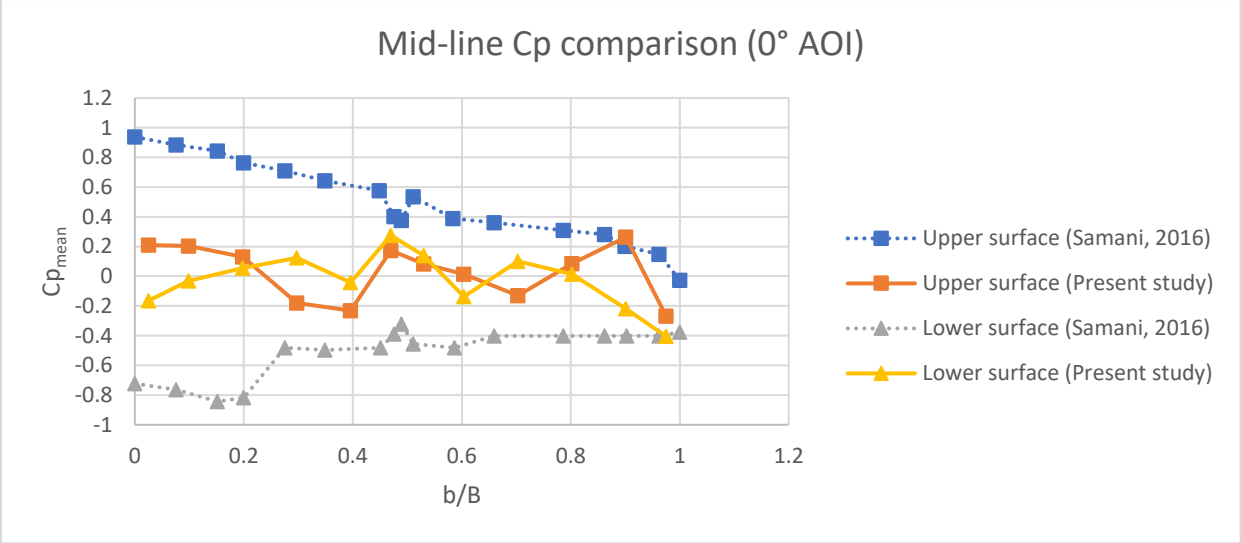

Figure 4.32 Mid-line mean Cp (16.56 m/s) comparison with mid-line of previous study (15.88 m/s) (0° AOI)

4.3 Wind-induced pressure coefficients for the 180° angle of incidence

The pressure coefficients were obtained for the 180° wind AOI for several wind speeds, ranging from 14.69 m/s to 41.71 m/s, however a software malfunction occurred for the 16.0 m/s wind speed case and the pressure values could not be fully recorded, thus the Cp data was disregarded. Some discrepancies of the pressure coefficients distribution along the panels were observed

between certain wind speeds therefore, the results were grouped into two categories to be discussed for the following wind speeds ranges, which are different than the wind speed ranges for 0° AOI:

Range 1: 14.69 m/s to 33.37 m/s,

Range 2: 35.46 to 41.71 m/s.

The values of the time-averaged pressure coefficients of the upper and lower surfaces were obtained through the experimental measurements, and the net pressure coefficient was determined and plotted for each of the investigated cases investigated. The sign convention was preserved as per the previously reported cases of 0° AOI, thus the positive pressure coefficient signifies that the wind is directed towards the respective surface and the negative pressure coefficient means the wind is directed away from the respective surface. Only the net pressure coefficient was reported in the current section, for the three lines: mid-line, inlet-line, and edge-line. It should be noted that the pressure coefficient results for the 0° AOI case were presented in detail whereas the ones corresponding to the 180° were only considered for the net pressure coefficient. The Cp along the mid-line, inlet-line and edge-line of the lower and upper surfaces of the tested panels can be found in Appendix A.

As previously described for the 0° wind AOI case, it is important to note that the first panel ends at b/B = 0.495, followed by the 20mm gap and the second panel, starting at b/B = 0.53, where B is the total length along both panels combined (1,990 mm) and b is the distance where the specific pressure tap reading was obtained along the line, as explained in the introduction of Chapter 4.

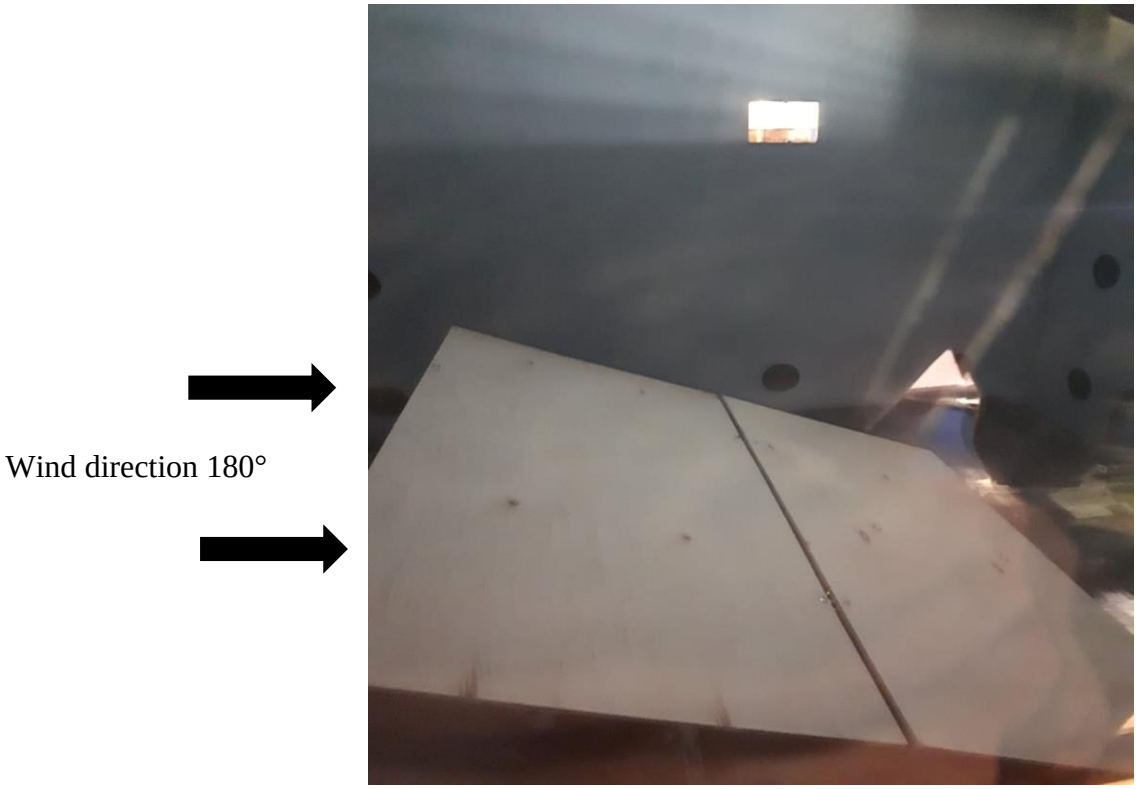

Figure 4.33 Inside view of the WDS with panels inside (180° AOI)

4.3.1 Cp_{net} along panels' mid-line for 180° AOI

The net pressure coefficients (Cp_{net}) along the mid-line of the panel for the speed ranges 1 and 2 are represented in Figure 4.34 and Figure 4.35, respectively. For all the tested wind speeds, the pressure coefficients started in the negative region (uplift) for the first panel and for the beginning of the second panel after the 20mm gap (at b/B = 0.53). For most of the wind speeds within the range 1 (Figure 4.34), the Cp_{net} along the mid-line had the critical negative values occurring near the beginning of the first panel, which could be attributed to the accelerated wind flow passing underneath the first panel, after being deflected by the panels surfaces. Along halfway of the mid-line, in the vicinity of the 20mm gap, the Cp_{net} increased on the first panel top edge, only to decrease on the second panel lower edge. The first panel was subjected to negative net pressure coefficients along the mid-line, except along the halfway of the mid-line and near the 20mm gap, for wind speeds ranging from 14.69 m/s to 22.82 m/s. The second panel was subjected to negative Cp_{net} along halfway of the second panel and when approaching the upper edge (at b/B = 0.98), where it increased to reach positive values. For the range 2 of wind speeds (Figure 4.35), it was

observed that both panels are subjected to negative pressure (uplift) along the entire mid-line, while experiencing the largest uplift Cp_{net} (negative) on the second panel at b/B = 0.6. Similarly, Cp_{net} increased on the first panel when approaching the gap, but the main difference from the first range of wind speeds was noticed where the net pressure coefficient decreased when approaching the top edge of the second panel, at b/B = 0.98 (Figure 4.35).

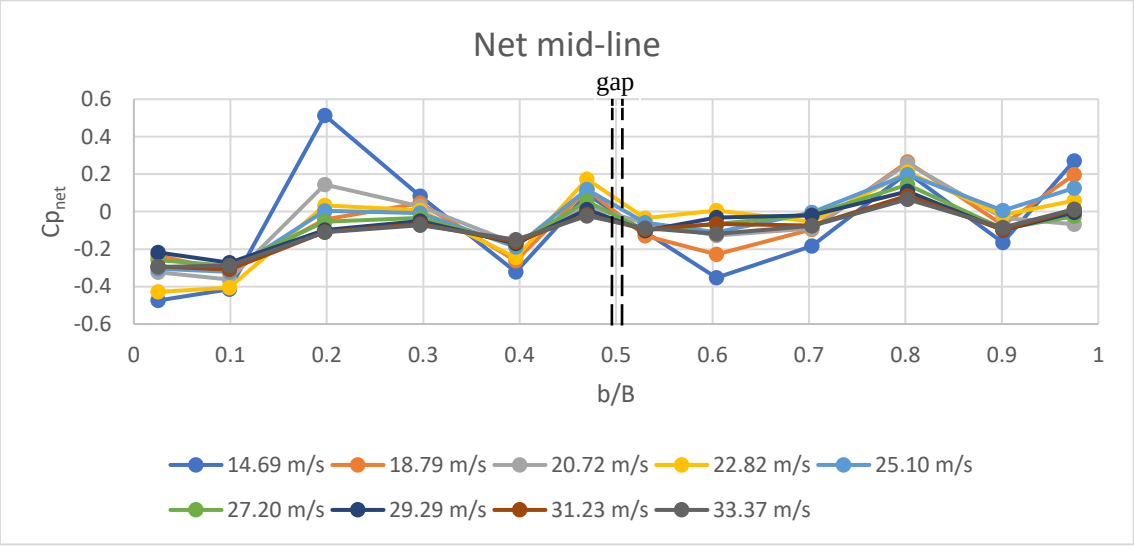

Figure 4.34 Net Cp variation along the mid-line (wind speed range 1, 180° AOI)

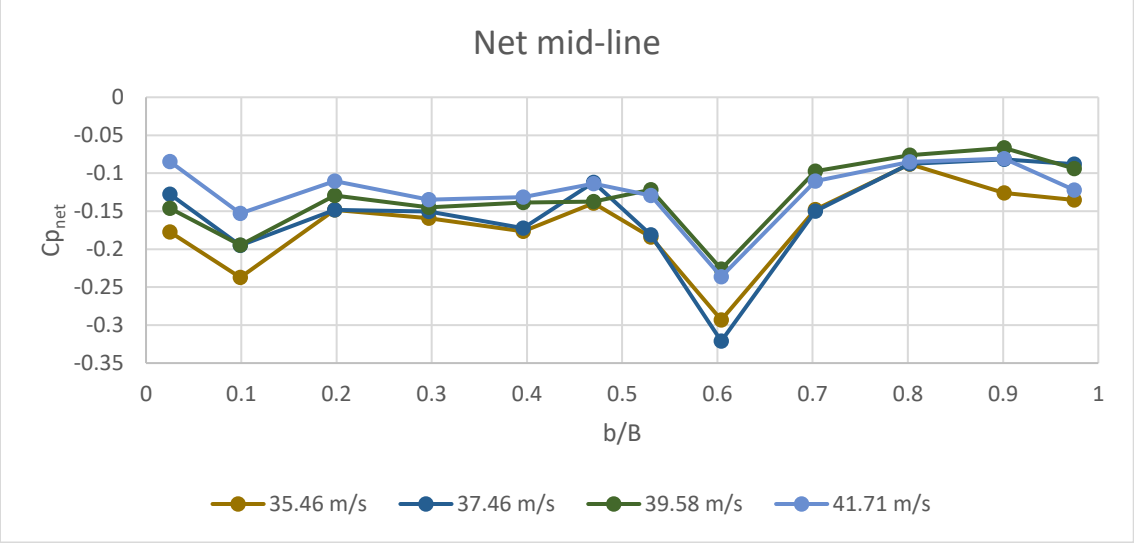

Figure 4.35 Net Cp variation along the mid-line (wind speed range 2, 180° AOI)

4.3.2 Cp_{net} along panels' inlet-line for 180° AOI

Along the inlet-line of the examined panels, the net pressure coefficients for the 180° wind AOI case were determined through the conducted experiment, and are represented for speed ranges 1 and 2 in Figure 4.36 and Figure 4.37, respectively. The Cp_{net} distribution was found to be similar for all the tested wind speeds along the inlet-line. Both panels were mostly subjected to negative Cp_{net} (uplift) along the inlet-line for the wind speeds of range 2 (Figure 4.37), except when approaching the 20mm gap (at b/B = 0.47), where a significant increase of pressure coefficient took place, reaching a positive value at the upper edge of the first panel. This behavior could be attributed to the suction outlet, located on the roof of the WDS right above the 20mm gap. For the wind speeds of range 1 (Figure 4.36), Cp_{net} was mostly in the negative region along the inlet-line of the panels except for the lower edge of the first panel, near the gap, around halfway and the upper edge of the second panel (b/B = 0.7 and b/B = 0.9), where the net pressure coefficient was positive. When approaching the top edge of the second panel, the Cp_{net} decreased for both speed ranges. For all the tested wind speeds, the maximum uplift value was observed at b/B = 0.4 along the inlet-line of the first panel, which is situated at the middle of the upper half of the first panel. On the lower edge of the first panel (b/B = 0.025), the Cp_{net} was positive along the inlet-line for most of the wind speeds of range 1, whereas the Cp_{net} was negative along the inlet-line for the wind speeds of range 2.

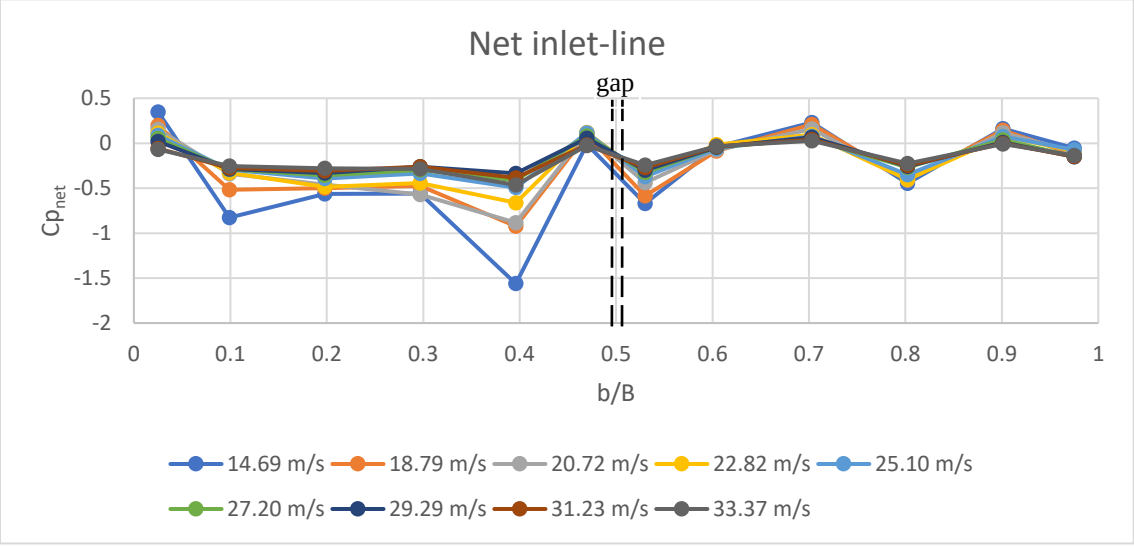

Figure 4.36 Net Cp variation along the inlet-line (wind speed range 1, 180° AOI)

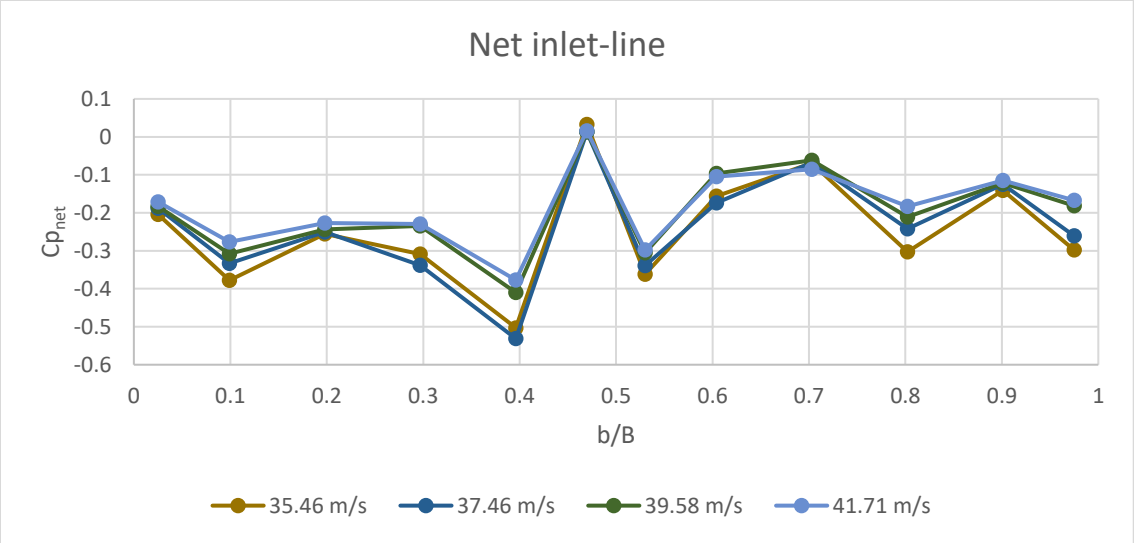

Figure 4.37 Net Cp variation along the inlet-line (wind speed range 2, 180° AOI)

4.3.3 Cp_{net} along panels' edge-line for 180° AOI

The net pressure coefficients along the edge-line of the panels were determined for the 180° AOI case. The results for the wind speeds of ranges 1 and 2 are determined and are illustrated in Figure 4.38 and Figure 4.39, respectively. Similar behaviour was observed for all the wind speeds; however, the location of the critical negative Cp_{net} differed between the two speed ranges. For the wind speeds of range 1, the maximum uplift Cp_{net} along the edge-line was observed on the first panel at b/B = 0.15 (Figure 4.38), whereas for the second range of speeds it occurred on the first panel at b/B = 0.35 (Figure 4.39). For all the examined wind speeds, the net pressure coefficient was found to be negative along the edge-line of the panels, except for wind speeds below 22.82 m/s, where the Cp_{net} reached positive values on the upper half of the second panel edge-line, around b/B = 0.75 and 0.85, before decreasing to negative near the upper edge of the second panel. The 20mm gap led to a decrease of uplift magnitude of the net pressure coefficient, where the lower edge of the second panel had a Cp_{net} value close to zero.

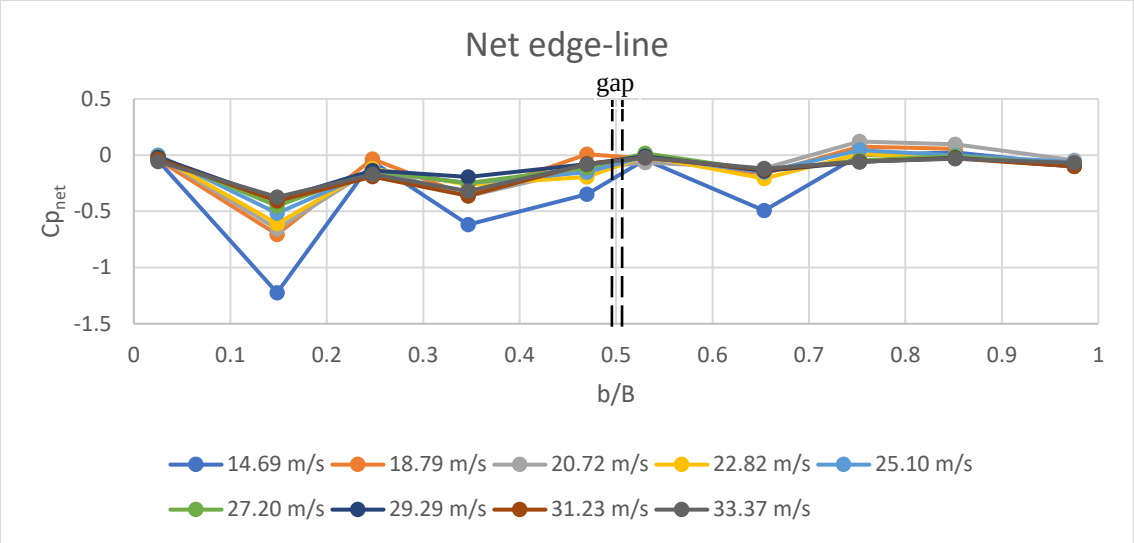

Figure 4.38 Net Cp variation along the edge-line (wind speed range 1, 180° AOI)

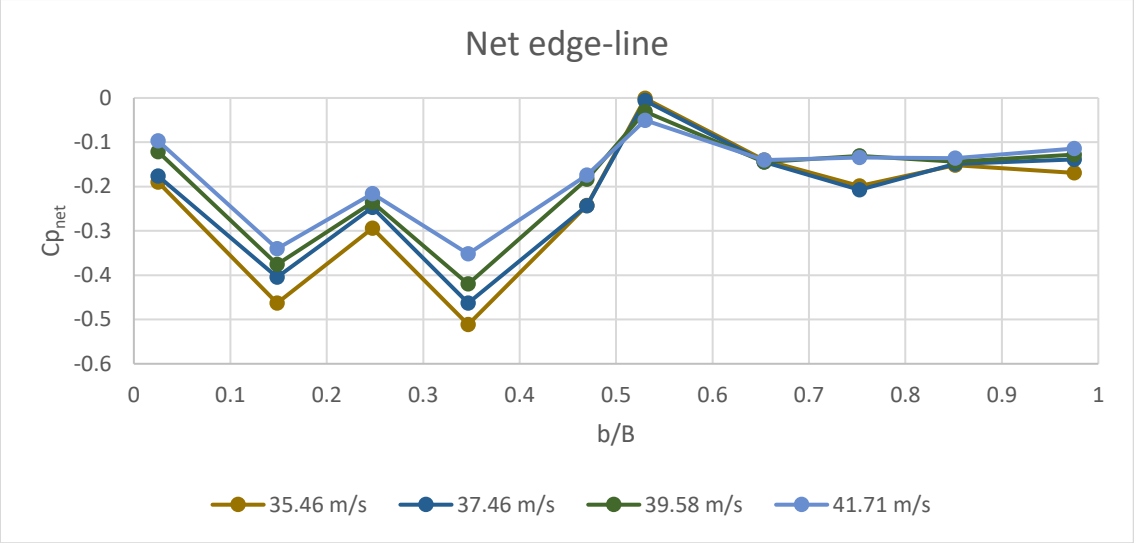

Figure 4.39 Net Cp variation along the edge-line (wind speed range 2, 180° AOI)

4.3.4 Cp contours along the solar panels for 180° AOI

The following Table 4.2 represents the contours for the mean upper, lower and net pressure coefficients, along the panels with 25° inclination setup, corresponding to one wind speed from each of the two ranges, 20.72 m/s and 37.46 m/s. When the panel is exposed to wind under 180° AOI, the flow hits the panels and is deflected by its surface, creating the pressure coefficient distribution.

The net pressure coefficients contours along the first panel showed uplift (negative Cp_{net}), with the most critical location being along the inlet-line, past half the first panel and close to the 20mm gap. Discrepancy was noticed between the two investigated wind speeds on the first panel, where past halfway of the mid-line, the net pressure coefficients became slightly positive for 20.72 m/s but remained negative for 37.46 m/s. In addition, between the inlet-line and the edge-line, positive net pressure coefficients were observed for the 20.72 m/s, whereas for the 37.46 m/s the negative pressure diminished. For the second panel, for the wind speed within range 2, the panel was subjected mostly to suction (negative pressure coefficient) along the mid-line, whereas for the wind speed within range 1, some regions of positive pressure coefficients were noticed, after the halfway of the mid-line. For the lower surface of the panels, highest Cp value occurred along the inlet-line of the first panel, and both panels' lower surfaces mostly underwent positive pressure coefficients. For the upper surface of the panels, under the 37.46 m/s wind speed, the panels were mostly subjected to uplift with the critical value occurring on the upper half of the inlet-line of the first panel (near the gap). For the 20.72 m/s wind speed, the most critical uplift pressure occurred at the beginning of the mid-line of the first panel near the edge, only to start diminishing until becoming positive beyond the halfway of the mid-line of the first panel, and then this decreased to reach negative values. This fluctuating Cp evolution could be due to the WDS outlet situated at the middle of the ceiling. For the second panel, the presence of the 20mm gap between the panels led to an increase of Cp along the mid-line, causing a positive pressure coefficient at the beginning of the mid-line and edge-line of the panel.

Table 4.2 Cp contours comparison for different wind speeds (20.72 m/s, 37.46 m/s) at 180° AOI:

Velocity	Upper Surface Cp	Lower Surface Cp	Net Cp
20.72 m/s	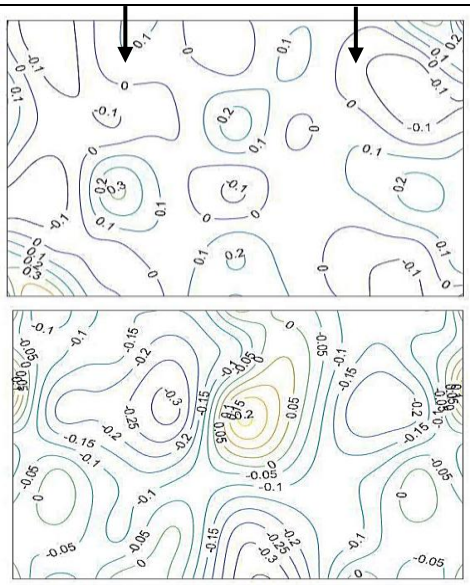	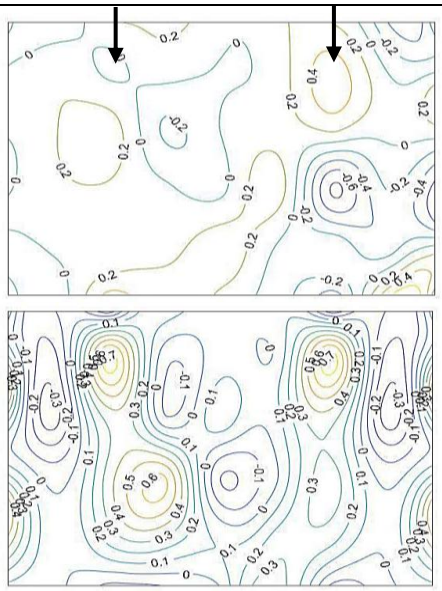	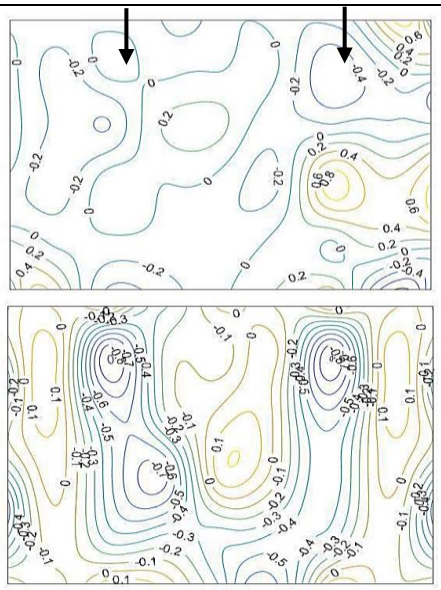
37.46 m/s	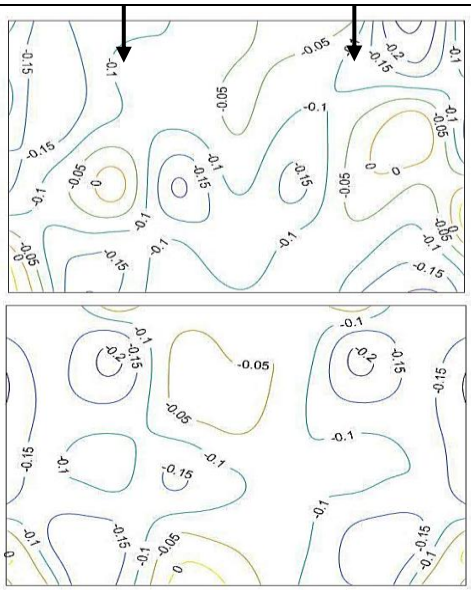	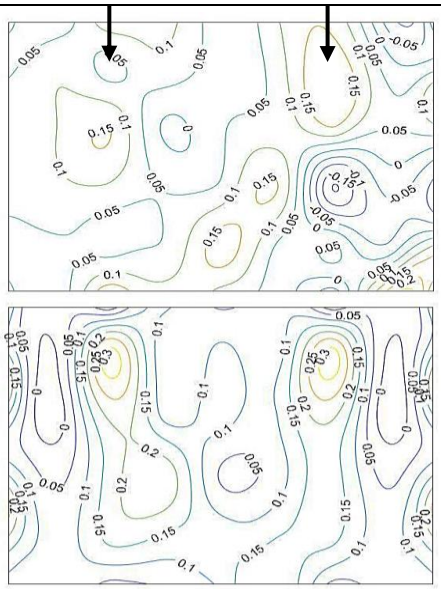	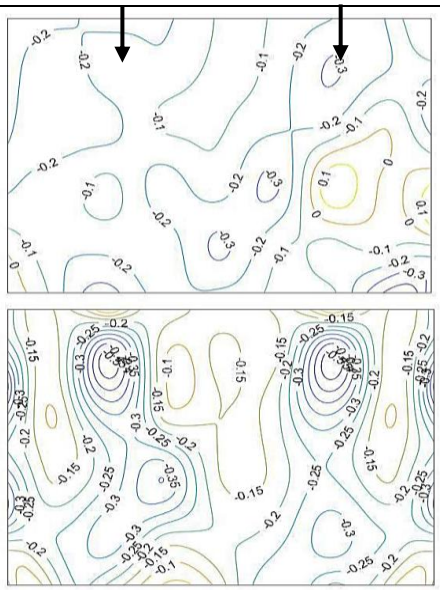

4.3.5 Comparison with previous ground-mounted solar panels study, for 180° AOI

For the 180° AOI, comparison of mean Cp results along the mid-line and inlet-line were conducted with the mean Cp along the mid-line of the previous study carried by Samani (2016), as shown in Figure 4.40 and Figure 4.41. The same model was used as for the 0° AOI, therefore the panel dimensions, inclination angle, solar racks and gap conditions are similar; however, some differences in the test procedure and analysis were present. The wind speed for the present study

was 14.69 m/s compared to 15.88 m/s for the study conducted by Samani (2016). The pressure coefficients measured in the current study on the upper and lower surfaces were more consistent with each other, when compared with Samani (2016), for which high positive and high negative Cp values were reported for the lower and upper surfaces of the panels, respectively. The results similarity was noticed especially for the inlet-line Cp results obtained in the present study, and the mid-line Cp results reported by Samani (2016) (Figure 4.41). The two studies reported similar Cp behaviour around the 20mm gap on the inlet-line, where its presence lead to an increase in Cp (in case of positive coefficients) and a decrease (in case of negative coefficients), when comparing the previous study (Samani,2016) Cp along the mid-line with the Cp along the inlet-line of the current study. In addition, it was noticed that the pressure coefficients decreased in magnitude the further the location on the line was, and when approaching the upper edge of the second panel.

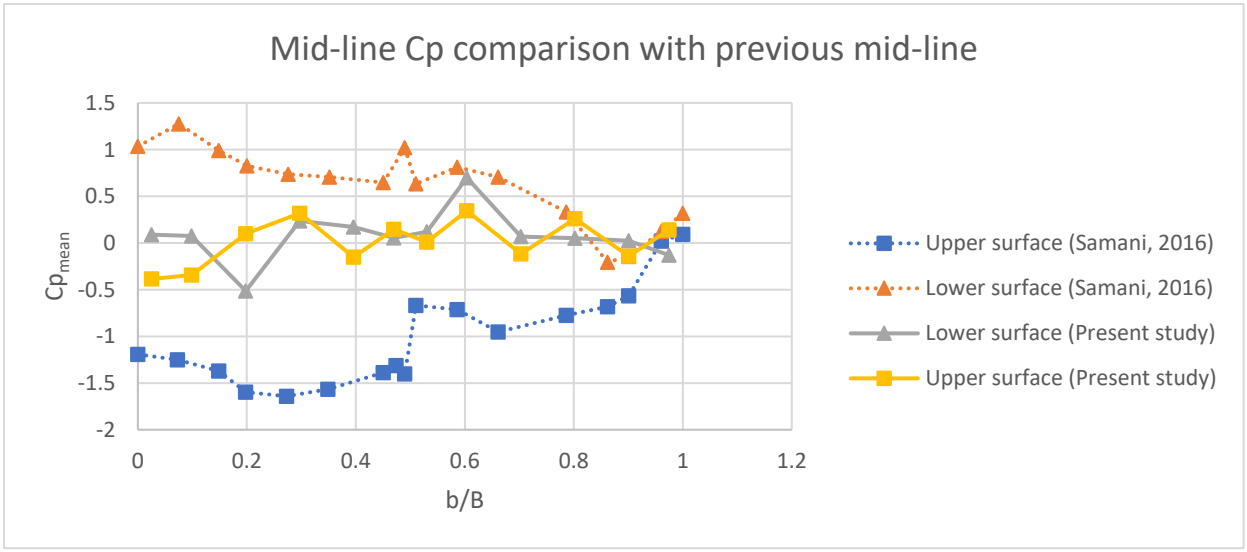

Figure 4.40 Mid-line mean Cp (14.69 m/s) comparison with mid-line of previous study (15.88 m/s) (180° AOI)

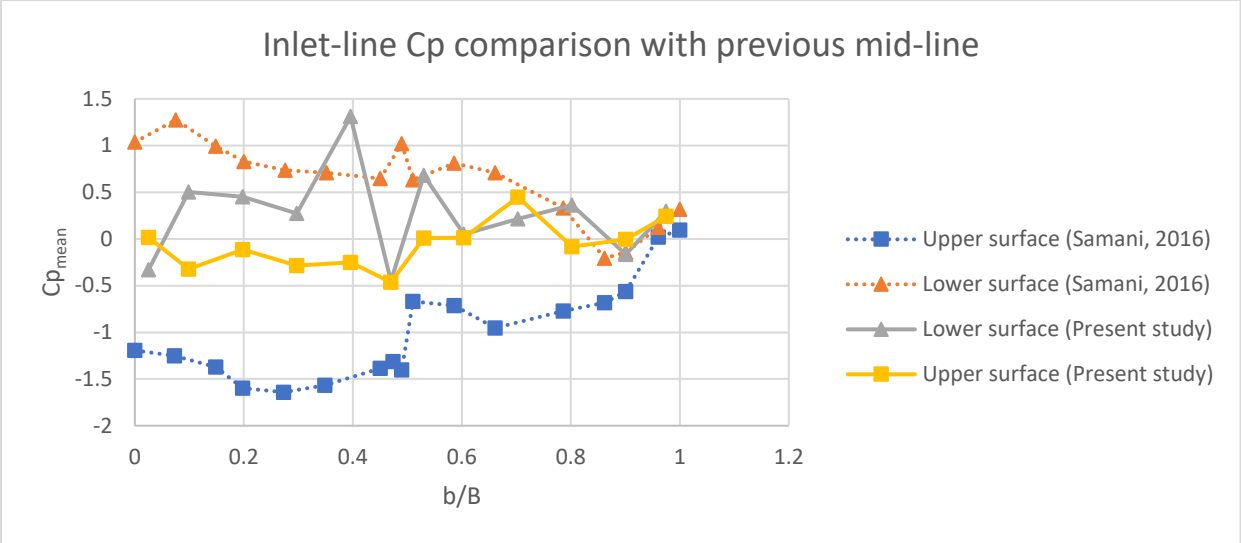

Figure 4.41 Inlet-line mean Cp (14.69 m/s) comparison with mid-line of previous study (15.88 m/s) (180° AOI)

4.4 The effect of the angle of incidence

The six different angles of incidence investigated (0°, 30°, 45°, 180°, 210°, and 225°) lead to pressure data obtained through the experiments, which were analysed, and the time-averaged pressure coefficients were calculated for each pressure tap. Table 4.3 and Table 4.4 represents the mean pressure coefficients contours on the upper surface, lower surface and the net pressure coefficients on the panels, for each of the six angles, according to a similar wind speed of 20-21 m/s, in order to avoid any discrepancy associated with the difference of wind speeds ranges. Also, it was noticed that the case with the highest suction and a sudden change of pressure coefficient on the panels system, was the 180° AOI case for which, especially on the first panel, underwent the most critical effects of the wind-induced pressure coefficient (highest uplift). The 30° and 45° AOI cases resulted in an alternation of net pressure coefficients along the line in between the flow coming from the inlets, similarly to the 210° and 225° AOI, as shown in the contours presented in Table 4.3. The highest Cp_{net} was observed for the 30° and 45° wind AOI cases, on the first panel at the lower edge and around halfway of the inlet-line, respectively. For the 180° wind AOI case, the most critical Cp_{net} took place on the first panel, along the inlet-line at the middle of the upper half of the panel. However, for the 210° and 225° AOI cases, the critical uplift Cp_{net} was observed on the second panel, along the line between the flows' direction, near the 20mm gap. The gap affected the results by reducing the uplift magnitude Cp_{net} on the first panel, however it also

increased the Cp_{net} uplift magnitude on the second panel. Critical negative Cp_{net} (uplift) was also noticed on the first panel along the line between the flow's directions of 30° and 45°, which leads to the conclusion that as the wind flow passes through the two opened inlets, suction, therefore wind flow moving away from the panels surfaces, was formed in between. For the 0° wind AOI case, positive Cp_{net} was formed at the point of contact with the first panel (windward edge), however negative Cp_{net} values were observed along the lines facing the inlets. This could be attributed to the suction effect on the flow by the outlet, experimental air leakage, or the wind passing below the first panel then being directed upwards towards the outlet, inducing uplift Cp on the panels.

Table 4.3 Cp contours comparison for different wind AOI (0°, 30°, and 45°)

Velocity	Upper Surface Cp	Lower Surface Cp	Net Cp
0°	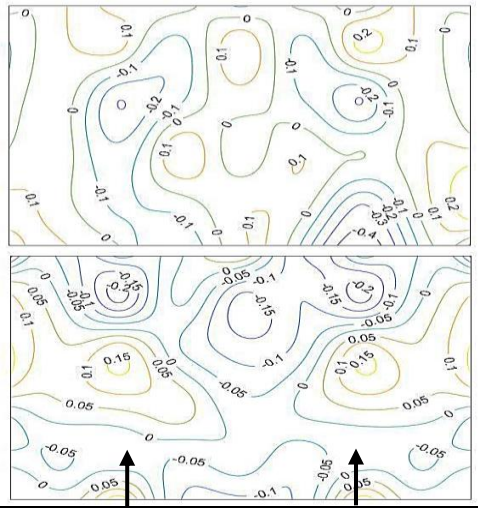	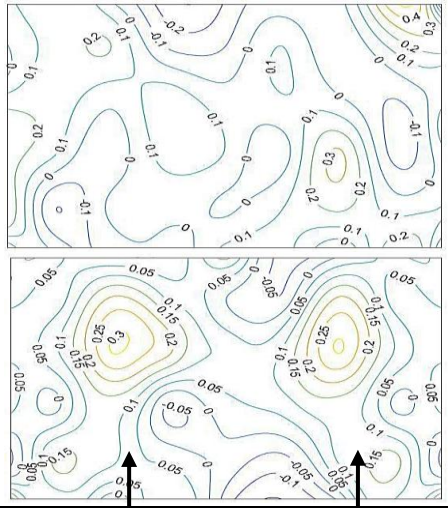	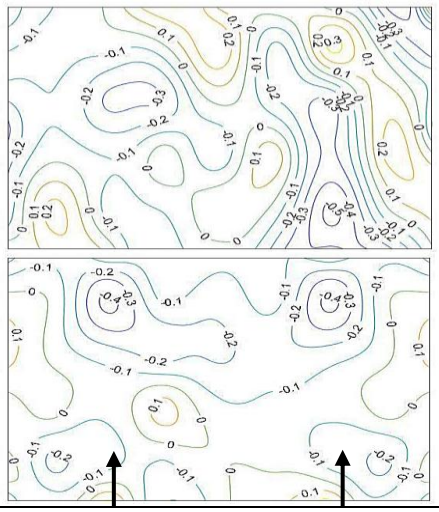
30°	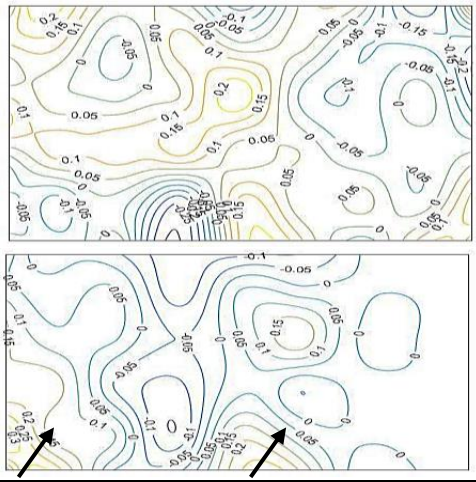	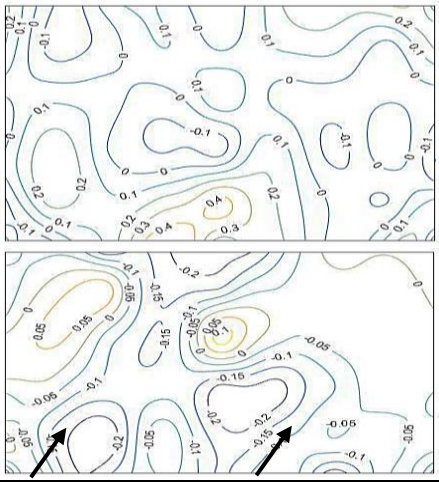	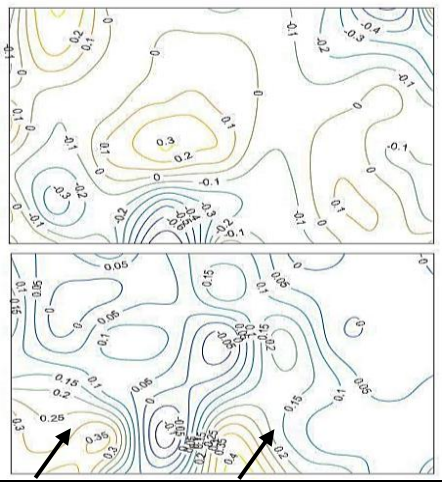
45°	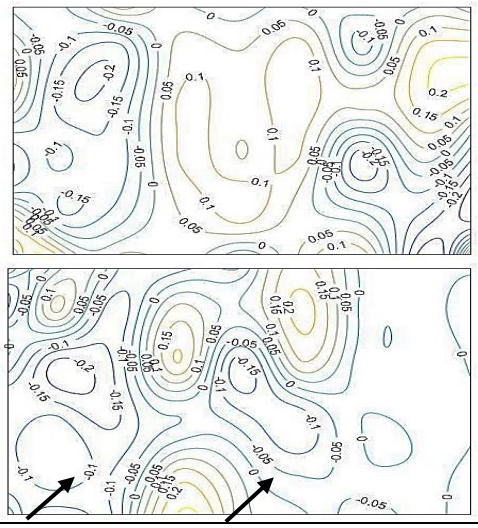	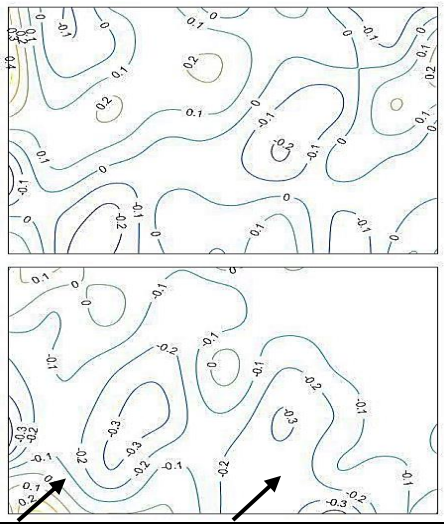	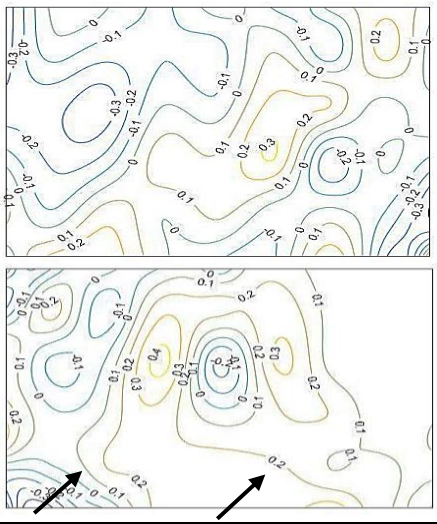

Table 4.4 Cp contours comparison for different wind AOI (180°, 210°, and 225°)

Velocity	Upper Surface Cp	Lower Surface Cp	Net Cp
180°	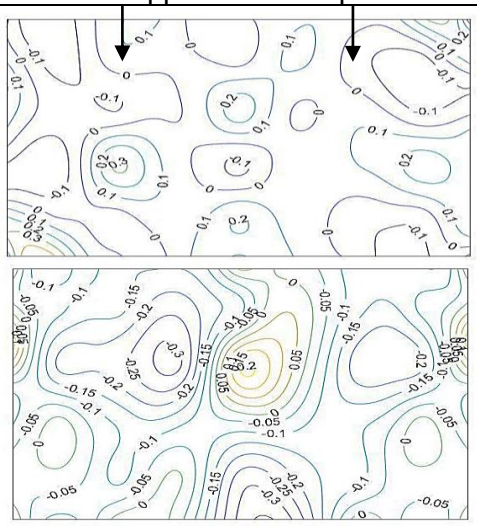	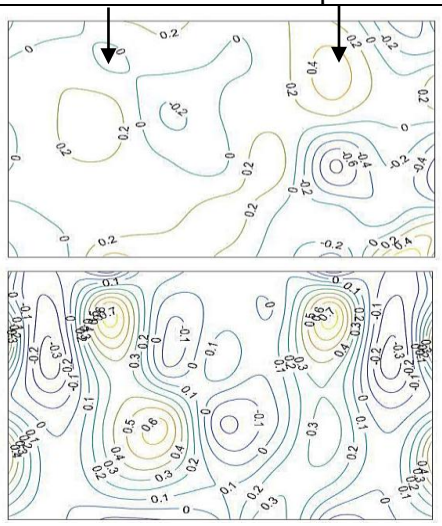	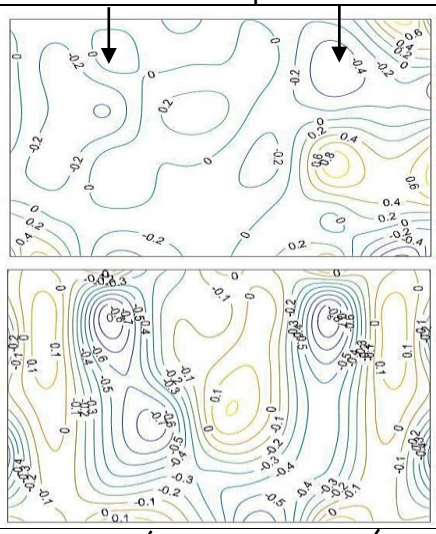
210°	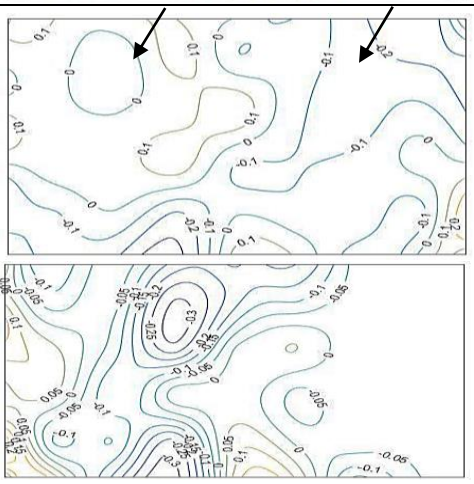	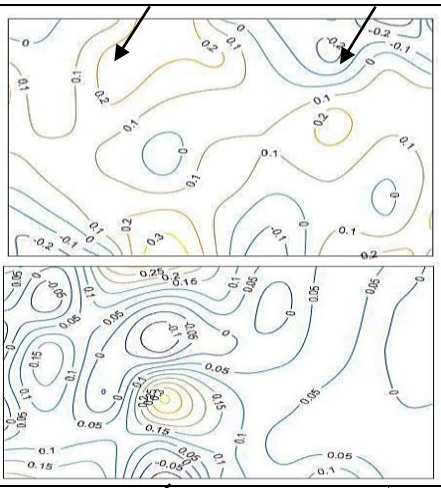	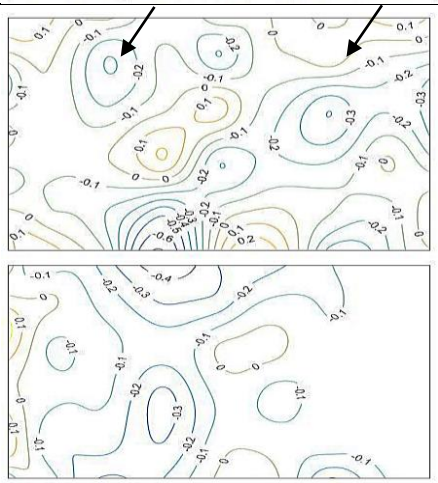
225°	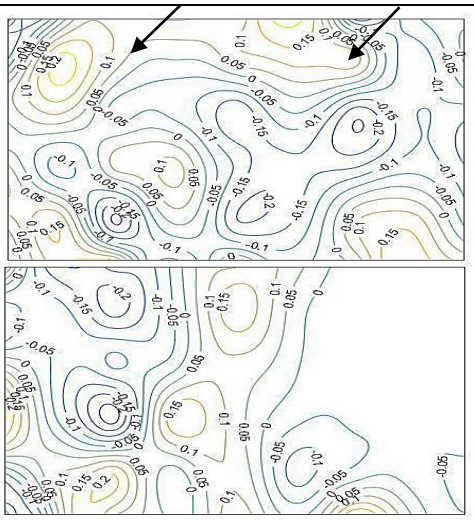	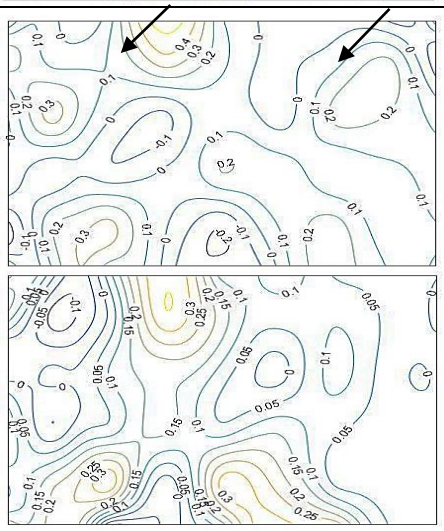	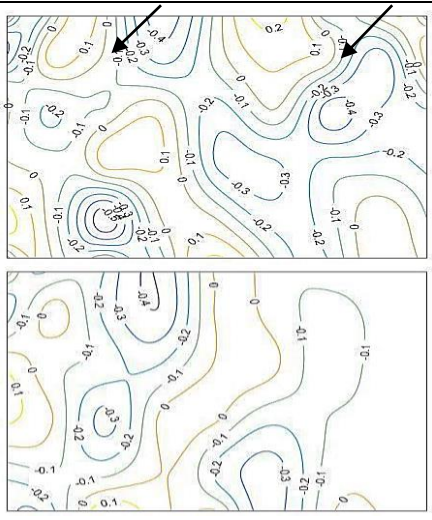

4.5 Mean equivalent pressure coefficient

Equivalent pressure coefficient, also known as normalized or area-averaged pressure coefficient, was calculated, by taking the Cp average along the tributary area of each pressure tap, for each of the six angles of incidence examined in this study.

4.5.1 Equivalent pressure coefficient Cp_{eq} for 0°AOI

The mean equivalent pressure coefficient, Cp_{eq}, for the 0° AOI case are plotted in Figure 4.42, Figure 4.43, and Figure 4.44. Typically in wind tunnel experiments, the results obtained for the mean Cp equivalent are in the positive range; however, the experiment conducted in the WDS facility led to negative Cp_{eq} results, as it can be seen in Figure 4.42, due to suction based flow simulated in the WDS facility by extracting the air through the top outlet. This experimental setting forced the airflow to be directed upwards away from the panel surface, thus producing uplift (suction) on the tested panels. From Figure 4.43 and Figure 4.44, it was noticed that the wind-induced equivalent mean pressure coefficient was slightly higher in uplift on the second panel than on the first panel, for most of the wind speed cases, except for 20.72 m/s where the Cp_{eq} value is lower in uplift (negative) than the one observed for the first panel.

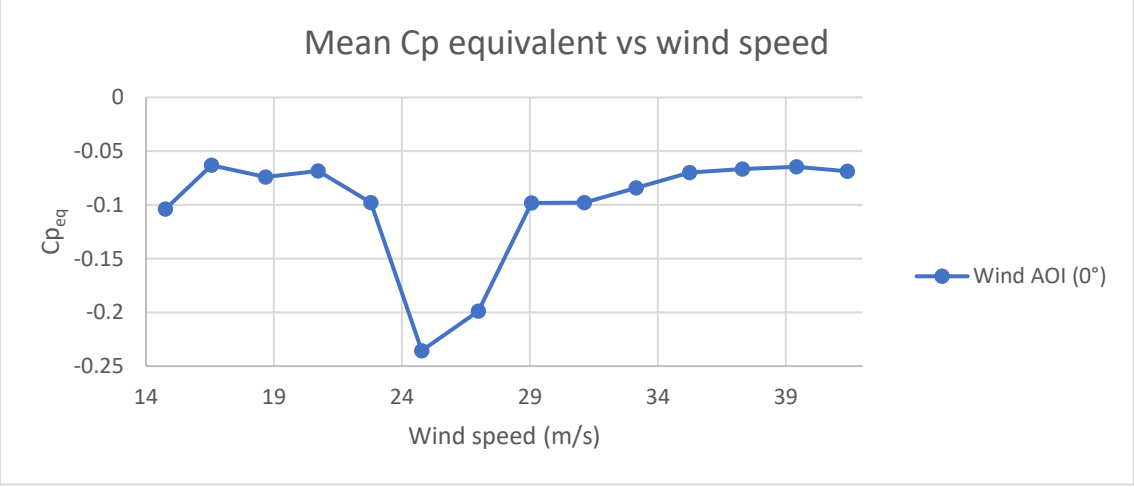

Figure 4.42 Mean Cp equivalent comparison for different wind speeds (both panels, °AOI)

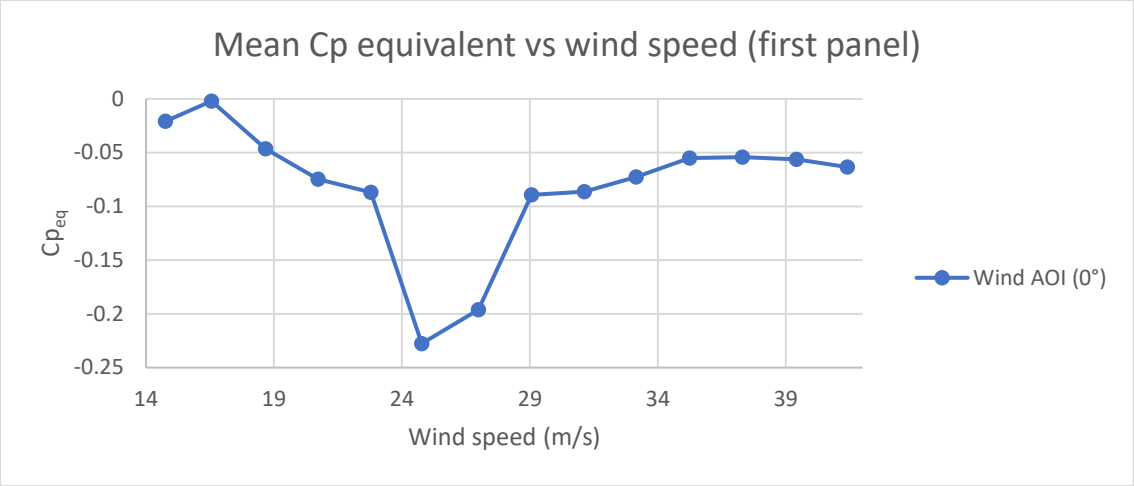

Figure 4.43 Mean Cp equivalent comparison for different wind speeds (first panel, 0° AOI)

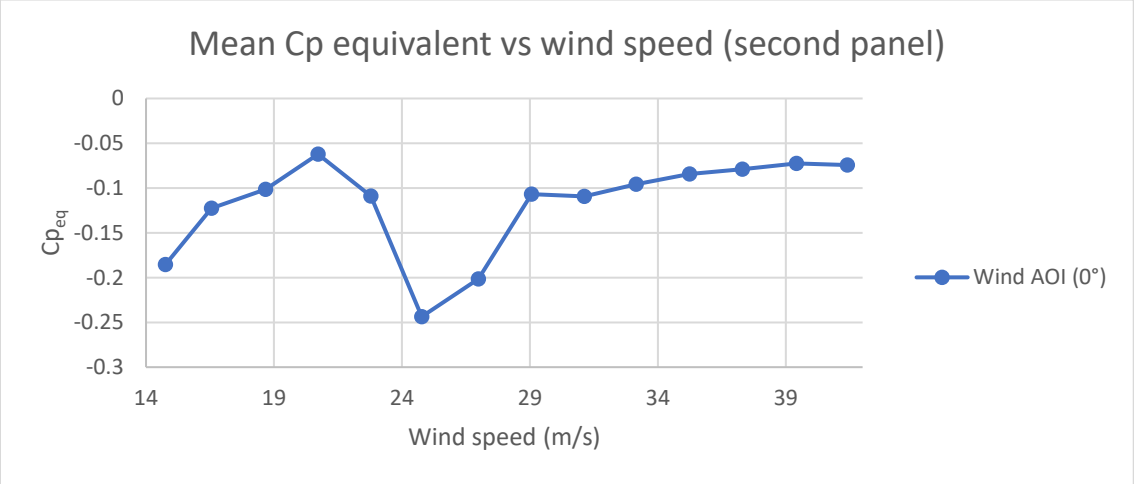

Figure 4.44 Mean Cp equivalent comparison for different wind speeds (second panel, 0° AOI)

4.5.2 Equivalent pressure coefficient Cp_{eq} for 180° AOI

The results of the mean Cp_{eq} for the 180° AOI case are plotted in Figure 4.46, Figure 4.47, and Figure 4.48. For the 0° AOI case, the mean Cp_{eq} of the first panel and the second panel had the same evolution and similar values. Whereas for the 180° case, the equivalent mean pressure coefficient on the first panel (Figure 4.46) was significantly higher in uplift magnitude (negative Cp_{eq}) than the equivalent mean pressure coefficient on the second panel, for most of the wind speed cases (Figure 4.47). This could be due to the fact that for the 180°, after hitting the first panel, the flow is deflected underneath the panel, or through the 20mm gap, diminishing and ultimately reaching the suction outlet at the top of the WDS without significantly impacting the second panel.

However, as shown in Figure 4.47**,** for higher wind speeds where the suction capacity is stronger (higher blower rpm settings), the wind flow is affected significantly by being directed upwards toward the outlet before hitting the first panel, while the second panel underwent significant negative pressure magnitude increase (suction).

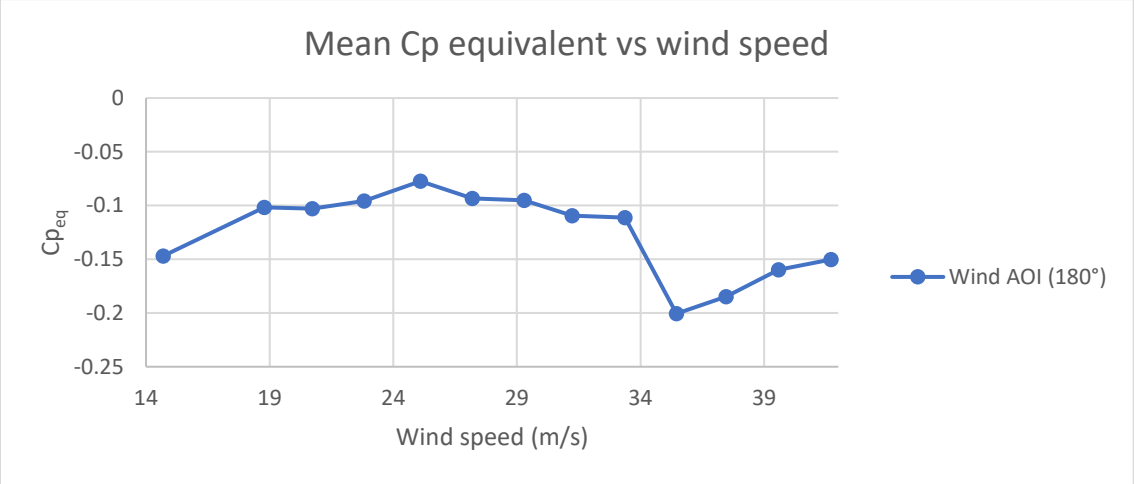

Figure 4.45 Mean Cp equivalent comparison for different wind speeds (both panels, 180° AOI)

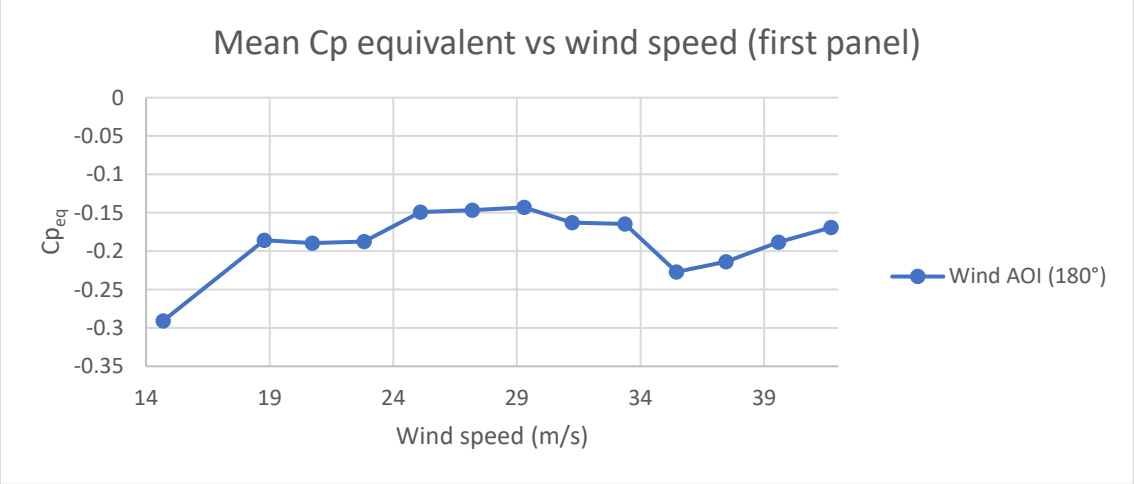

Figure 4.46 Mean Cp equivalent comparison for different wind speeds (first panel, 180° AOI)

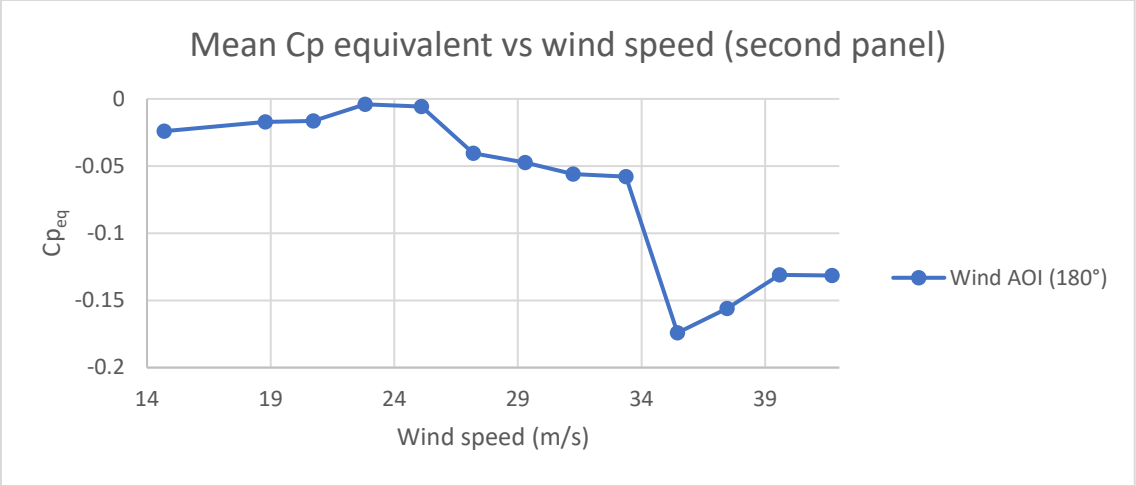

Figure 4.47 Mean Cp equivalent comparison for different wind speeds (second panel, 180° AOI)

4.5.3 Mean equivalent pressure coefficient for all the tested wind angles of incidence

The mean equivalent pressure coefficient results for the six angles are plotted in Figure 4.48**.** As shown in the graph, the critical wind AOI that induced the highest equivalent pressure coefficient was found to be for the 180° wind AOI, followed by the 0° wind AOI case, as can be seen in Figure 4.48. The wind speed 14.69 m/s used in the calculation was chosen since it was the closest wind speed to the wind speed of 15.88 m/s employed in the previous study (Samani, 2016), for comparison reasons. Similarly, Samani (2016) plotted the Cp_{eq} graph (Figure 4.49) for the wind speed of 15.88 m/s, and concluded that the 180° case induced the most critical equivalent pressure coefficient on the panels. From the present study, it can be concluded that the 180° wind AOI condition induced the most critical mean equivalent pressure coefficient on the panels. For the present experiment conducted in the WDS facility at 14-15 m/s wind velocity, the first panel underwent a higher suction effect than the second panel experienced for the 180° case.

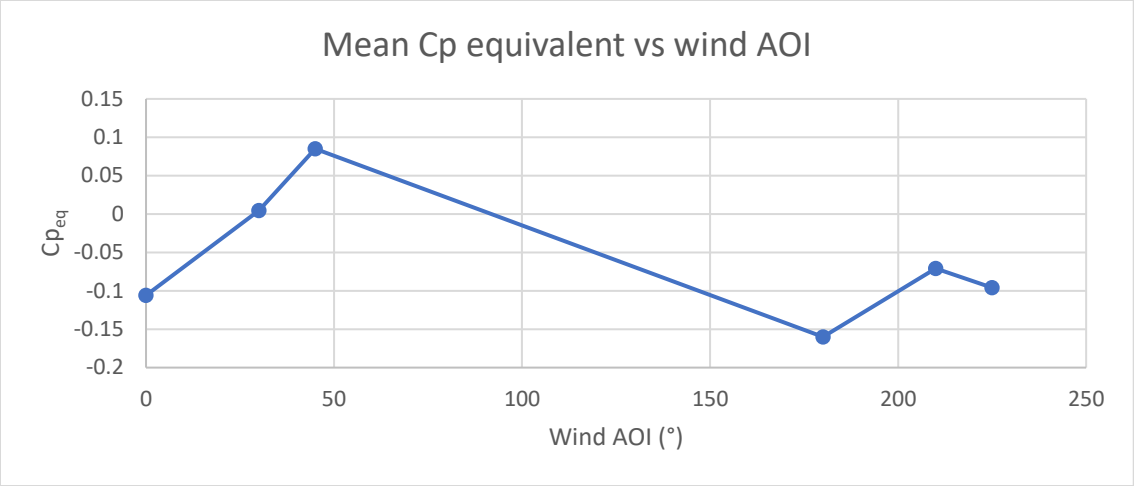

Figure 4.48 Mean Cp equivalent comparison for different wind AOI (Present study)

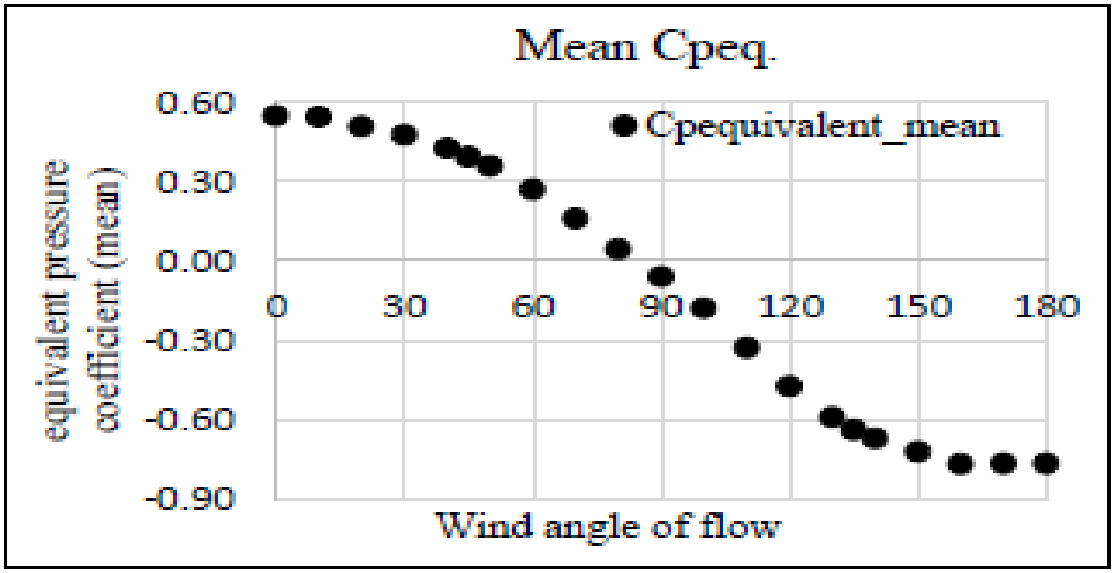

Figure 4.49 Mean Cp equivalent comparison for different wind AOI (Samani, 2016)

With the increase of angles from 0° to 45°, the mean equivalent pressure coefficient increased from the negative to the positive range in the present study (Figure 4.48), unlike the results obtained by Samani (2016), where the Cp_{eq} values started at 0° in the positive range then decrease with the increase of the angle of incidence. This could be due to the differences of the experimental facilities where the experiments were carried out.

Chapter 5 CFD Setup and Results

5.1 Introduction

Computational Fluid Dynamics (CFD) analysis can be carried out to numerically evaluate the wind pressure coefficient on the panels. In addition, CFD allows for visualizing the wind flow behavior inside the WDS facility when interacting with the tested panels, which can help for a better understanding and justification of the pressure coefficients distribution on the panels. The WDS was built recently, and it is a unique facility; hence, it is important to understand the CFD methodology that can be adopted, and the turbulence models, which can be associated with the wind flow simulated inside this facility, for future studies.

Prior to setting up the CFD model, a three-dimensional AutoCAD drawing representing the experiment was conducted, included in Appendix B. To avoid any mistakes in geometry, the model and the WDS facility were replicated with as many details as possible. After the drawing was completed, this was exported in 'IGES' format, to be imported in the CFD software. StarCCM+ CFD software was used in this study due to its economical aspect, accuracy, time efficiency and reliability (Kim, 2013), while AutoCAD software was used to draw the geometric domain. After importing the computational geometry, the boundary conditions, computational grid and the numerical models, which are best suited for the experiment, were selected. The examined cases are the 0° and 180° wind AOI, which were found to be the two critical cases in the analysis of the experimental results (Chapter 4).

5.2 Geometric model

The experimental setup was modelled with the same panels' dimensions (two 985 mm x 1960 mm with a thickness of 12.7 mm) as used in the WDS experiment (Figure 5.1) and similar test configurations such as the 20mm gap and 25° inclination angle were implemented in the CFD analysis. The WDS facility and the solar frames were also modelled in the CFD simulations, as per the dimensions presented in Chapter 3, with as much details as possible to avoid any geometry related effects. The blower and the duct were not included in the model, since the flow can be

simulated through the top outlet by having the wind directed upwards. This was deemed more suitable since it is more computationally economical (smaller domain) and the same outcome is expected.

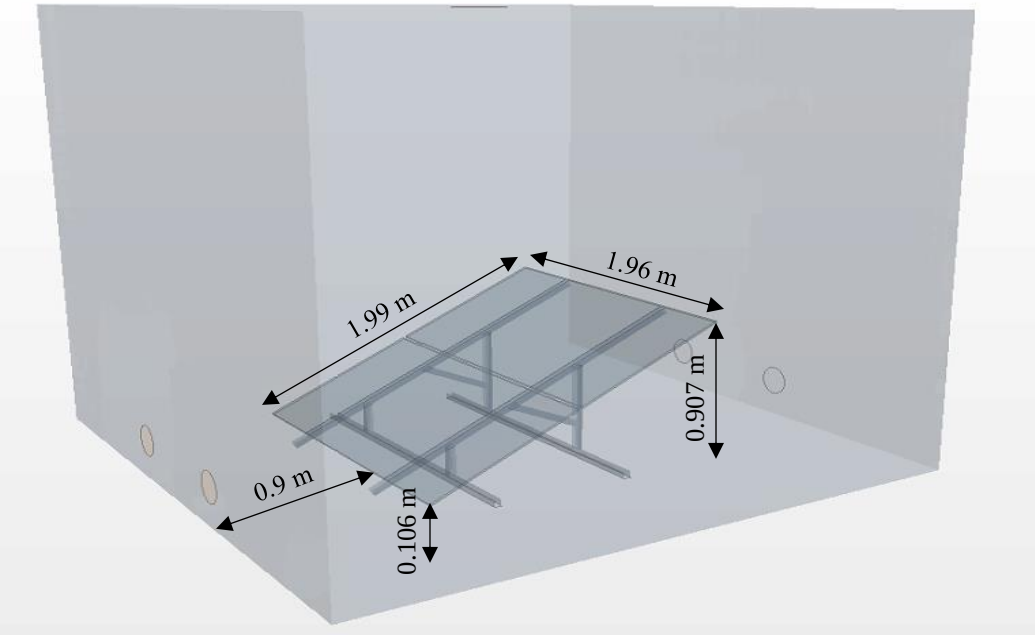

Figure 5.1 Three-dimensional view of the WDS computational geometry (dimensions taken from upper surface of the panels)

5.3 Numerical model

The three-dimensional RANS turbulence model was used to determine the initial flow conditions around the solar panels, later employed by the LES turbulence model, which allows for more accuracy and details in turbulent flow cases than the RANS model (Kim, 2013; Franke et al., 2007). Since the flow in the WDS facility is highly unstable and turbulent, this method was chosen to be the most suitable for the CFD analysis.

For the initial conditions, the shear stress transport (SST) k-ω turbulence model (Menter, 1994) was selected, based on the fact that this model provides good performance for predicting flow behavior around bluff bodies (Yang et al., 2009). Several previous studies have adopted the SST k-ω turbulence model for ground-mounted solar panels studies (Jubayer and Hangan, 2014; Jubayer and Hangan, 2016; Reina and De Stefano, 2017). In addition, Shademan et al. (2014) concluded that the SST k-ω model is more suitable than the realizable k-ε model for flow

simulation around ground-mounted solar panels. After convergence was reached, the unsteady LES with Dynamic Smagorinsky subgrid scale model (Germano et. al, 1991) was employed. Second order implicit scheme was selected for the temporal discretization and the MUSCL (Monotone Upstream Centered Scheme for Conservation Laws) 3rd order (Van Leer, 1979) was used as the spatial discretization scheme. The time-step was selected as 0.0004 s for maintaining the Courant number below one, which in definition signifies that the flow is not travelling further than one cell along each time step. Moreover, 20 inner iterations were specified for each unsteady time-step. Stability and convergence are accomplished by having residuals values below 10^{-4} for each time-step, and over a physical period of 2.6 seconds.

In the WDS experiment, the outlet wind speed was the only setting that was constant and controlled, accomplished by selecting the rpm of the blower connected to the outlet. Hence, the boundary conditions of the CFD domain were set, such that the outlet located on the ceiling of the WDS was defined as "velocity inlet" with a value of 14 m/s directed upwards, to numerically simulate the experiment as accurate as possible. As for the lateral inlets, they were defined as "pressure outlet" with zero-gauge pressure. This yielded to an inlet lateral velocity of around 16 m/s to 16.4 m/s, as incoming wind flow towards the inside of the WDS, initiated by the pressure difference induced by the outlet. For all the other parts of the experimental setup such as the solar panels, the panels' frame and the WDS walls, these were defined as no-slip, no-penetration "wall" boundaries. The air in the box was defined with an atmospheric density, ρ, of 1.2047 kg/m^3 and a dynamic viscosity, μ, of 1.8205 x 10^{-5} Pa·s, corresponding to the experimental air temperature of around 20°C.

5.4 Grid sensitivity analysis

Mesh or computational grid was defined by dividing the geometrical domain into multiple elements, which allows the StarCCM+ software to solve the necessary equations with respect to the grid nodes and cells. The smaller the elements are, the more accurate the results will become. However, this comes with a consequence on the computational cost of the analysis, since smaller grids lead to more cells for the software to solve. Thus, it is important to select the appropriate computational grid to avoid any effects on the convergence criteria and on the efficiency of the

results, while being computationally economical at the same time. Local mesh refinement and sensitivity analysis were conducted through volumetric controls, which limits the number and size of the mesh cells, while determining the adequate results.

As recommended by several studies (Franke et al., 2007; Tominaga et al., 2008), hexahedral meshing was employed. Mesh refinement was carried out for the numerical CFD study around the inlets, outlet, solar panels and frame. To select the appropriate computational grid for the simulations, mesh sensitivity analysis was conducted. Table 5.1 represents the three different meshing examined: mesh A, mesh B and mesh C, and are shown in Appendix B. For the numerical simulations, a computer with an Intel® Core™ i-7-4770 CPU @3.40 GHZ processor was used, with 12 GB of installed memory (RAM).

Table 5.1 Size and computational cost for different meshes

Mesh	Number of cells	Solution time required (days)
A	975,251	7
B	2,174,941	16
C	2,887,483	23

The grid sensitivity analysis was conducted for the LES solution, due to the fact that this requires more cells equivalent to smaller mesh size, to reach convergence when compared with RANS algorithm. Performance is judged based on several criteria such as: the average velocity line from the inlet to opposite wall (with panels), the plenum pressure and the inlet average velocity. Graphs were plotted to visualize mesh size effect on the lateral inlet velocity (Figure 5.2) and on the plenum pressure (Figure 5.3). It was observed that meshes B and C converged and reached very similar results, around 16.2 m/s and -160.8 Pa for inlet velocity and plenum pressure, respectively, while for the mesh A, the inlet velocity and plenum pressure were respectively around 16.5 m/s and -165.4 Pa.

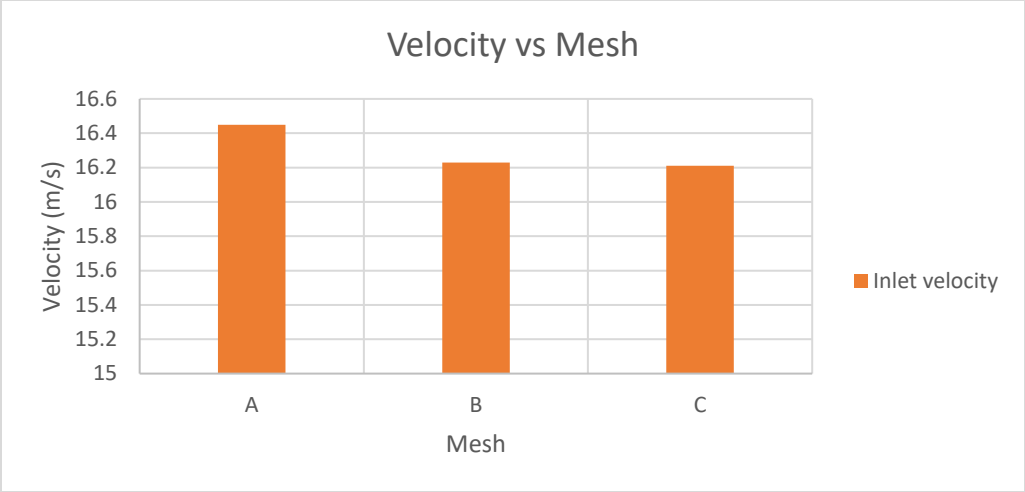

Figure 5.2 Inlet velocity comparison for different mesh sizes (0° AOI)

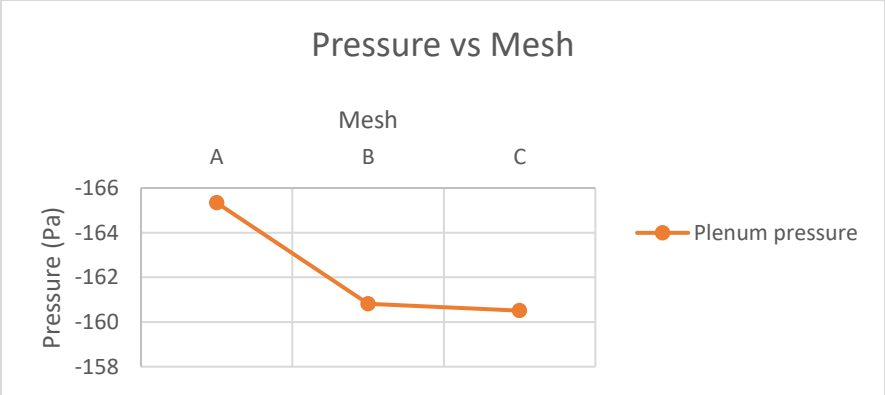

Figure 5.3 Plenum pressure comparison for different mesh sizes (0° AOI)

Figure 5.4, representing the average velocity on the line spanning from the inlet to the opposite wall, shows a similar behavior for mesh B and mesh C. The wind speed decreased slightly with the horizontal distance across the WDS chamber. A sudden drop in wind velocity magnitude was noticed at a distance of 1.3 m, which is due to the wind-panel contact point located 1.24 m from the inlet. As can be seen in Figure 5.4, good agreement can be noticed between the wind velocities obtained for mesh B and mesh C, especially at the end (near the opposite wall at a distance of 3.6 m) and at the contact point between the wind flow and the first panel, where an increase of velocity occurred for mesh A. This was the opposite of the trend that occurred for mesh B and mesh C, where the velocity decreased. Taking into consideration the computational cost and the good agreement of the simulation results, it was decided that mesh B (Figure 5.5), formed by approximately 2,175,000 cells, was the most adequate for the numerical simulations. Solution convergence was reached at around 2.6 s of physical time (124,000 iterations).

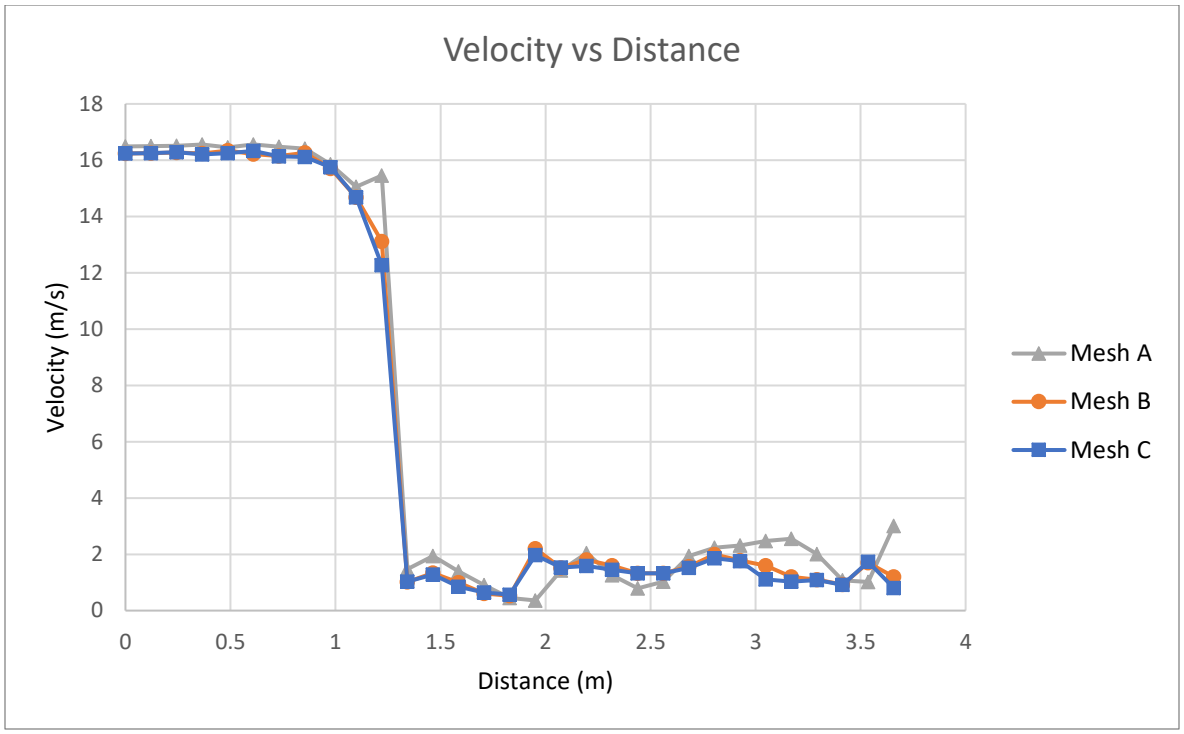

Figure 5.4 Mesh comparison of the velocity along the inlet to opposite wall line (0° AOI)

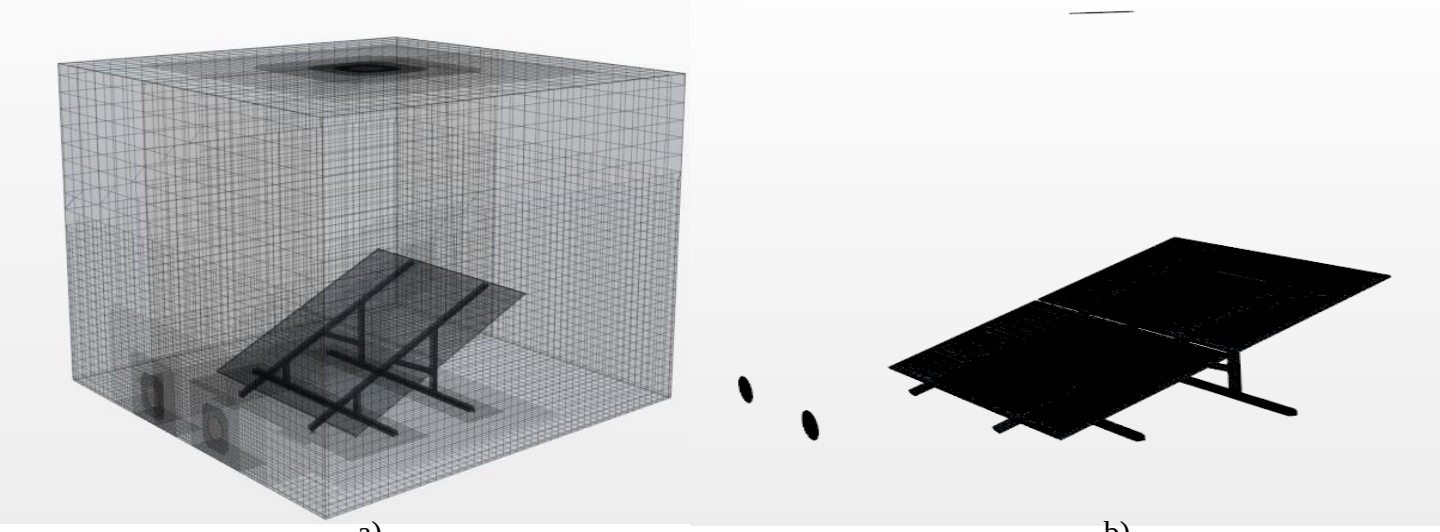

a) b)

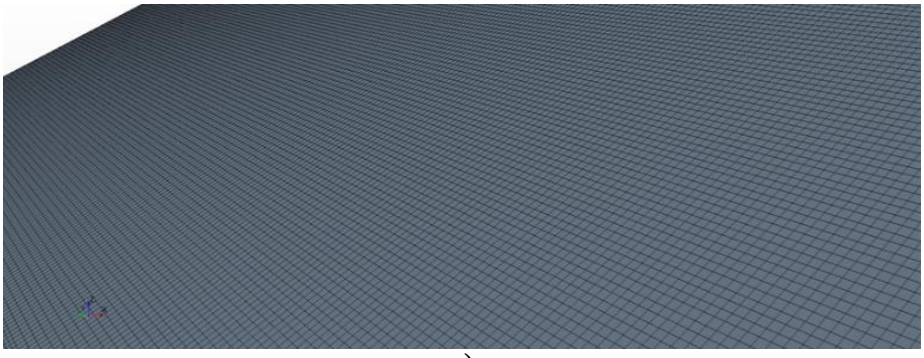

c)

Figure 5.5 Computational grid (mesh B): a) WDS and panels module isoparametric view, b) panel and inlets mesh refinement, c) close-up view of the cells on the surface of the panels

5.5 Numerical results for RANS and LES at 0° wind AOI

As mentioned previously, the RANS turbulence model was used only until reaching the converged solutions, which was then used as initial conditions for the LES model. The flow velocity profile was plotted for the RANS and LES simulations in Figure 5.6, with the presence of the panels. Values are obtained along a vertical line, located between the inlet and the panels, ranging from the ground to the ceiling of the WDS facility. The comparison shows a good agreement between the two models, with the maximum velocity occurring at the height of the inlet-center, where a sudden increase occurred around the height of 0.21 m.

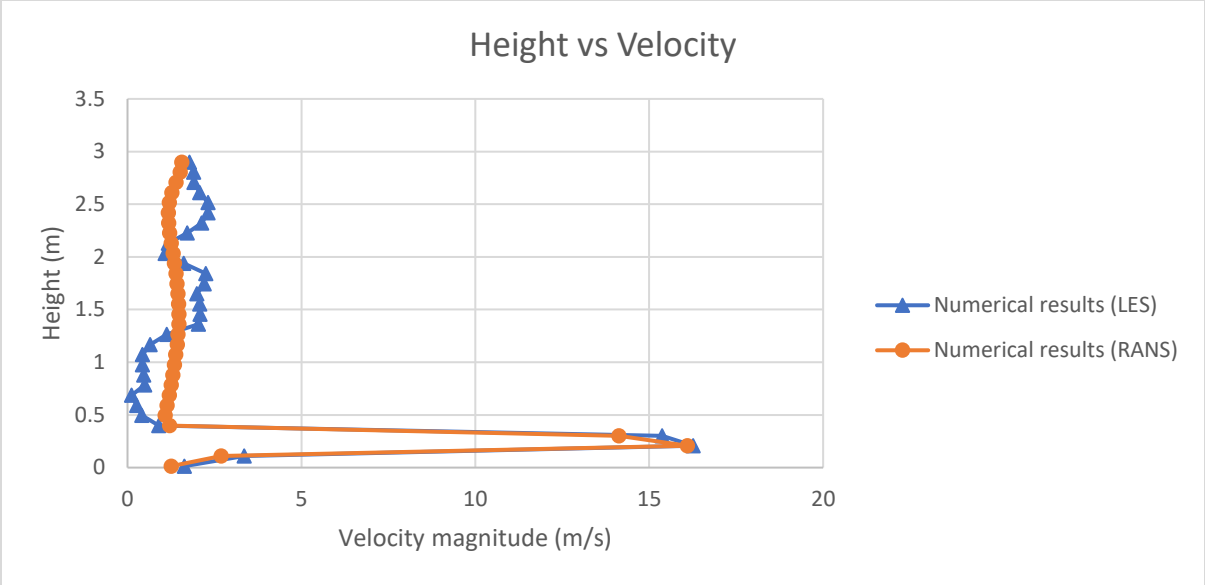

Figure 5.6 Numerical wind velocity magnitude profile between inlet and panels

5.5.1 Numerical Cp contours along the solar panels for 0° AOI

Pressure coefficients, obtained from the experimental and numerical RANS results, are presented in Figure 5.7. As expected, RANS model does not replicate the experiment very well, especially for highly turbulent flows. It was observed that there were no fluctuations, nor variation in the pressure coefficient contours on the upper surface of the panels, as shown in Figure 5.7. The inlets location resulted in the highest positive Cp on the panels, which diminished along the distance. Same can be observed for the pressure coefficients distribution along the mid-line, where a positive Cp can be noticed halfway of the first panel; due to the redirection of the flow towards the middle after hitting the first panel, following a diminishing trend along the panels (Figure 5.7). In addition to the absence of the Cp alternations along the panels, it also resulted in an underestimation of the negative pressure coefficient magnitude when compared with the experimental results. The numerical RANS Cp value was -0.05 compared to the experimental Cp value of -0.4. The advantage of using RANS is that it requires less time, lower grid density and limited computational resources to reach convergence, when compared with LES. However, it does not provide adequate results for scenarios where high turbulence is present in the wind flow. It provides good initial conditions for the LES model, minimizing the computational cost, therefore LES was used for the CFD simulations replicating the WDS experiment performed on the solar panels model.

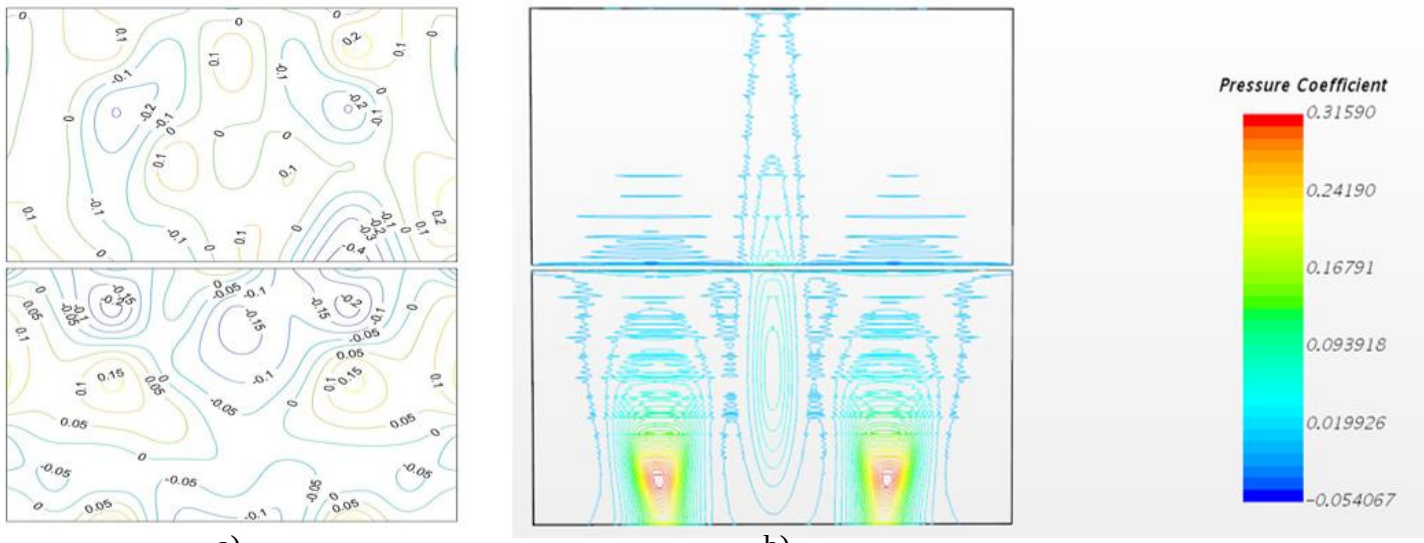

a) b)

Figure 5.7 Pressure coefficient (0° AOI) contours along the solar panels' upper surfaces: a) experimental results, b) numerical (RANS) results

When unsteady (LES) conditions were employed in the CFD software, the pressure coefficient fluctuated more around the upper surface of the panels and varied from negative to positive values registering contour patterns similar to the experimental results, as can be seen in Figure 5.8. The numerical results obtained through the LES model predicted better the magnitude of the pressure coefficient determined from the experimental results. However, it overestimated the positive Cp near the point of contact between the wind flow and the first panel, where the Cp value obtained from the LES simulation was 0.52 compared to the experimental Cp value of 0.15 (Figure 5.8). This discrepancy could be caused by the experimental WDS flow, which had more dispersion when the wind is directed towards the panels through the inlets. From the upper surface pressure coefficients contours, it was observed that the WDS experimental flow was more dispersed, when compared with the WDS simulated flow, specially at the wind-panel contact point. The resolution of the pressure taps used in the experiment affects the pressure coefficient distribution, where there were only around 96 taps monitored at the surfaces of the panels, much lower compared to the numerical simulations, which employed around 110,000 measured points on the panels' surfaces. For the pressure coefficients along the lower surfaces of the solar panels, the numerical results were not comparable with the experimental results. The numerical pressure coefficients result for the lower surface were negligible with little to no variation, except near the 20mm gap and edges, as it can be seen in the graphs included in the Appendix B. Air leakage in the experiment, due to WDS displacements through crane usage, or due to the flow circulation through the gaps at the

contact with the floor, could be the reason of such difference with the experimental results, where significant Cp values were noticed along the lower surface of the panels. For the future experiments, having a door for the WDS facility with proper sealing and also obtaining tabulated flow velocities measured experimentally, corresponding to the detailed incoming flow to be implemented in the CFD software and employed in the boundary conditions for the inlets flow description, could resolve such discrepancy and could allow for better and more precise numerical flow replication.

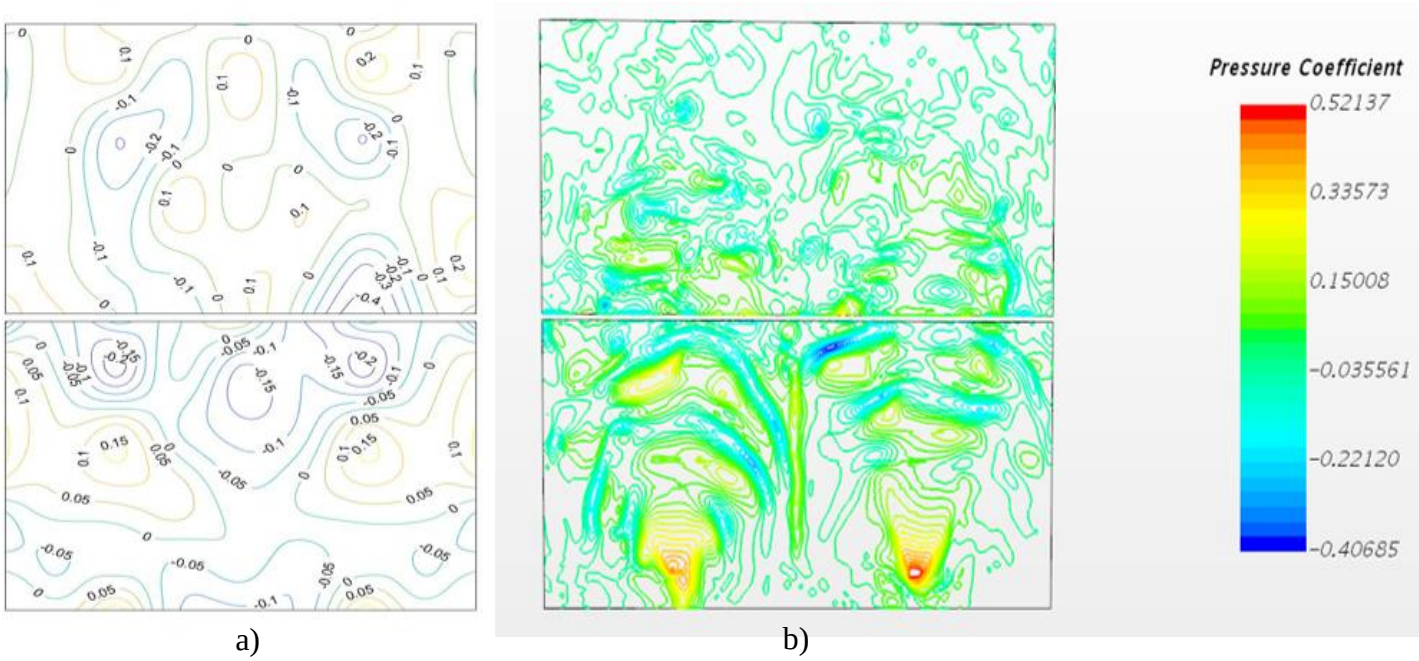

a) b)

Figure 5.8 Pressure coefficient (0° AOI) contours on the solar panels' upper surfaces: a) experimental results b) numerical (LES) results

5.5.2 Numerical velocity contours for 0° AOI

In addition to the high resolution, another advantage provided by the CFD numerical approach over the experimental one, is the ability to obtain flow characteristics at any point or location of the experimental facility. Visualizing the flow can help in understanding better the flow behavior and pressure coefficient distribution on the panel surface. As shown in Figure 5.8, the Cp fluctuations occurred after the wind flow encountered the first panel (bottom panel); a positive Cp on the upper surface of the panel took place, followed by an alternation of negative and positive Cp along the inlet-line. This alternation gradually ceased after passing the 20mm gap and reaching

the second panel. It was also noticed that positive Cp values along the mid-line of the first panel took place.

Similar pattern can be observed for the velocity contours of the inlet-plane, a vertical plane passing through the inlet-line, represented in Figure 5.9. The wind speed increased after the flow interacted with the panel surface, reaching a value of around 19.7 m/s, as shown in Figure 5.9. This wind speed increase diminished along the panel surface, beyond the 20mm gap between the panels. For the mid-plane, represented perpendicular to the panel at its middle location (Figure 5.10), wind speed started increasing near midway of the first panel; this is attributed to the wind flow from the inlets being redirected towards the middle of the panel due to the outlet suction location and wind flow redirection when hitting the first panel. Velocity reached was around 14.1 m/s near the 20mm gap, which can be similar to the WDS outlet suction effect, located right on top of the gap, since the employed wind speed condition was 14 m/s.

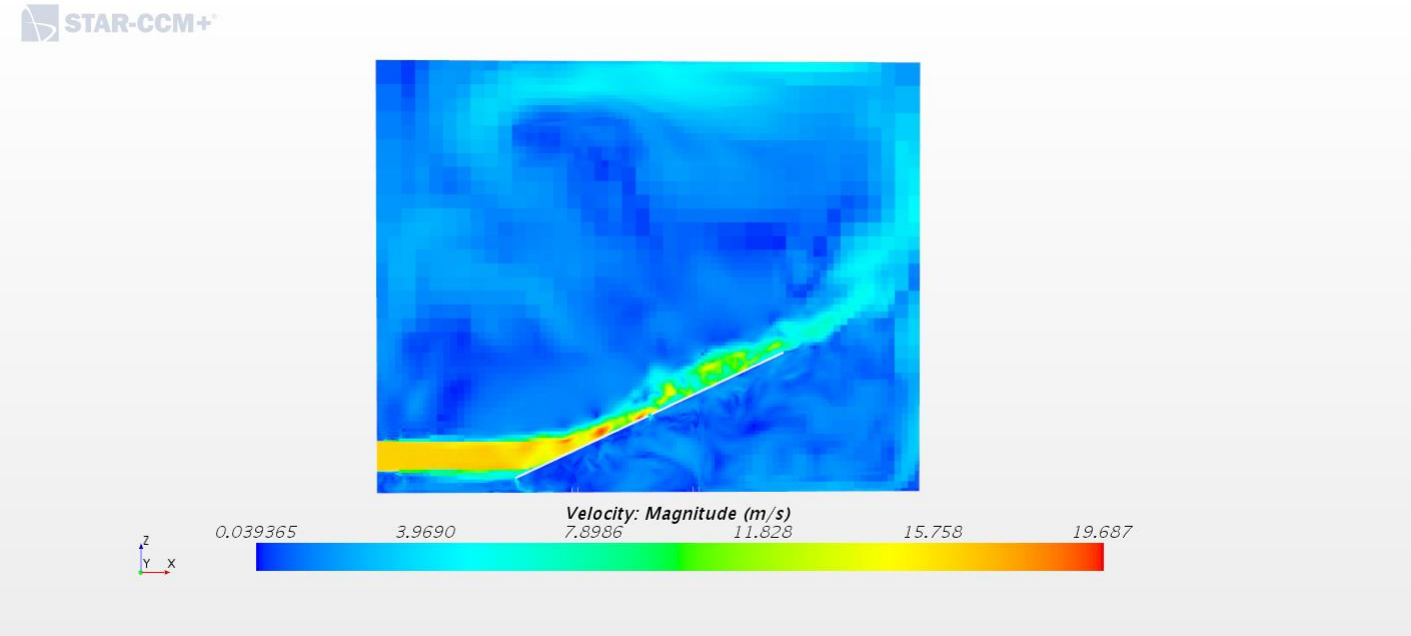

Figure 5.9 Velocity contours (inlet-plane, 0° AOI)

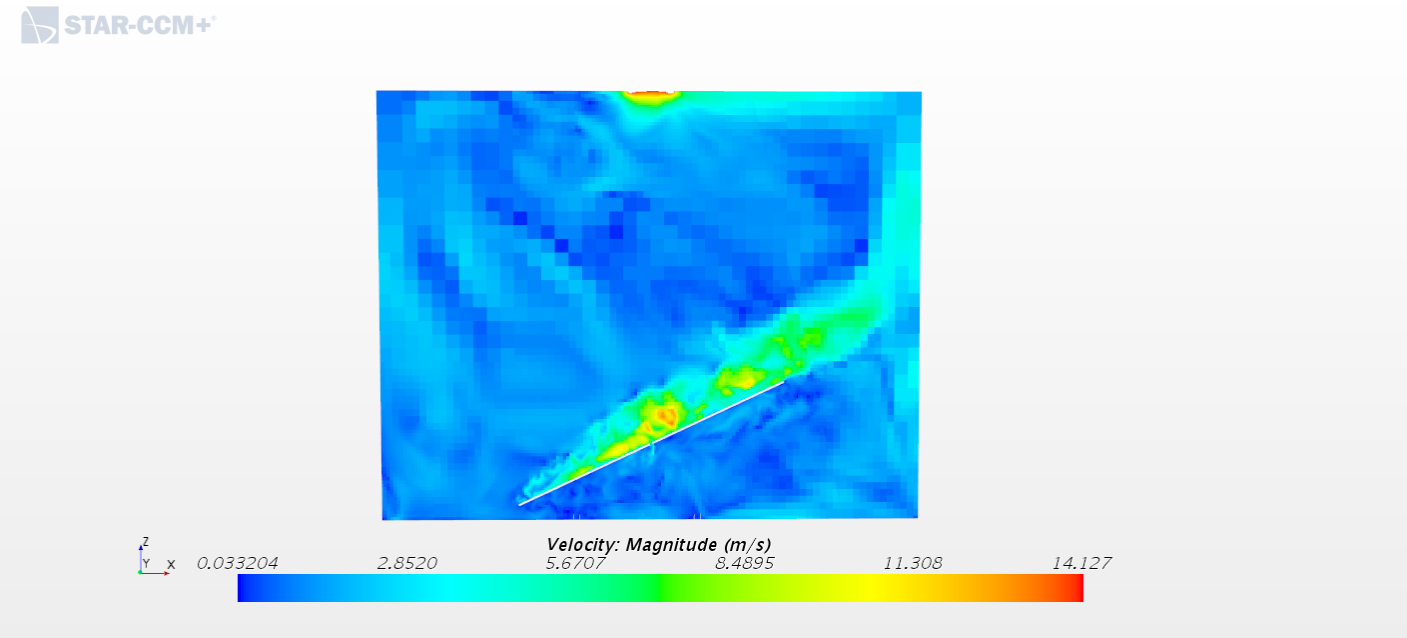

Figure 5.10 Velocity contours (mid-plane, 0° AOI)

5.5.3 Numerical velocity vector fields for 0° AOI

When the wind flow approached the panels, it resulted in an alternation of pressure coefficients ranging from negative to positive values. The vector representation of the wind velocity magnitude can help visualize the wind behavior that led to the Cp fluctuations along the upper surface of the panels. Figure 5.11 and Figure 5.12 represent the flow along the vertical plane section passing through the WDS inlet. As it can be observed, the flow entering the circular inlet follows a nearly uniform velocity of around 16.2 m/s near the center of the inlet. When approaching the surface of the panels, the wind flow is deflected upwards, downwards or around the surface. With the addition of the suction effect from the outlet, this led to creation of swirls, and an increased flow speed to around 19.7 m/s (higher velocity magnitude), which are more visible in Figure 5.12. These swirls are most significant before reaching the gap and near the surface of the first panel, while their effects diminish with the velocity along the second panel. The swirls (small vortices) presence justifies the presence of the signaled alternations of pressure coefficient distribution along the panel surface. The flow could have been influenced by the gap presence, the panel surfaces and the outlet suction effect caused by the blower, located at the center of the top wall above the gap.

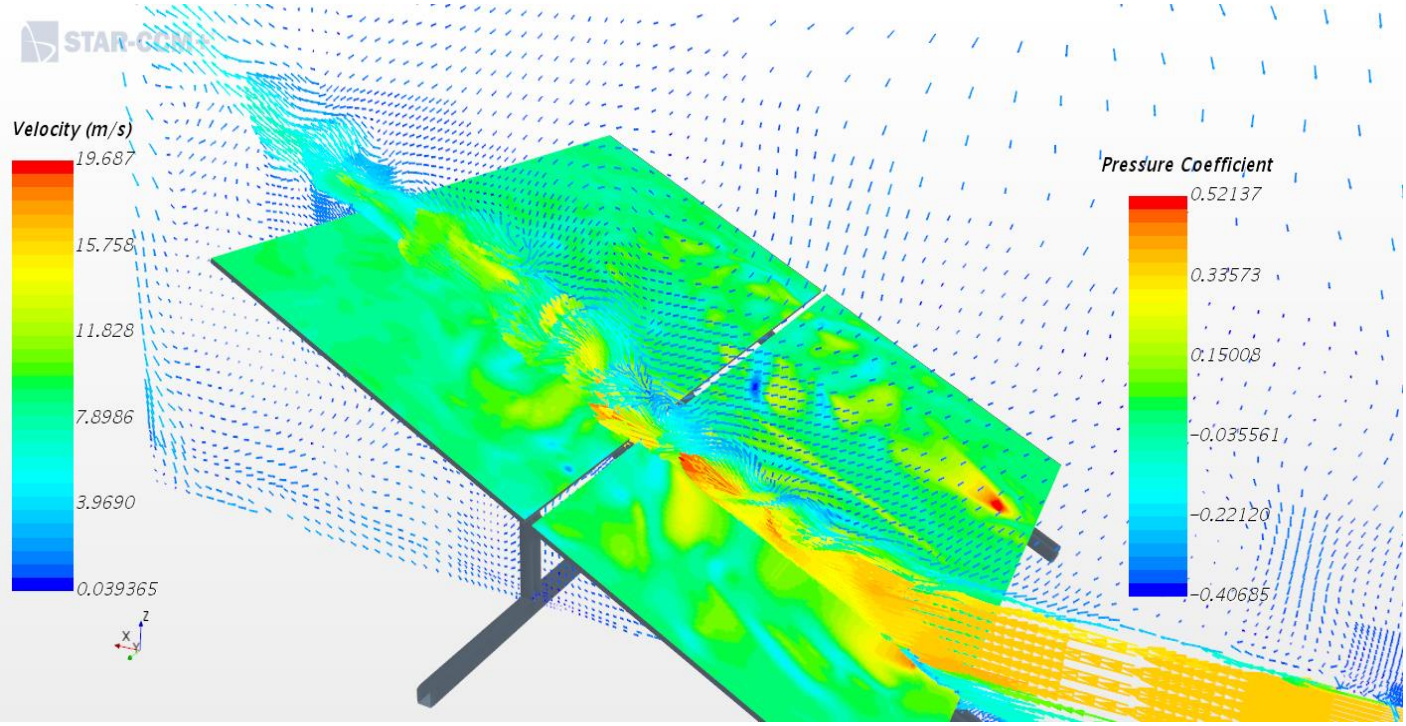

Figure 5.11 Velocity vector field (inlet-plane) with Cp contours on the panels' upper surfaces (0° AOI)

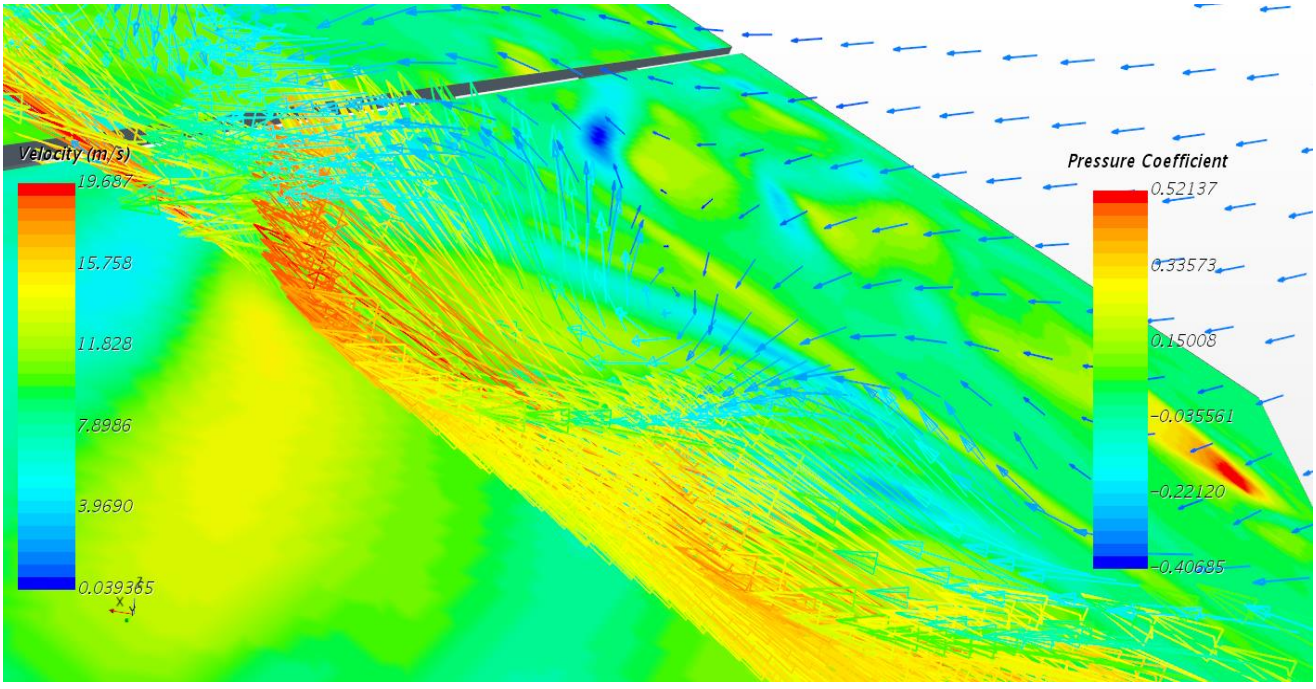

Figure 5.12 Close-up view of the velocity vector field (inlet-plane) with Cp contours on the panels' upper surfaces (0° AOI)

The velocity vector field along mid-line plane section is represented in Figure 5.13. No significant swirls are visible, and this explains the absence of Cp fluctuations and alternations between

positive and negative values along the mid-line of the panel. A possible cause for registering a positive pressure coefficient along the mid-line of the first panel is the detachment of wind flow from both inlets when hitting the panel, and the redirection of some flow streamlines towards the middle of the panel, where the suction outlet is located. This led to a deviation of the flow from the inlet-line path and formed a positive Cp along the mid-line. The only discrepancy between the numerical and experimental results is that the positive Cp values for the experimental results were registered along the mid-line of the second panel, whereas for the numerical results the positive Cp values can be observed on the first panel. Increasing wind speed occurred above the second panel after the flow passed the gap, reaching a magnitude of 14.1 m/s with the wind velocity vectors being directed upward.

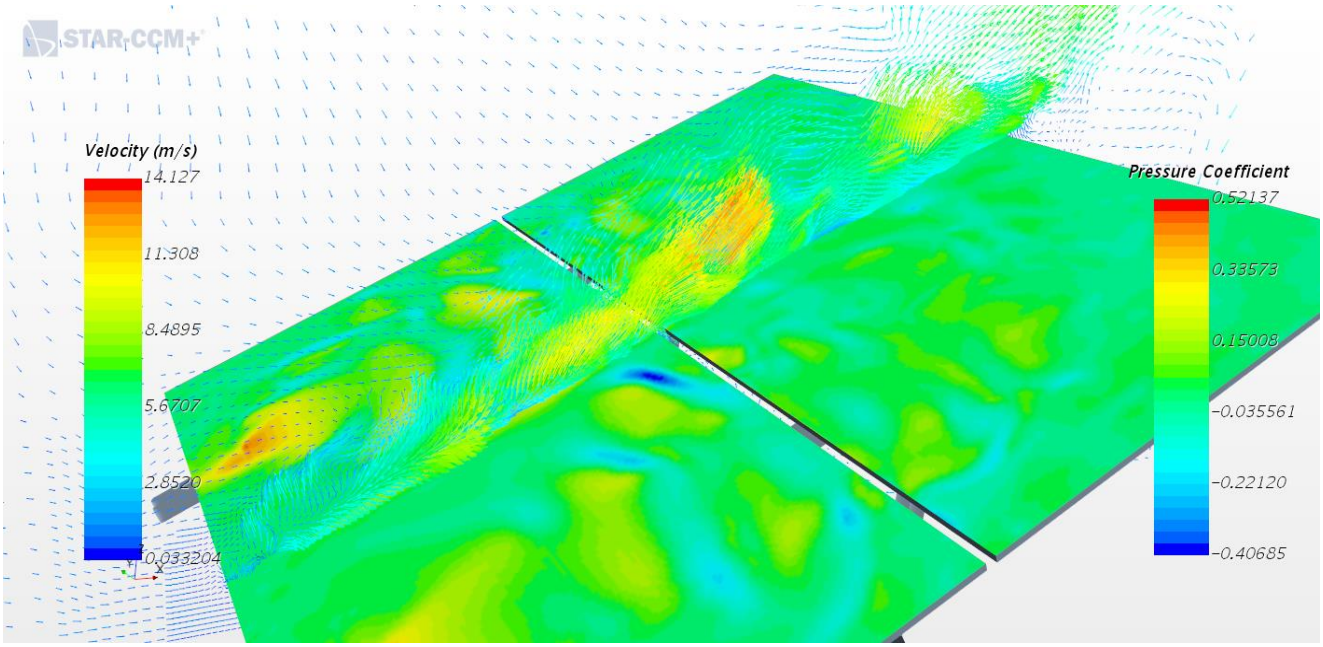

Figure 5.13 Velocity vector field (mid-plane) with Cp contours on the panels' upper surfaces (0° AOI)

5.6 Numerical results for LES for the solar panels at 180° AOI

5.6.1 Numerical Cp contours along the solar panels for 180° AOI

CFD simulation for the solar panels at 180° wind AOI case were conducted following the same methodology used for the 0° AOI case. The contours of the pressure coefficients along the surfaces of the panels were obtained for the 180° wind AOI case (Figure 5.14). The LES numerical results for the upper surface pressure coefficients were negligible, with no fluctuations and constant

magnitudes close to zero throughout the panels, except near the 20mm gap and some edges, as it can be seen in the graphs included in Appendix B. As mentioned previously, the air leakage in the experiment, due to lifting and displacing the WDS through often crane usage, or different flow suction mechanisms, could be the reason of such difference with the experimental results, where significant Cp distribution was noticed along the upper surface of the panels. For the lower surface of the panels, the numerical pressure coefficient contours showed a similar distribution when compared with the experimental results on the first panel. The lines facing the inlets were mostly subjected to positive Cp with the highest magnitude occurring midway of the upper half of the first panel, near the gap; also, negative pressure coefficients were observed near the side edges (Figure 5.14). Both the critical positive Cp and negative Cp were observed on the first panel upper half; however, the magnitudes were underestimated by the CFD simulation, for both positive and negative Cp. On the lower surface of the second panel, the numerical pressure coefficient magnitudes were negligible unlike the Cp values determined through the experiment. This could be attributed to problems encountered during the experiment, the experimental WDS flow having stronger suction; these can be avoided in the future with further flow studies and detailed wind profile to be defined for the flow in the WDS facility.

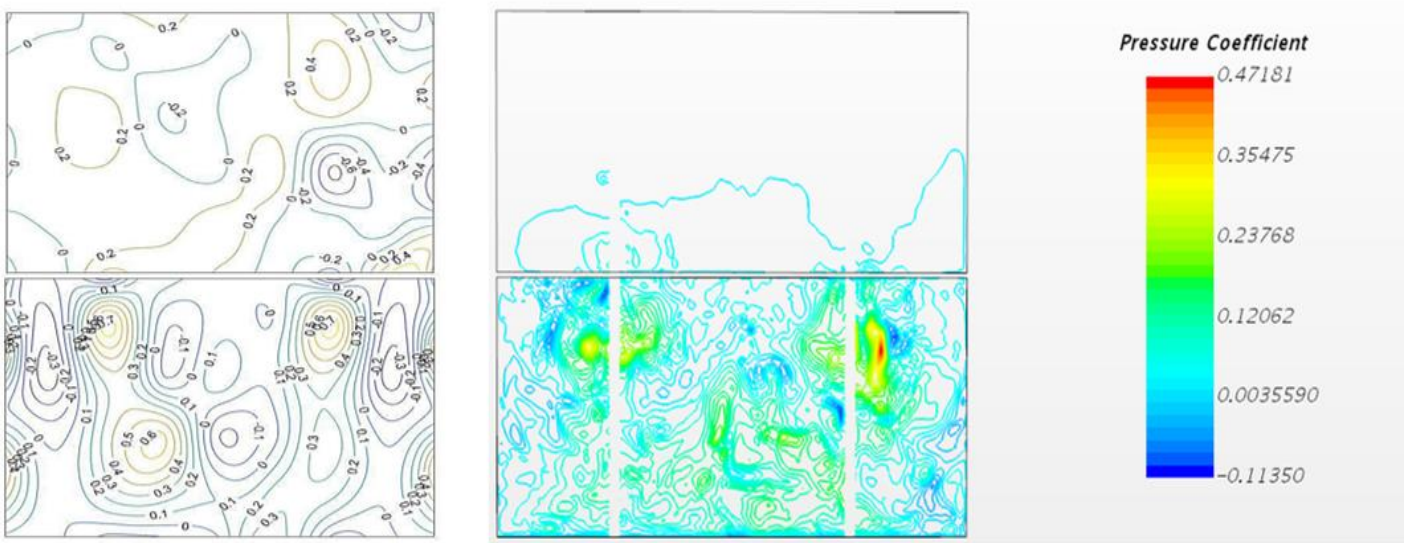

a) b)

Figure 5.14 Pressure coefficient (180° AOI) contours on the solar panels' lower surfaces: a) experimental results b) numerical (LES) results

5.6.2 Numerical velocity contours and vector fields for 180° AOI

The velocity contours and the vector fields along the plane section passing through the inlet and the panels were determined and were represented in Figure 5.15 and Figure 5.16, respectively. It can be observed that the further the moving wind flow was from the inlet, getting below the solar panels, the less uniform it became, where the velocity decreased on the circumference of the circle shaped flow. It is also noticed that flow velocity of around 17 m/s occurred when getting below the middle of the lower half of the second panel, prior to any interaction with the panel's surface (Figure 5.15). This can be attributed to the WDS outlet suction effect and the gap presence. After passing the gap, the flow velocity decreased along the panel distance, and small swirls formation could be noticed (Figure 5.16).

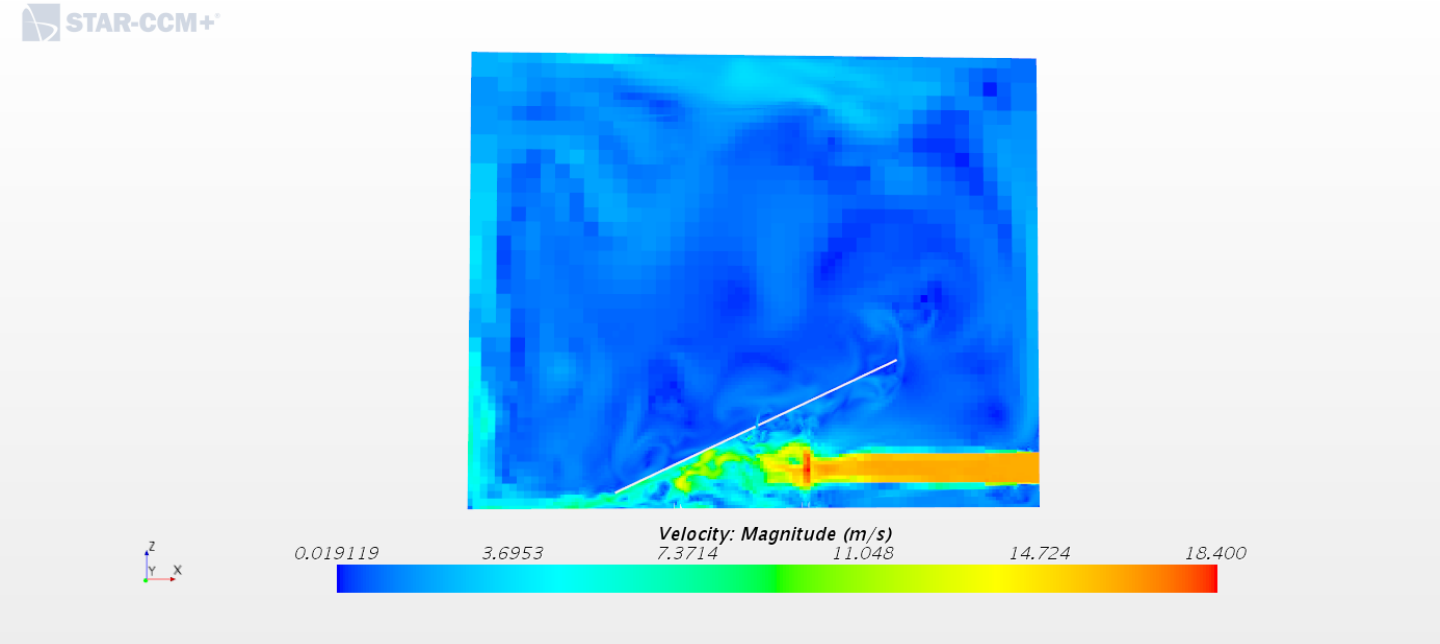

Figure 5.15 Velocity contours (inlet-plane, 180° AOI)

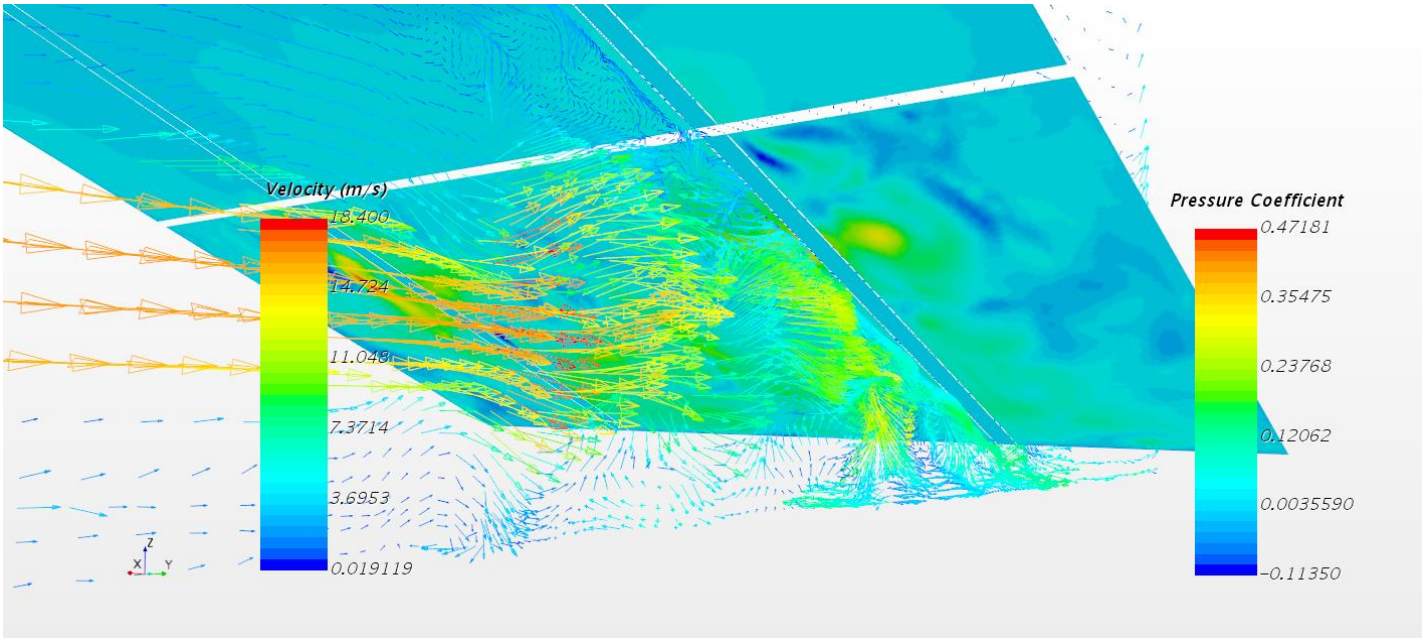

Figure 5.16 Velocity vector field (inlet-plane) with Cp contours on the panels' lower surfaces (180° AOI)

The velocity contours and vector field along the mid-panel section were determined and represented in Figure 5.17 and Figure 5.18, respectively. Flow incoming through the inlets begins to deviate slightly to the middle of the panel and an increase of wind speed was noticed near the 20mm gap. The mid-plane air velocity reached a maximum magnitude of around 11 m/s near the midway of the lower half of the first panel and decreased gradually due to the wind flow impinging on the panel surface and due to the interaction with the bottom floor of the WDS. The flow along the mid-plane section is fairly controlled with no significant swirls or vortices, which explains the absence of pressure coefficient fluctuations or sudden alternations between positive and negative values.

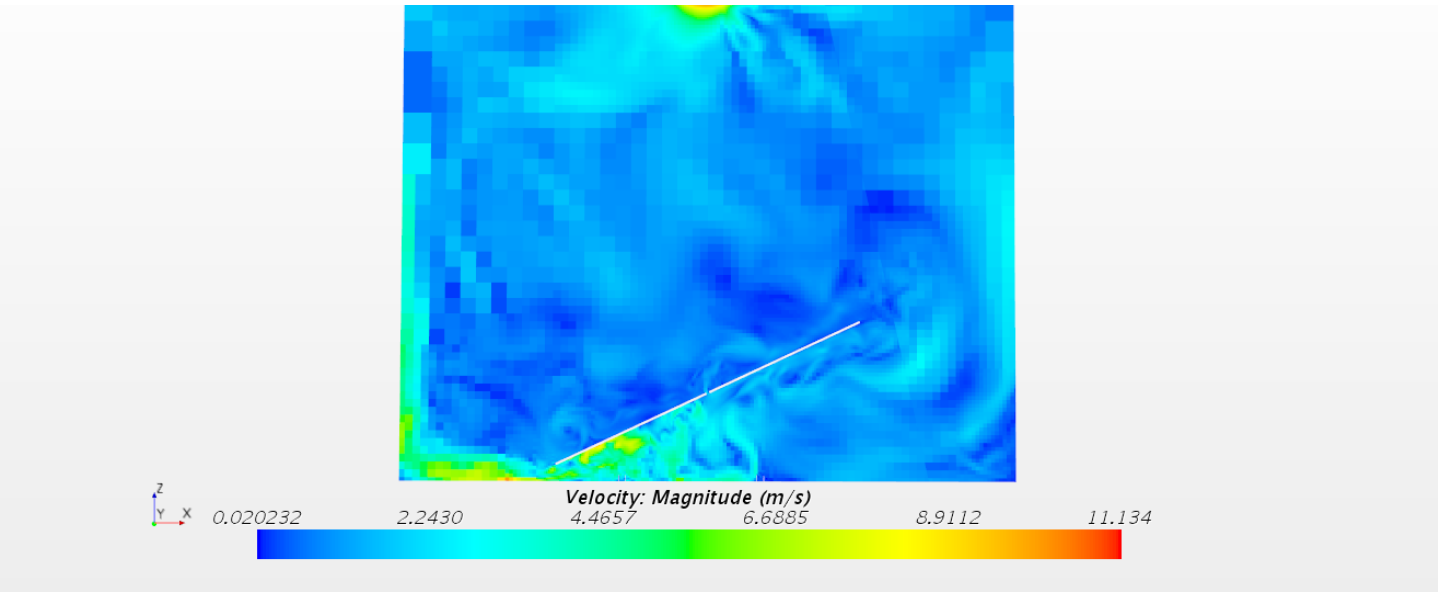

Figure 5.17 Velocity contours (mid-plane, 180° AOI)

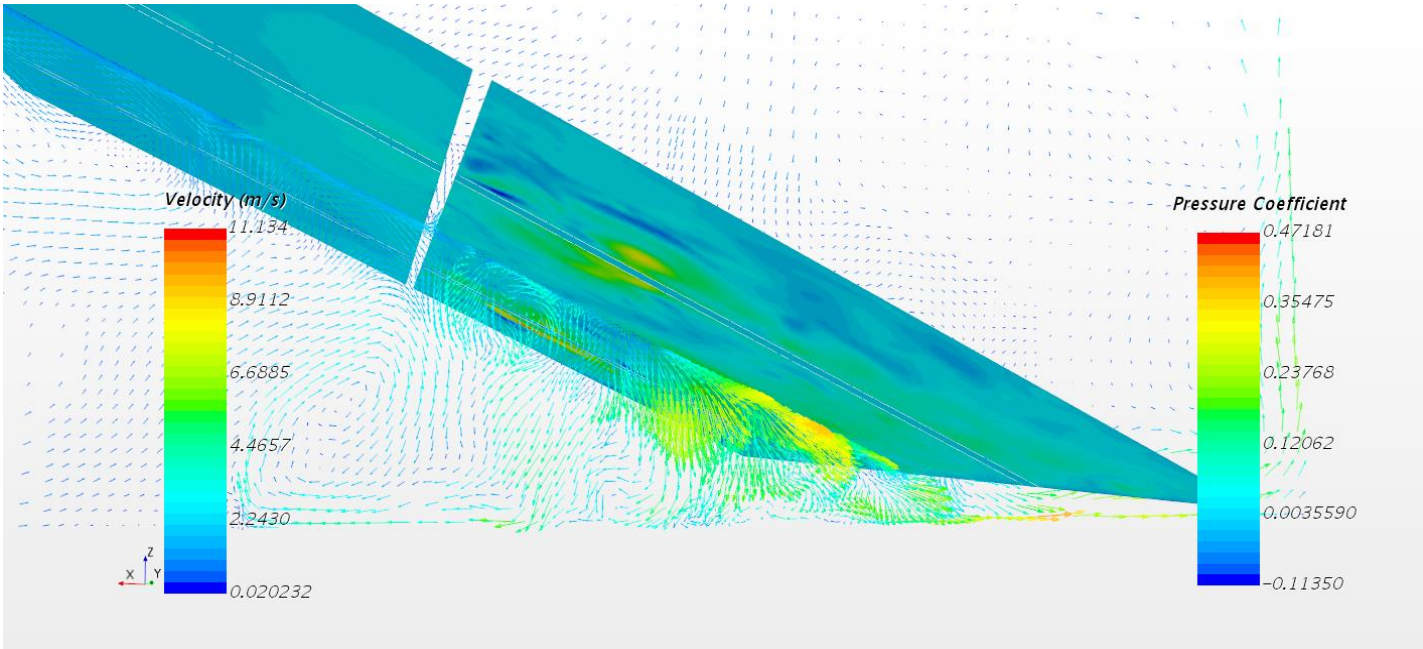

Figure 5.18 Velocity vector field (mid-plane) with Cp contours on the panels' lower surfaces (180° AOI)

In general, CFD results provided flow information and helped understanding the Cp fluctuations on the panels, along with identifying the locations on the panels where the wind speeds increased. However, the flow was not identical to the experimental WDS flow. And that could be observed when the Cp values on the lower surface of the panels and upper surface of the panels were negligible for the 0° and 180° AOI cases, respectively. A smaller mesh size, detailed flow profile

measured experimentally to be implemented in the CFD simulations, and further turbulence models examined could help resolve these discrepancies.

Chapter 6 Conclusions and Recommendations

6.1 Introduction

The new WDS experimental facility at the University of Ottawa was used to determine the wind-induced pressure coefficients distribution on full-scale solar panels with a 25° inclination angle. Different cases were considered in this study, for wind speeds between 14 m/s and 42 m/s, and wind angles of incidence between 0° and 225°. Results from 48 pressure taps installed on each surface of the panels were analyzed and the dimensionless pressure coefficients along the panel lines and surface contours were determined. A CFD study was also conducted to replicate the WDS experiment, for a better understanding of the flow-structure interaction, inside the WDS facility. Numerical results were obtained and were compared with the experimental values, to evaluate the selected CFD turbulence model, in relation to the WDS facility wind flow. Detailed flow behavior was obtained through the CFD simulations, which provided better visualization and understanding of the pressure coefficient distribution on the surfaces of the examined solar panels.

6.2 Conclusions

Six wind angles of incidence, 0°, 30°, 45°, 180°, 210°, and 225° were considered in the experiments, each tested for different wind speeds ranging from 14 m/s to 42 m/s, with approximately 2 m/s increments. Pressure measurements were obtained on the upper surface and lower surface of the panels, and the net pressure was calculated. Pressure coefficient results were determined and were analyzed for better comparison, as detailed in Chapter 4. Contours representing the pressure coefficient distribution along the tested model were determined and discussed for all the six wind angles of incidence.

The 0° and 180° wind AOI cases were found to be the most critical cases, where the tested solar panels registered the highest magnitudes of net equivalent pressure coefficient, also known as the area-averaged pressure coefficient. The critical AOI that induced the highest equivalent pressure coefficient, Cp_{eq} was found to be the 180° wind AOI, when the wind flow from the inlets is approaching the panels from behind, followed by the 0° wind AOI case, when the incoming flow

is approaching the panels from the front. Similarly, Samani (2016) concluded that the 180° AOI case induced the highest critical equivalent pressure coefficient on the panels. For the 0° wind AOI case of the present study, the wind-induced equivalent net pressure coefficient was greater in uplift (negative Cp_{eq}) on the second panel than on the first panel, for most of the wind speeds examined. The 0° wind AOI case conducted in the WDS facility led to negative (uplift) Cp results, due to the WDS flow being controlled by the suction through the top outlet, which forced the wind flow from the lateral inlets, to be redirected upwards, away from the panel surface after contact. Regarding the 180° wind AOI case, the net equivalent pressure coefficient on the first panel (lower panel) was significantly higher in uplift magnitude (negative Cp) than the net equivalent pressure coefficient on the second panel for most cases. This difference of values between the first panel and the second panel can be attributed to wind flow hitting the first panel's lower surface, then getting deflected and passing below the panel, and ultimately reaching the outlet. The higher wind speeds led to an increase in uplift (negative) Cp_{eq} on the second panel and that can be attributed to the outlet, located at the center of the WDS ceiling, having stronger suction effect for higher selected wind speeds (higher industrial blower rpm settings) on the wind flow. The Cp_{eq} of the present study on the panels are shown in Table 6.1 for the different wind AOI at 14-15 m/s. The previous study conducted by Samani (2016) resulted in a decrease of Cp_{eq} when the wind AOI increased from 0° to 45°, whereas for the present study, the Cp_{eq} increased, reaching the highest positive value at a wind AOI of 45°, as can be seen in Table 6.1. The differences between the two facilities are that the WDS simulates a suction oriented flow, due to the outlet effect, when compared to the flow generated by the wind tunnel. Also, the magnitude of the pressure coefficients obtained in the wind tunnel were higher than the ones measured in the WDS, since the tested model was fully submerged in the wind flow. From the present study, it can be noticed that the first panel was subjected to a small negative Cp_{eq} (suction) which increased to positive when the panel was turned with regard to the wind direction, until reaching 180° wind AOI, where the Cp_{eq} decreased and the highest suction magnitude was registered for the first panel. For the second panel, the Cp_{eq} had the highest suction value at 0° wind AOI and decreased in magnitude while remaining negative for the other wind directions. The Cp_{eq} was found to be significantly higher in magnitude for the first panel than the second panel for 45° and 180° AOI, whereas the opposite was observed for the 0° and 210° AOI.

Table 6.1 Experimental Cp_{eq} on the panels for different wind AOI (present study)

AOI case	Panel 1 Cp_{eq}	Panel 2 Cp_{eq}	Total Cp_{eq}
0°	-0.021	-0.19	-0.106
30°	0.081	-0.072	0.0045
45°	0.18	-0.011	0.085
180°	-0.29	-0.024	-0.16
210°	-0.022	-0.12	-0.071
225°	-0.11	-0.081	-0.096

For the 0° wind AOI case, the wind speeds affected the pressure coefficient distribution on the solar panels. The lower wind speeds range, below 23 m/s resulted in a positive pressure coefficient on the upper surface inlet-line of the first panel, alternating positive to negative magnitudes along the second panel, whereas with higher wind speeds, above 23 m/s, negative Cp values were observed along the inlet-lines of both panels. On the upper surface, uplift (negative Cp) took place as the flow approached the 20mm gap between the panels, for all wind speeds. For low wind speeds, positive Cp was formed on the second panel mid-line, signifying that the air was diverted to the middle (outlet location) after interacting with the panels, whereas for higher wind speeds the panels underwent stronger suction; positive Cp values were noticed on the mid-line of the first panel. Similar distribution was observed for the lower surfaces of the panels, the only difference being the magnitudes of the Cp coefficients, which could be attributed to the higher blower rpm leading to stronger upward suction exerted on wind flow post interaction with the panels.

For the 180° wind AOI case, it was concluded that the first panel was subjected mostly to uplift (negative Cp) with the most critical value occurring on the upper half of the inlet-line, near the 20mm gap, for all the wind speeds. Along the first panel, a positive net pressure coefficient was noticed halfway of the mid-line for low wind speeds, below 23 m/s, whereas the Cp remained negative for the higher wind speeds. Between the inlet-line and the edge-line, low wind speeds led to an alternation of negative to positive Cp_{net}, whereas for higher wind speeds, the negative Cp_{net} which was noticed on the inlet-line, diminished in value, however did not switch to positive region. Along the edge-line, alternation of the net Cp is observed for most wind speeds, while staying in

the negative (uplift) range, with the 20mm gap producing an effect on the Cp results by reducing the magnitude of the uplift and bringing it close to null, only to alternate and increase in negative magnitudes along the second panel. Similar effect was observed for most wind speeds on the inlet-line. Along the second panel mid-line, for the high wind speeds, above 23 m/s, the net pressure coefficients were mostly negative, whereas for the lower speeds, positive pressure coefficients were noticed on the upper half of the mid-line, near the centre of the second panel.

For the 0° and 180° wind AOI cases, comparisons of the mean Cp results along the mid-line and inlet-line were conducted with the mean Cp along the mid-line of the previous study carried out by Samani (2016) on similar solar panels model configurations. Discrepancies between the Cp distributions and magnitudes were noticed when comparing with Samani (2016), which were due to the different characteristics of the wind flow simulated by the two facilities, the WDS in the present study and the WindEEE in the previous study. For the 0° wind AOI case, the net pressure coefficient contours obtained in the present study, contained negative values (uplift), unlike the results of the experiment conducted by Samani (2016), which reported only positive Cp_{net} values. That could be due to the fact that, as designed in the WDS facility, the flow suction is more dominant. The WDS outlet opening, located at the middle of the top ceiling of the WDS, directs the wind flow upwards through its connection to the blower. The 20mm gap between the panels had a similar effect on the pressure coefficient distribution along the inlet-line for the 180° wind AOI case, where an abrupt change took place. The gap effect on the Cp values was more noticeable for the results along the inlet-line than for the mid-line.

Computational Fluid Dynamics (CFD) analysis was conducted to numerically evaluate the wind pressure coefficient on the panels, using STAR-CCM+ software. The 0° and 180° wind AOI cases were examined, as these were found to be the two critical cases when the analysis of the experimental results was performed. The three-dimensional domain of the simulation and the modelling results were determined and represented in Chapter 5. Due to the fact that the flow in the WDS facility is unstable and turbulent, the three-dimensional RANS model was employed to determine the initial conditions to be used by the unsteady LES turbulence model.

For the 0° wind AOI case, it was observed that the RANS turbulence model did not replicate the experimental conditions well and underestimated the negative Cp values, whereas LES model resulted in better flow replication; fluctuations were noticed in the pressure coefficient contours

on the panels' upper surfaces. From the pressure coefficients contours, it was observed that the WDS flow was more dispersed in the experiment, when compared with the CFD numerical simulation, particularly at the wind-panel contact point, where the CFD resulted in an overestimated positive Cp value. The pressure taps resolution could have played a significant role in this discrepancy, along with the wind dispersion being stronger in the experiment, when compared to the CFD simulation. However, Cp fluctuations were observed similar to those obtained through the experimental results. The wind velocity vectors indicated the swirls formations and an increase of wind speed after the wind flow impacted the first panel, causing an alternation of Cp on the upper surface along the inlet-line. The wind flow velocity magnitude and the swirls effect were most critical on the first panel inlet-line near the 20mm gap, only to diminish with the flow velocity along the second panel after passing the gap. This swirls presence passing along the upper surface of the panels explains the Cp alternations between positive and negative values, which could have been created by the gap presence, the panels surface-wind interaction and the effect of the outlet suction, located at the center of the WDS top ceiling above the gap. Along the mid-line, no significant swirls formation or Cp fluctuations were noticed. For the CFD simulation, positive Cp were observed on the first panel mid-line, unlike the experimental results where the positive Cp values were observed along the second panel mid-line. This could be caused by the suction outlet, located at the middle of the WDS top ceiling, causing the detachment of wind flow incoming from both of the inlets when encountering the first panel and the redirection of streamlines towards the middle of the panel. Increased wind flow velocity occurred, reaching the highest speed near the 20mm gap location (below the outlet) and followed by a diminishing trend afterwards. Also, for the CFD numerical simulations, the pressure coefficients on the lower surfaces, registered negligible magnitudes, with little to no variation, except for the region near the 20mm gap and edges; this can be due to air leakage in the real WDS experimental chamber or due to several other factors that are mentioned in the research limitations below.

For the numerical 180° wind AOI case, the CFD simulation showed that the wind speed increased along the inlet-plane section, below halfway of the second panel prior to any contact with the surface, which can be attributed to the WDS outlet suction effect and the gap presence. After passing the gap, the flow velocity magnitude decreased along the panel distance. Flow coming through the inlets begins to deviate slightly to the middle after passing the 20mm gap. The wind velocity along the mid-plane section reached a maximum magnitude around midway of the lower

half of the first panel and decreased gradually with no significant swirl formation. Along the lower surface of the panels, it was found that the first panel underwent the critical Cp in positive and negative magnitudes, whereas the lower surface of the second panel had negligible pressure coefficient distribution, unlike what was observed through the experimental results. Positive Cp was observed on the first panel along the line facing the inlets, similarly to the experimental results, with the highest value occurring on the upper half near the gap with negative pressure on the sides. After the wind flow was deflected due to contact with the first panel surface, the numerical simulation induced positive Cp along the mid-line lower half of the first panel, whereas the experimental results had negative Cp values. The numerical Cp distribution on the second panel showed some discrepancy with the experimental results, which could be attributed to the limitations in the experimental conditions, the WDS experimental flow experiencing stronger dispersion, and this emphasizes on the importance of further flow studies, CFD investigations and detailed wind profile to be defined for the WDS flow. Along the upper surfaces of the panels, similarly to the panels' lower surfaces of the 0° wind AOI case, the numerical Cp distribution was negligible which can be attributed to the same reasons as mentioned previously.

In general, it was concluded that the flow in the WDS facility is more of an uplift, upward-suction based flow, and the results were different from the previous wind tunnel study. This new facility could be used to test panels capacity and failures of the connections under high unsteady wind speeds.

6.3 Research limitations

It is important to mention several research limitations noticed in the current study, whether they were caused by technical difficulties or uncontrollable events. The WDS facility is still newly acquired, hence it is expectable to undergo certain errors at the beginning of the testing procedures. One of these limitations is the crane usage whenever access to the module is needed, due to the absence of a door or a turntable. Lifting and placing the WDS entire structure could affect the experimental conditions, considering the absence of threads to properly seal the unused inlets along with the uneven seal around the perimeter in contact with the floor, since air leakage could take place altering the flow. This restriction also has limited the number of cases to be tested, along

with the time-constraint events; such as the WDS facility moving deadline to an allocated new building, and the University of Ottawa laboratory two-week shutdown caused by an unfortunate accident in the lab.

6.4 Recommendations for future research

Regarding future research recommendations, a turntable would be essential to be placed inside the WDS facility, which will allow to change the wind AOI to test several cases without influencing the flow conditions. A door can be added to the WDS, which will reduce the usage of cranes limiting the potential air leaks. More taps can be used for the pressure measurements on the surfaces of the solar panels, which will provide better accuracy and more information regarding the wind-induced effects. Calibration of the WDS facility can be conducted and different panels' scales can be examined to help understand the scale effect and to determine correction factors for the pressure coefficient results. To achieve the full potential of the WDS facility, it is recommended to conduct further studies on the generated flow characteristics. The influence of opening opposite and oblique inlets on the generated wind flow and their effects on the created turbulence could be studied to broaden the WDS role in the research industry. Defining the WDS inlets flow in CFD by tabulated wind speed values measured through the experiment could help avoid discrepancies in the numerical results. Moreover, the CFD simulations can be carried out with a much finer grid and a smaller time step to enhance the accuracy and performance of the numerical replication of the experiment. In addition, it is recommended to examine different models such as DES turbulence model or WALE subgrid scale turbulence model, along with different meshing techniques and solvers to obtain a more accurate description of the most appropriate CFD methodology to follow for the new WDS facility. Finally, modelling the blower part included in the geometric domain could allow for better accuracy; however, this could significantly increase the computational cost of the simulation. Hence, future studies are recommended to be conducted modelling the effects of the blower connected to the WDS outlet.

References

Abiola-Ogedengbe, A. (2013). Experimental investigation of wind effect on solar panels. Thesis and Dissertation Repository, University of Western Ontario.

Abiola-Ogedengbe, A., Hangan, H., Siddiqui, K. (2015). Experimental investigation of wind effects on a standalone photovoltaic (PV) module. Renewable Energy, 78, 657-665.

Aly, A. M., Bitsuamlak, G. (2013). Aerodynamics of ground-mounted solar panels: test model scale effects. Journal of Wind Engineering and Industrial Aerodynamics. 123, 250-260.

Aly, A. M., Bitsuamlak, G. (2014). Aerodynamic loads on ground-mounted solar panels: multi scale computational and experimental investigations. Advances in Civil, Environmental, and Materials Research (ACEM14).

Aly, A.M., Bresowar, J. (2016). Aerodynamic mitigation of wind-induced uplift forces on low-rise buildings: A comparative study. Journal of Building Engineering, 5, 267-276.

Anderson, J. (1995). Computational Fluid Dynamics: The basics with applications. New York, NY: McGraw-Hill, Inc.

ASCE 49-12. (2012). Wind Tunnel Testing for Buildings and Other Structures. American Society of Civil Engineers.

ASCE 7-16. (2016). Minimum Design Loads and Associated Criteria for Buildings and Other Structures. American Society of Civil Engineers.

Banks, D. (2012). How Wind Load Studies Will Impact The Solar Industry. WREF proceedings.

Bitsuamlak, G., Dagnew, A., Erwin, J. (2010). Evaluation of wind loads on solar panel modules using CFD. The Fifth International Symposium on Computational Wind Engineering (CWE2010).

Cain, J.H., Banks, D. (2015). Wind Loads on Utility Scale Solar PV Power Plants. 2015 SEAOC Convention

Cain, J.H., Banks, D. (2016). Wind Loads on Utility Scale Solar PV Power Plants. 2016 SEAOC Convention

Casey, M., & Wintergerste, T. (2000). Best Practice Guidelines, ERCOFTAC Special Interest Group on Quality and Trust in Industrial CFD. ERCOFTAC.

Franke, J., Hellsten, A., Schlünzen, H., & Carissimo, B. (2007). Best Practice Guideline for the CFD Simulation of Flows in the Urban Environment. COST 732: Quality Assurance and Improvement of Microscale Meteorological Models. COST Office Brussels, ISBN 3-00-018312-4.

Germano, M., Piomelli, U., Moin, P. and Cabot, W. H. (1991), "A Dynamic Subgrid-Scale Eddy Viscosity Model", Physics of Fluids A, Vol. 3, No. 7, pp. 1760-1765.

Holmes, J. D. (2015). Wind loading of structures. CRC Press.

IESO. (2019a). microFIT Program. Independent Electricity System Operator. Retrieved from: http://www.ieso.ca/en/get-involved/microfit/news-overview.

IESO. (2019b). Feed-in Tariff Program. Independent Electricity System Operator. Retrieved from: http://www.ieso.ca/Sector-Participants/Feed-in-Tariff-Program/Overview.

IPCC. (2011). Intergovernmental Panel on Climate Change (IPCC) Special Report on Renewable Energy Sources and Climate Change Mitigation. Prepared by Working Group III of the IPCC [O. Edenhofer, R. Pichs-Madruga, Y. Sokona, K. Seyboth, P. Matschoss, S. Kadner, T. Zwickel, P. Eickemeier, G. Hansen, S. Schlömer, C. von Stechow (eds)]. Cambridge University Press, Cambridge, United Kingdom and New York, NY, USA, 1075 pp. (Chapter 9).

Jubayer, C.M., Hangan, H. (2014). Numerical simulation of wind effects on a stand-alone ground mounted photovoltaic (PV) system. Journal of Wind Engineering and Industrial Aerodynamics. 134, 56-64.

Jubayer, C.M., Hangan, H. (2016). A numerical approach to the investigation of wind loading on an array of ground mounted solar photovoltaic (PV) panels. Journal of Wind Engineering and Industrial Aerodynamics. 153, 60-70

Kim, D. (2013). The application of CFD to building analysis and design: a combined approach of an immersive case study and wind tunnel testing. Virginia Polytechnic Institute and State University.

Kopp, G.A., Surry, D. and Chen, K. (2002), “Wind loads on a solar array,” Wind Struct., 5(5), 393-406.

Mehta, C.K., Coulbourne, L.W. (2013). *Guide to the Wind Load Provisions of ASCE 7-10.* American Society Of Civil Engineers.

Menter,F.R. (1994).Two-equation eddy-viscosity turbulence model for engineering applications. Am.Inst.Aeronaut.Astronaut.J.32,1598–1605.

Müllenbach, P., Deutenbach, K.R. (1991). Determination of dynamic pressure and reference pressure in automobile wind tunnels with open test section. Journal of Wind Engineering and Industrial Aerodynamics, 38, 11-22.

NBC. (2015). National Building Code of Canada. Canadian Commission on Building and Fire Codes. National Research Council Canada.

Nkemdirim, L.C. (2006). Wind. In the Canadian Encyclopedia. Retrieved from: http://www.the canadianencylopedia.ca/en/article/wind/

NRCan. (2017). About Renewable Energy. National Resource Canada Retrieved from: https://www. nrcan.gc.ca/energy/renewable-electricity/7295.

Ontario Ministry. (2019). Renewable energy development in Ontario: A guide for municipalities, Feed-in tariff program. Retrieved from: https://www.ontario.ca/document/renewable-energy-development-ontario-guide-municipalities/40-feed-tariff-program

PV2-(2012). Wind Design for Low-Profile Solar Photovoltaic Arrays on Building Roofs. SEAOC. Structural Engineers Association of California.

PV2-(2017). Wind Design for Solar Arrays. SEAOC. Structural Engineers Association of California.

Reina, G. P., De Stefano, G. (2017). A CFD Study of Wind Loads on High Aspect Ratio Ground-Mounted Solar Panels. Computational Science and Its Applications-ICCSA 2017, Part I, LNCS 10404, pp. 261–272, 2017

Samani, Z. (2016). Wind Loading on Full-scale Solar Panels. Electronic Thesis and Dissertation Repository. 3529. University of Western Ontario. Retrieved from: https://ir.lib.uwo.ca/etd/3529

Shademan, M., Barron, R. M., Balachandar, R., Hangan, H. (2014). Numerical simulation of wind loading on ground-mounted solar panels at different flow configurations. Canadian Journal of Civil Engineering 41, 728-738.

Structural Commentaries. (2015). User's Guide-NBC 2015 Part 4 Division B. National Research Council Canada. Canadian Commission on Building and Fire Codes.

Tieleman, H. W. (1990). Wind tunnel simulation of the turbulence in the surface layer. Journal of Wind Engineering and Industrial Aerodynamics, 36, 1309-1318.

Tominaga, Y., Mochida, A., Yoshie, R., Kataoka, H., Nozu, T., Yoshikawa, M. and Shirasawa, T., (2008), "AIJ guidelines for practical application of CFD to pedestrian wind environment around buildings," Journal of Wind Engineering and Industrial Aerodynamics, 96, 1749-1761.

Van Leer, B. (1979), Towards the Ultimate Conservative Difference Scheme, V. A Second Order Sequel to Godunov's Method, J. Com. Phys.., 32, 101–136.

Yang, Y., Gu, M., Jin, X. (2009). New inflow boundary conditions for modeling the neutral equilibrium atmospheric boundary layer in SST k-w model. In proceedings of the Seventh Asia Pacific Conference on Wind Engineering. APCWE-VII

Zhou, Y., Kareem, A. (2002). Definition of wind profiles in ASCE 7. Journal of Structural Engineering, 128(8), 1082-1086.

Appendix A

Cp along panels' upper surface mid-line

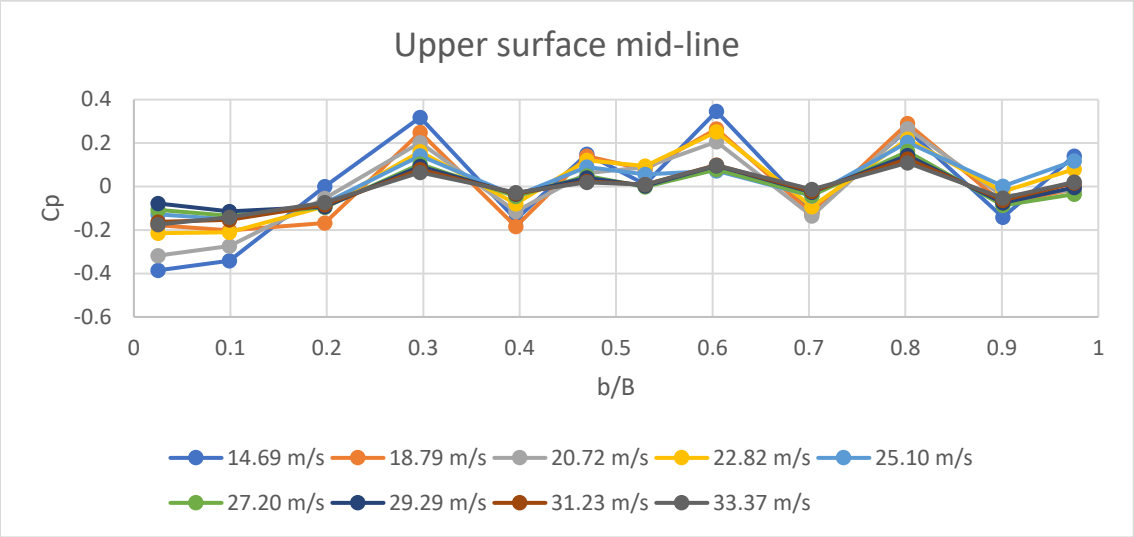

Figure A.1 Cp variation along the upper surface mid-line (wind speed range 1, 180° AOI)

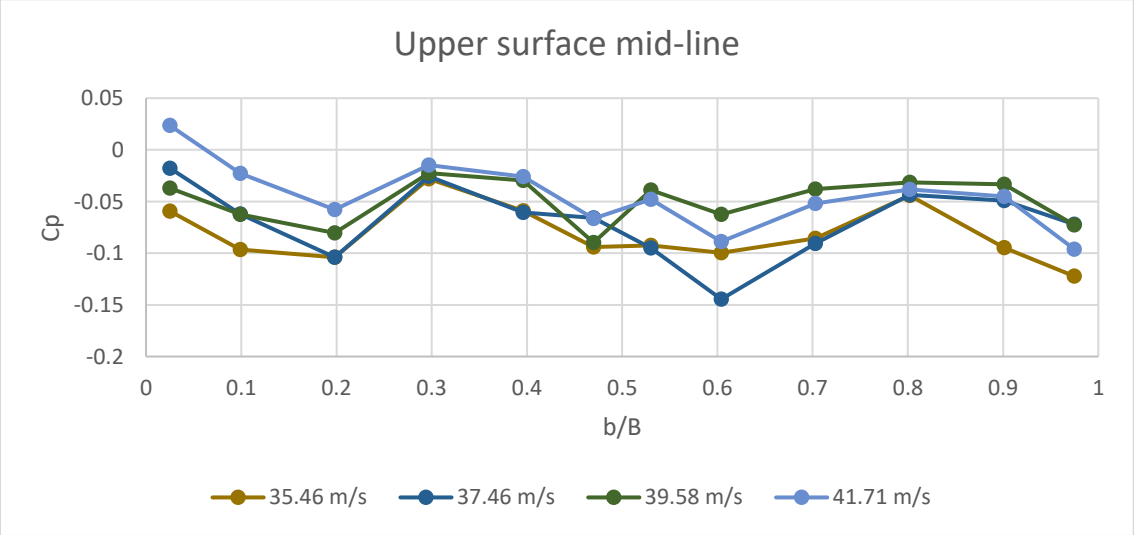

Figure A.2 Cp variation along the upper surface mid-line (wind speed range 2, 180° AOI)

Cp along panels' lower surface mid-line

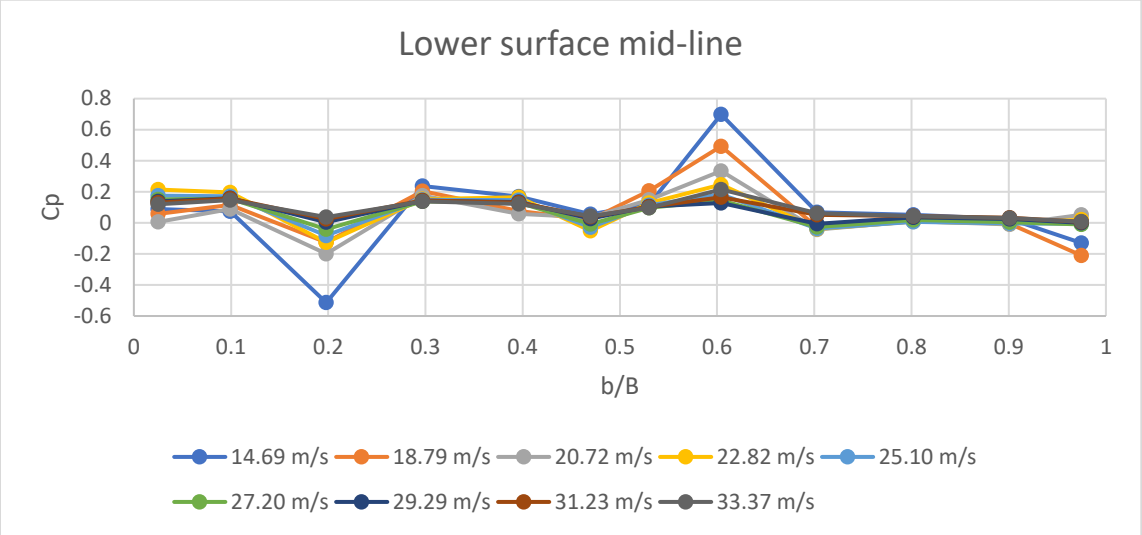

Figure A.3 Cp variation along the lower surface mid-line (wind speed range 1, 180° AOI)

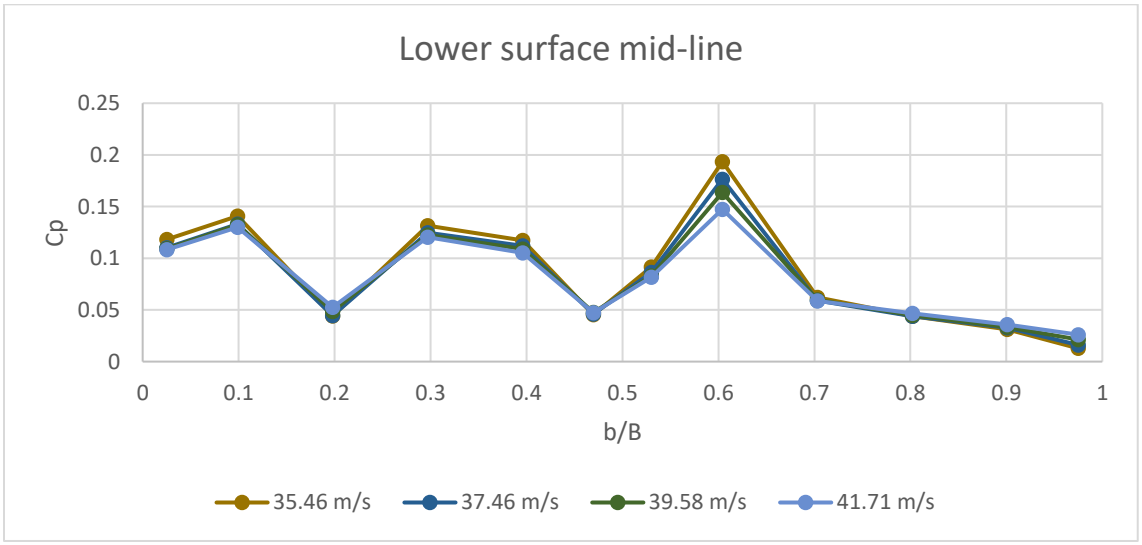

Figure A.4 Cp variation along the lower surface mid-line (wind speed range 2, 180° AOI)

Cp along panels' upper surface inlet-line

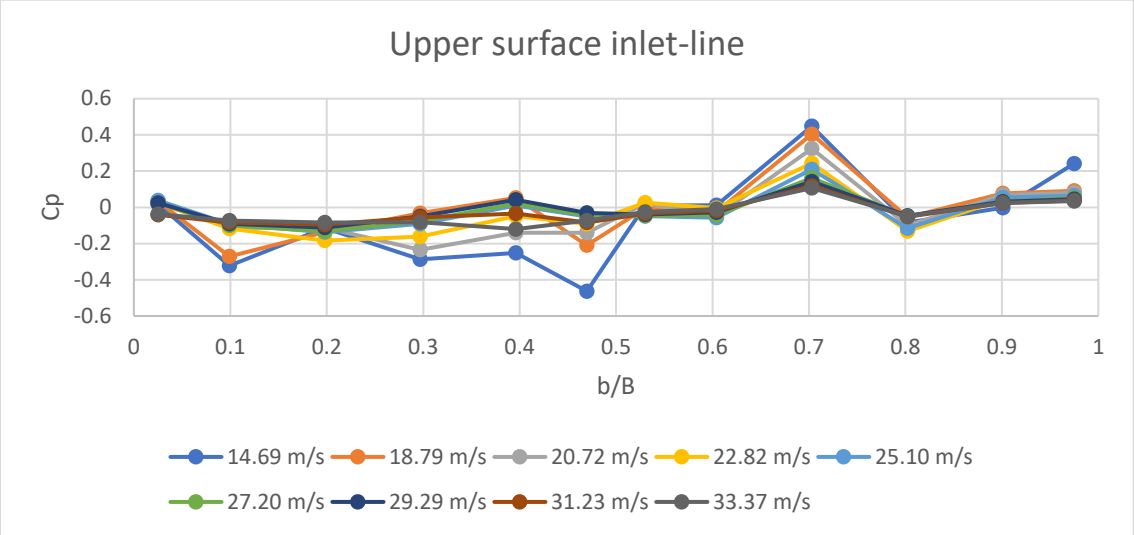

Figure A.5 Cp variation along the upper surface inlet-line (wind speed range 1, 180° AOI)

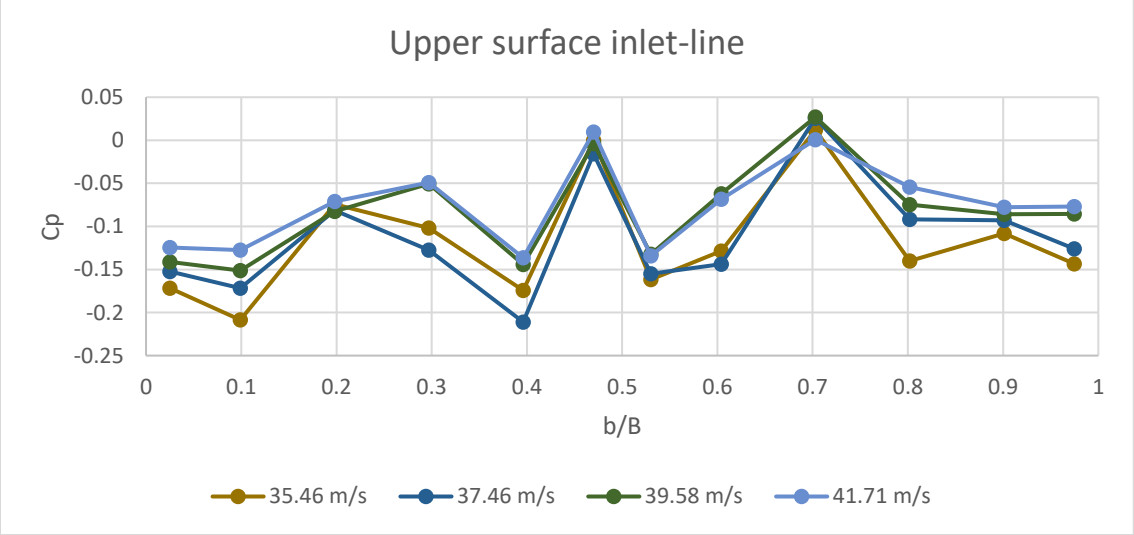

Figure A.6 Cp variation along the upper surface inlet-line (wind speed range 2, 180° AOI)

Cp along panels' lower surface inlet-line

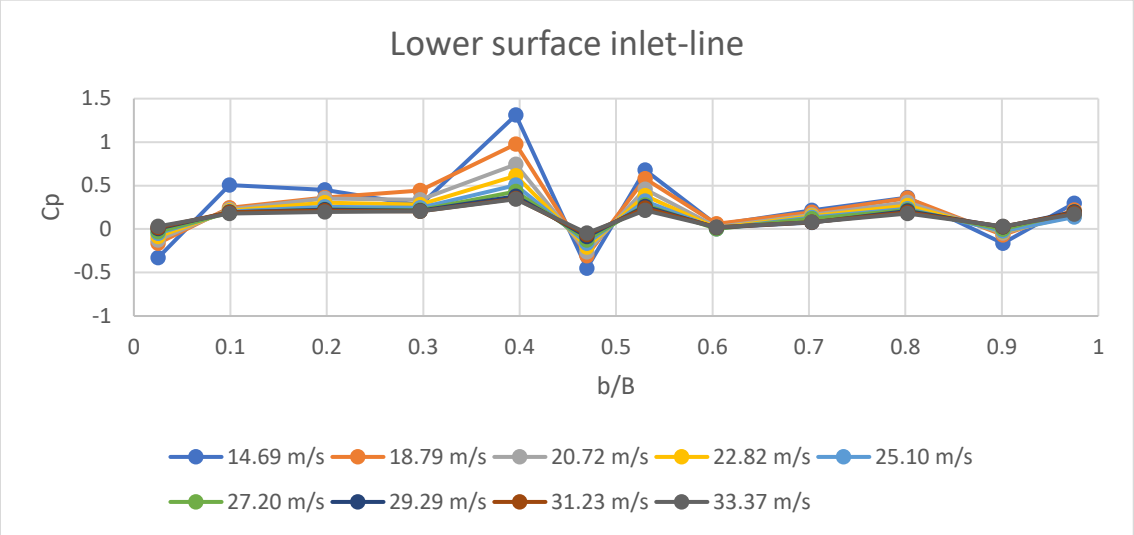

Figure A.7 Cp variation along the lower surface inlet-line (wind speed range 1, 180° AOI)

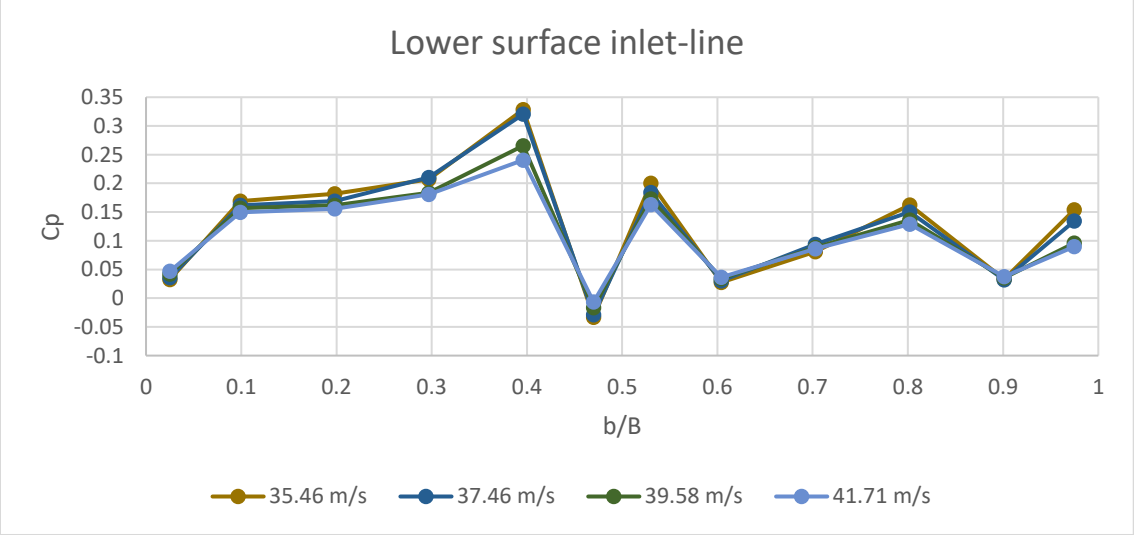

Figure A.8 Cp variation along the lower surface inlet-line (wind speed range 2, 180° AOI)

Cp along panels' upper surface edge-line

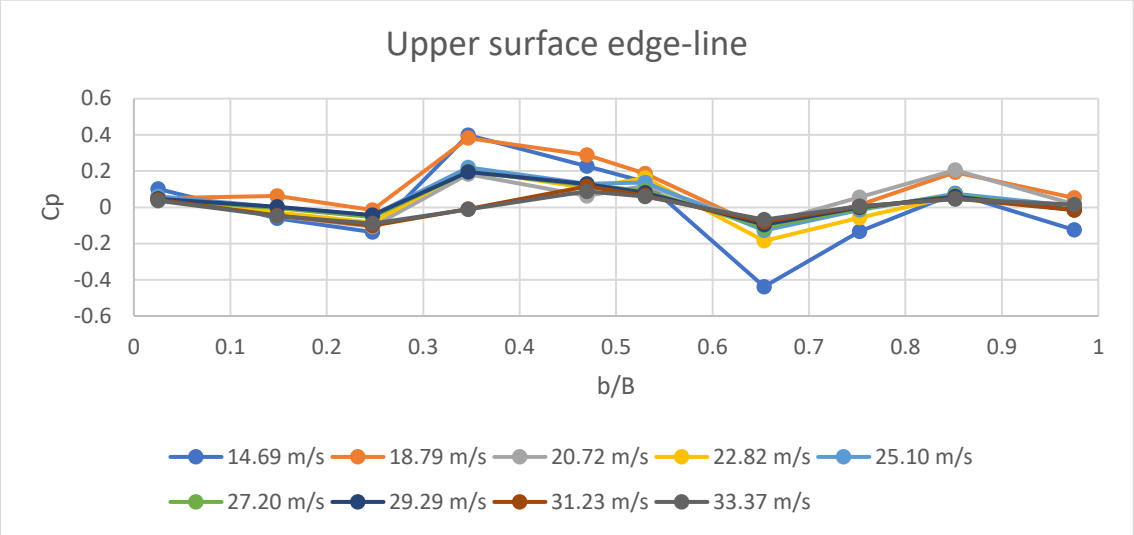

Figure A.9 Cp variation along the upper surface edge-line (wind speed range 1, 180° AOI)

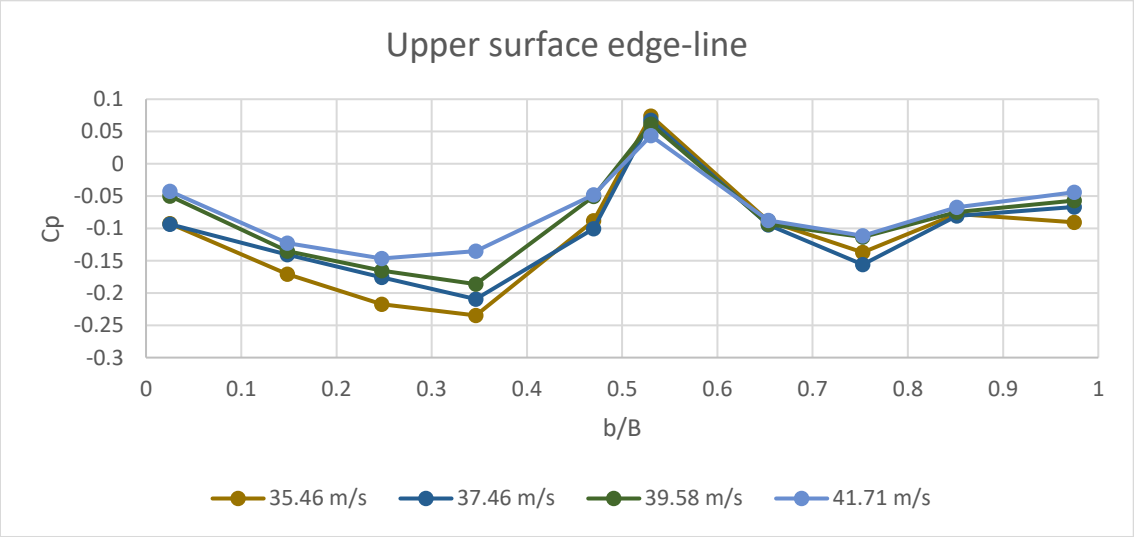

Figure A.10 Cp variation along the upper surface edge-line (wind speed range 2, 180° AOI)

Cp along panels' lower surface edge-line

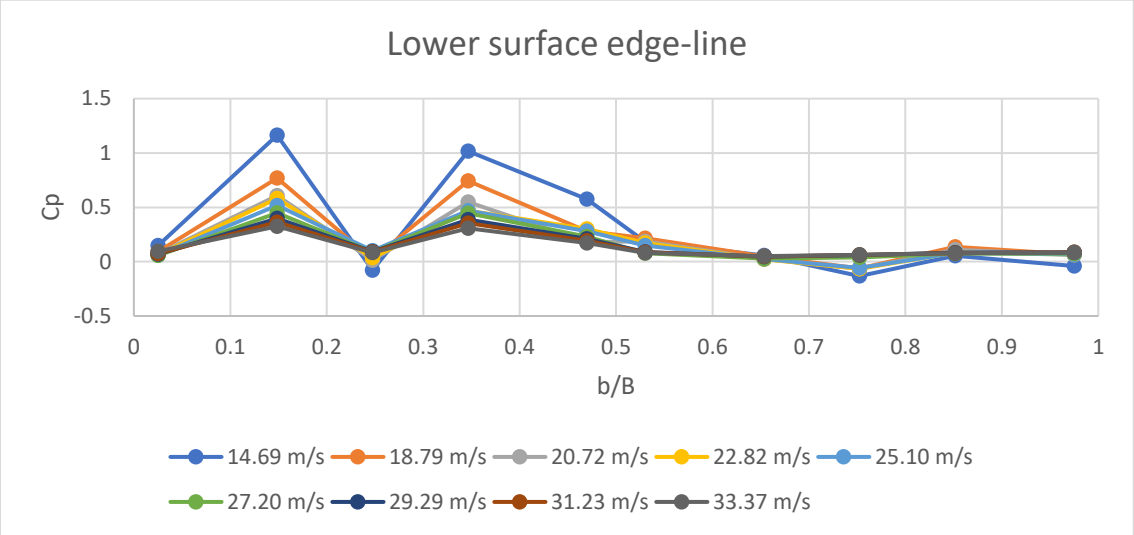

Figure A.11 Cp variation along the lower surface edge-line (wind speed range 1, 180° AOI)

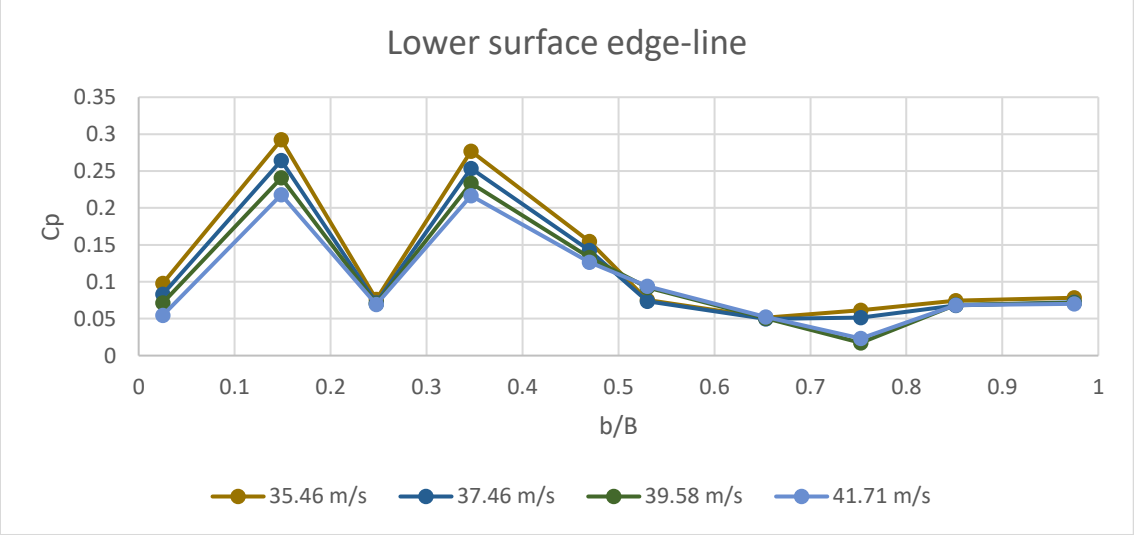

Figure A.12 Cp variation along the lower surface edge-line (wind speed range 2, 180° AOI)

Appendix B

AutoCAD drawings

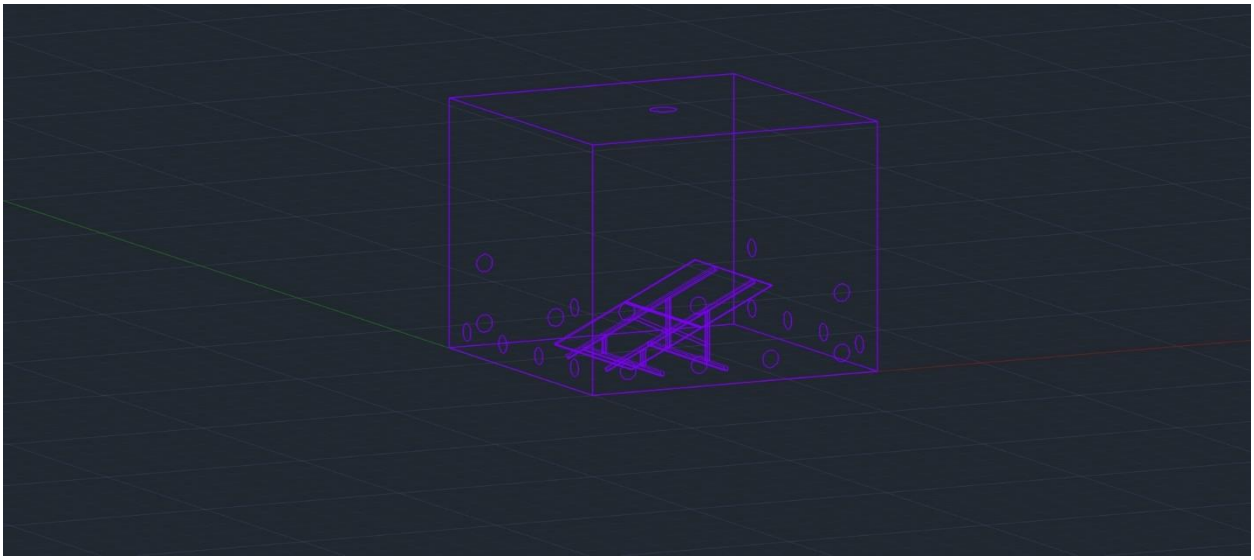

Figure B.1 Drawing representing the WDS facility with panels

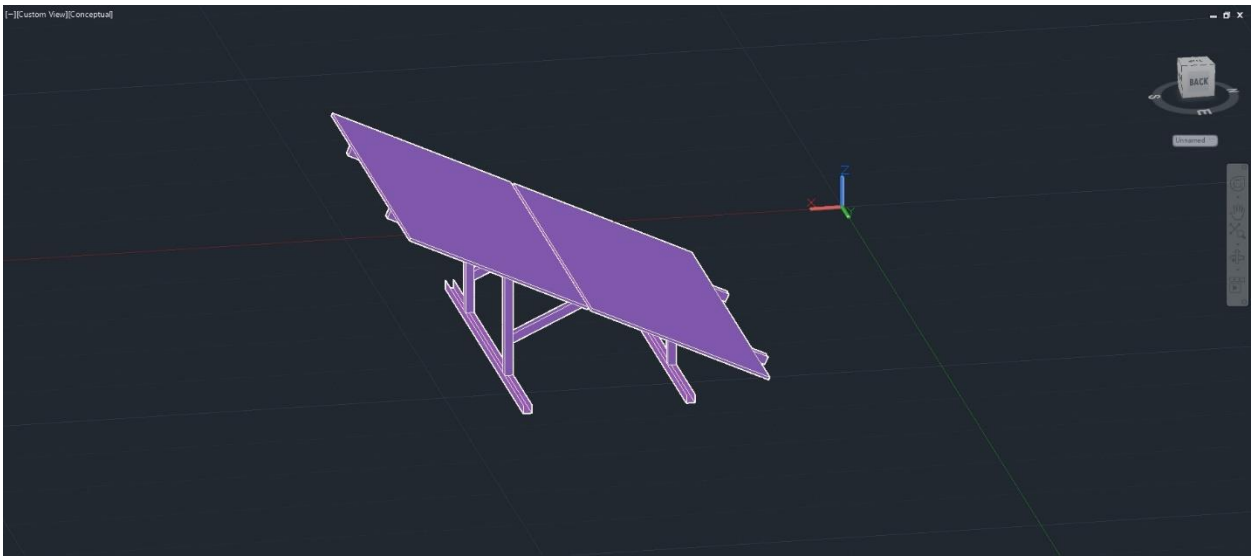

Figure B.2 Drawing representing the panels with frame

Different meshes figures

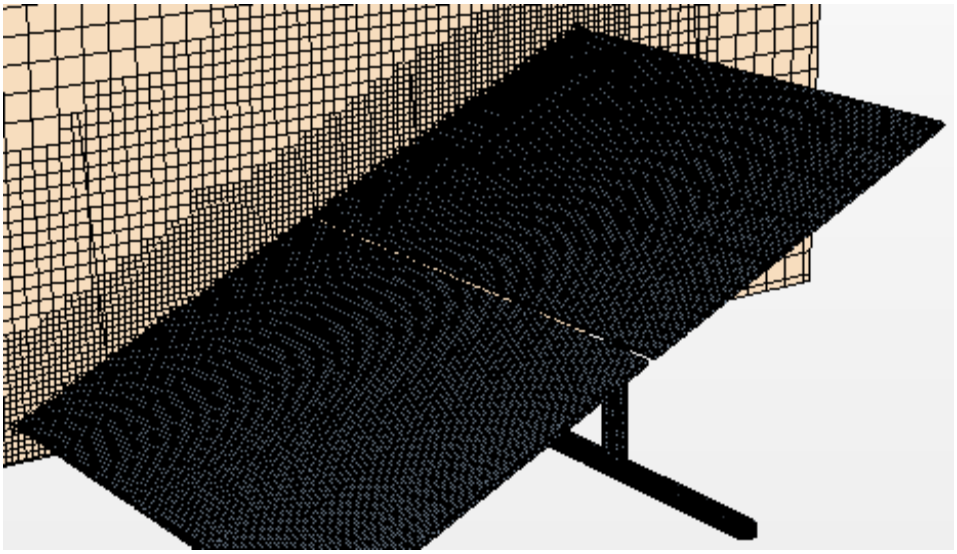

Figure B.3 Mesh A refinement around panels

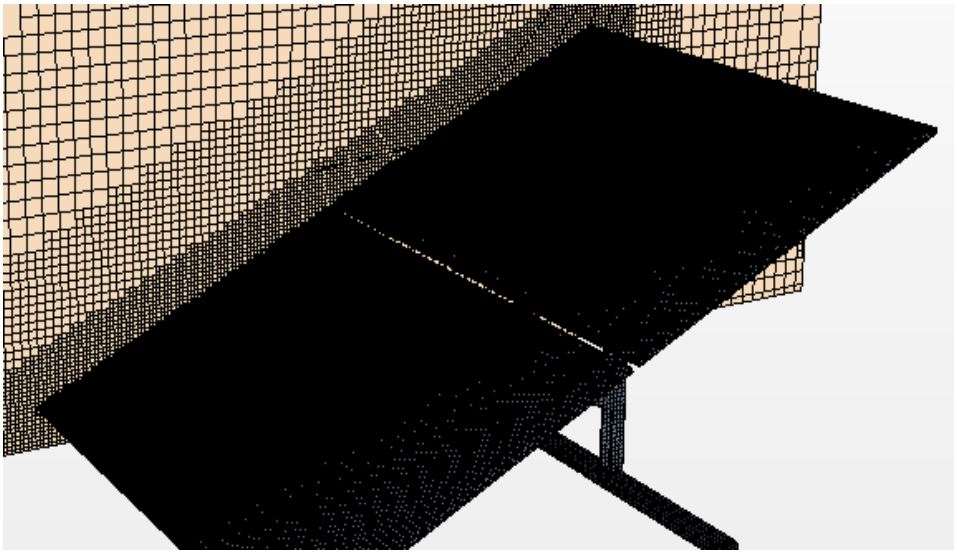

Figure B.4 Mesh B refinement around panels

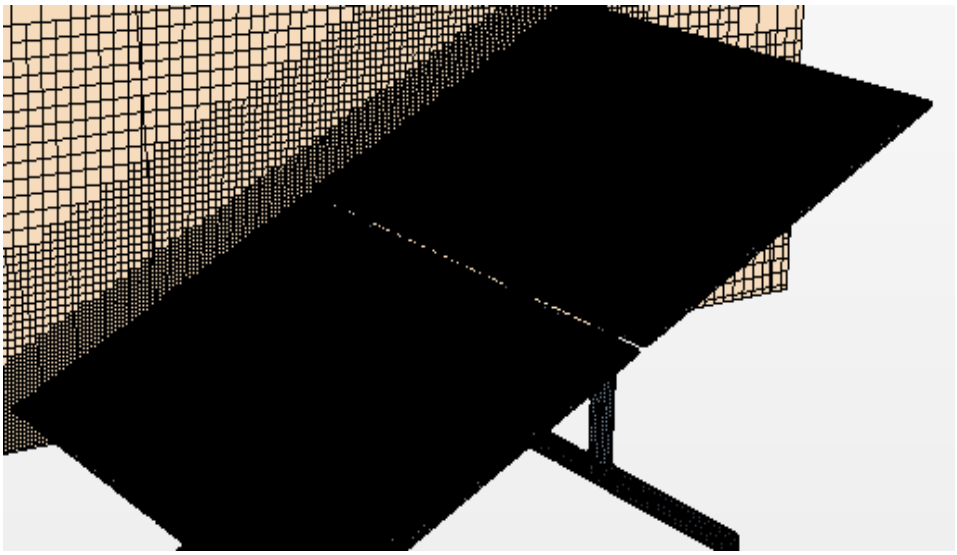

Figure B.5 Mesh C refinement around panels

Numerical Cp contours along the panels' lower surfaces

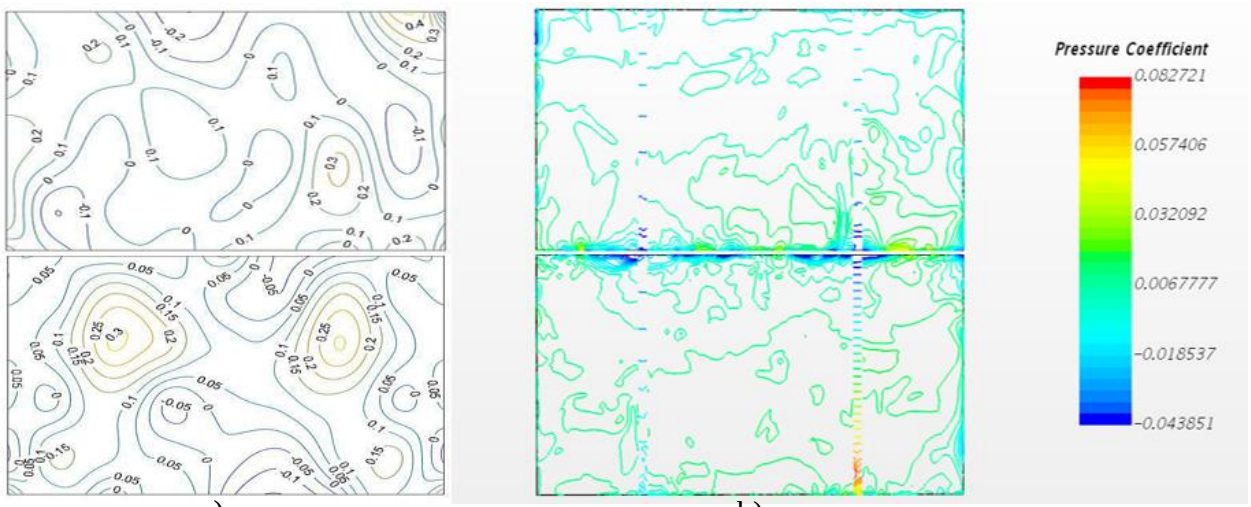

a) b)

Figure B.6 Pressure coefficient (0° AOI) contours on the solar panels' lower surfaces: a) experimental results b) numerical (LES) results

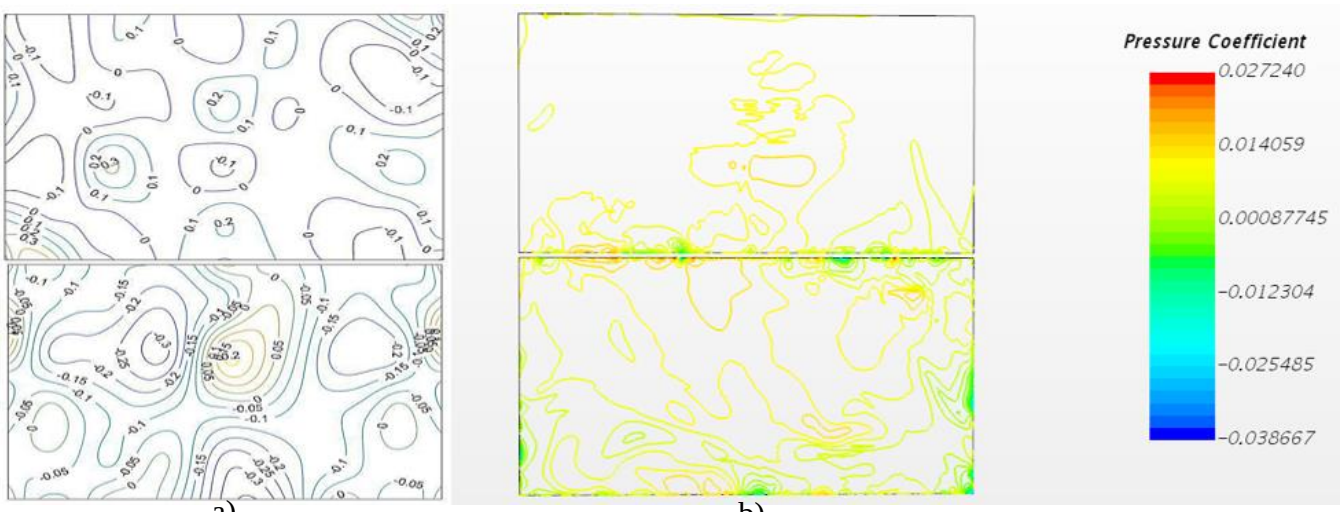

a) b)

Figure B.7 Pressure coefficient (180° AOI) contours on the solar panels' upper surfaces: a) experimental results b) numerical (LES) results